

MASTER

Hydrodynamics of slot jet injection into a cross-flow

van Mierlo, P.A.

Award date:
2006

[Link to publication](#)

Disclaimer

This document contains a student thesis (bachelor's or master's), as authored by a student at Eindhoven University of Technology. Student theses are made available in the TU/e repository upon obtaining the required degree. The grade received is not published on the document as presented in the repository. The required complexity or quality of research of student theses may vary by program, and the required minimum study period may vary in duration.

General rights

Copyright and moral rights for the publications made accessible in the public portal are retained by the authors and/or other copyright owners and it is a condition of accessing publications that users recognise and abide by the legal requirements associated with these rights.

- Users may download and print one copy of any publication from the public portal for the purpose of private study or research.
- You may not further distribute the material or use it for any profit-making activity or commercial gain

Take down policy

If you believe that this document breaches copyright please contact us providing details, and we will remove access to the work immediately and investigate your claim.

Hydrodynamics of slot jet injection into a cross-flow

P.A. van Mierlo
Master's thesis
WET 2006.19

14th August 2006

Committee:

prof.dr.ir. A.A. van Steenhoven (supervisor)
dr.ir. H.C. de Lange (coach)
dr. J.G.M. Kuerten
dr.ir. C.C.M. Luijten
M.B. Jovanović (advisor)

Technische Universiteit Eindhoven
Department of Mechanical Engineering
Thermo Fluids Engineering Division

Hydrodynamics of slot jet injection into a cross-flow

P.A. van Mierlo
14th August 2006

Preface

This thesis is submitted for the degree of Master of Science in Mechanical Engineering at Technische Universiteit Eindhoven. The research described herein was conducted under the supervision of prof. A.A. van Steenhoven and dr. H.C. de Lange in the Department of Thermo Fluids Engineering, Eindhoven, between September 2005 and August 2006.

I would like to acknowledge the influence of my mentors who first introduced me to the unexpected charms of fluid dynamics. I am pleased to express my thanks to my supervisor professor A.A. van Steenhoven. Also thanks to my promotor, Rick de Lange, for all of his assistance and guidance over the past year. I wish to express my sincere gratitude to Milenko Jovanović, my co-promotor, for his invaluable encouragement and guidance. Milenko's enthusiasm, support and aim at perfection in writing and conducting experiments are greatly appreciated.

I really appreciate the freedom that was given me in and around the laboratory. Let me also thank Henri and Geert Jan for helping me with fabricating the set-up and Jan for his assistance when I was experiencing computer problems.

Thanks to my fellow students Jeroen, Ruud, Esther and Marcel for the three pleasant years I have spend with them at the University. I would also like to thank my family for their support and encouragement during my study-time. Finally, I deeply appreciate the patience and understanding of my girlfriend, Annemiek, during the hours spent writing this thesis.

Abstract

Numerical simulations and particle image velocimetry experiments were carried out to investigate the effect of geometry variations on a slot-jet injection into a cross-flow. This type of flow is produced by film cooling and it can be found in gas turbines. The coolant ejection generates a complicated and sensitive flow field, which influences the heat and mass transfer (see Jovanović [12]).

In this thesis, the two-dimensional isothermal time-dependent incompressible Navier-Stokes equations were solved by means of the finite element software package Comsol. Firstly, computations were conducted with an injection through the perpendicular slot at the very-low velocity ratio of 0.25. The influence of three differently shaped imperfections, which were placed inside the slot, on the flow field was analyzed. An imperfection influences the flow inside the slot and has minor influence on the external flow field. The external flow field is dominated by vortical structures. The numerical simulations have shown that differences induced by different imperfections can be detected.

To validate these results, experiments were conducted in the water channel. Due to limitations inside the water channel, a jet was parallel supplied and through two-dimensional slot ejected perpendicularly into the cross-flow. Three slot geometries were analyzed: perfect, imperfect and inclined. The experiments were conducted at the velocity ratio of 0.75 and the cross-flow boundary layer was almost laminar. Unsteady flow fields were measured by means of particle image velocimetry. A shear layer, detected at the windward side of the jet, is quasi-periodically shed by positive and negative vortical structures. A second shear layer at the lee side is shed only by negative vortical structures. Differences have also been detected in the average flow fields.

To complete the study, new two-dimensional computations were conducted with similar geometries and corresponding flow conditions to the water channel experiments. A relatively good agreement to the experimental time-averaged data has been obtained. The instantaneous flow structures differ significantly.

Samenvatting

Numerieke simulaties en particle image velocimetry experimenten zijn uitgevoerd om het effect van geometrie variaties jet injectie door een spleet in een hoofdstroming te onderzoeken. Dit type stroming wordt geproduceerd in film-koeling applicaties welke in gas turbines toegepast worden. De injectie van een koelstroming genereert een complex en gevoelige stroming die invloed heeft op warmte- en massaoverdracht (zie Jovanović [12]).

In deze scriptie zijn de tweedimensionale tijdsafhankelijke onsamendrukbare Navier-Stokes vergelijkingen, zonder temperatuurvariaties, opgelost door het eindige elementen software pakket Comsol. Ten eerste, zijn berekeningen uitgevoerd met jet injectie door een loodrechte spleet bij de lage snelheidsverhouding van 0.25. De invloed van drie verschillende spleetimperfections op de stroming is geanalyseerd. Een imperfectie beïnvloedt de stroming in de spleet en heeft weinig effect op de omliggende stroming. De numerieke simulaties hebben aangetoond dat verschillen geproduceerd door de imperfecties aanwezig zijn.

Om deze resultaten te valideren zijn experimenten uitgevoerd in een waterkanaal. Begrenzungen in het waterkanaal hebben ertoe geleid dat een jet parallel werd aangevoerd en vervolgens door een tweedimensionale spleet geïnjecteerd in de hoofdstroming. Drie spleet vormen zijn geanalyseerd: perfect, imperfect en hellend. De experimenten waren uitgevoerd bij een snelheidsverhouding van 0.75 en de grenslaag van de hoofdstroming was bijna laminair. Niet-stationaire stromingen waren gemeten door middel van particle image velocimetry. Een schuiflaag, gedetecteerd aan de windzijde van de jet, wordt quasi-periodiek gevoed door positieve en negatieve wervelende structuren. Een tweede schuiflaag aan de lijzijde van de jet wordt gevoed door alleen negatieve wervelende structuren. Tevens zijn verschillen ook gedetecteerd in de tijdsgemiddelde stromingen.

Om de studie compleet te maken zijn nieuwe tweedimensionale berekeningen uitgevoerd met overeenkomstige geometrie en stromingscondities als in de waterkanaal experimenten. Een vrij goede overeenkomst met de tijdsgemiddelde stromingen is gevonden. De instantane stromingen tonen een significant verschil.

Contents

Preface	i
Abstract	iii
Samenvatting (in Dutch)	v
Nomenclature	ix
1 Introduction	1
1.1 Film cooling	1
1.2 Literature survey	2
1.3 Objectives and research approach	4
2 Numerical experiments Part I	5
2.1 Modeling the problem	5
2.2 Preliminary flow description	8
2.3 Mean flow	9
2.4 Instantaneous flow	11
2.5 Discussion	13
3 Water channel experiments	15
3.1 Measurement technique and postprocessing method	15
3.2 Experimental set-up	16
3.3 Preliminary flow description	18
3.4 Two-dimensionality	19
3.5 Mean flow	22
3.6 Instantaneous flow	26
3.7 Discussion	35
4 Numerical experiments Part II	39
4.1 Adapted numerical model	39
4.2 Preliminary simulation results	40
4.3 Mean flow	41
4.4 Instantaneous flow	44

5	Comparison	46
5.1	Numerical predictions with slot jet experiments	46
5.2	Slot jet injection with round jet injection	48
5.3	Discussion	50
6	Conclusions and recommendations	52
	Bibliography	54
A	Identification of vortical structures	56
B	Statistical analysis of vortical structures	62

Nomenclature

Convention

$\bar{}$	time-averaged quantity
\prime	time-fluctuating quantity
$\langle \rangle$	spatial-averaged quantity
$\hat{}$	spatial-fluctuating quantity

Vectors and tensors

\underline{v}	velocity $\underline{v} = (u, v, w)$
\underline{v}_1	irrotational velocity
\underline{v}_2	rotational but divergence free velocity
$\underline{\omega}$	vorticity distribution $\underline{\omega} = (\omega_x, \omega_y, \omega_z)$
\underline{g}	gravitation $\underline{g} = (0, -g, 0)$
\underline{t}	unit tangent
\underline{n}	unit normal
\underline{z}	unit normal to the xy -plane
$\underline{r}, \underline{r}^*$	position
\underline{s}	$\underline{r} - \underline{r}^*$
∇	symbolic $(\frac{\partial}{\partial x}, \frac{\partial}{\partial y}, \frac{\partial}{\partial z})$
\mathbf{I}	identity matrix
τ	viscous stress tensor
σ	total stress tensor

Subscripts

∞	main stream
jet	jet
max	maximum
i	integer
j	integer
vor	vortical structure
M	location in a domain
P	location in a domain

Roman symbols

x, y, z	$[m]$	coordinates
u, v, w	$[ms^{-1}]$	velocity components in x, y, z -direction
p	$[kgm^{-1}s^{-2}]$	pressure
t	$[s]$	time
A	$[m^2]$	cross-section
D	$[m]$	width of the slot
L	$[m]$	characteristic length
M	$[-]$	location in a domain
N	$[-]$	amount
P	$[-]$	location in a domain
U	$[ms^{-1}]$	modulus of velocity $ \underline{v} $
V	$[ms^{-1}]$	characteristic velocity
Re_x	$[-]$	Reynolds number related to x
Re_D	$[-]$	Reynolds number related to D
Tu_u, Tu_v, Tu_w	$[%]$	turbulence intensity in x, y, z -direction
U_∞	$[ms^{-1}]$	main stream velocity
V_{jet}	$[ms^{-1}]$	jet velocity
VR	$[-]$	velocity ratio

Greek symbols

α	$[^\circ]$	angle of velocity with horizontal
δ_1	$[m]$	boundary layer displacement thickness
δ_{99}	$[m]$	boundary layer thickness
η	$[kgm^{-1}s^{-1}]$	dynamic viscosity
θ	$[rad]$	angle between two velocity vectors
λ	$[-]$	eigenvalue of a matrix $\lambda = \lambda_{re} + \lambda_{im}$, wavelength
λ_{im}	$[-]$	swirling strength
ν	$[m^2s^{-1}]$	kinematic viscosity
ξ	$[%]$	percentage of time that a flow is dominated by rotation
ρ	$[kgm^{-3}]$	density
ς	$[%]$	percentage of vortical structures detected
Γ	$[m^2s^{-1}]$	circulation
Γ_1	$[rad]$	vortical structure identification function
$\Delta x, \Delta y$	$[m]$	spatial distance between grid points
$\Delta X_0, \Delta Y_0$	$[m]$	size of an interrogation window
ΔZ_0	$[m]$	thickness of light sheet
Ω	$[s^{-1}]$	average vorticity

Chapter 1

Introduction

1.1 Film cooling

Gas turbines are used to convert caloric energy to work power. They have a great contribution in aircraft propelling and electrical power generation. Within a gas turbine a mixture of compressed air and fuel is combusted. This combustion produces high temperature gases. Hot gas flows through static vanes towards rotor blades which are mounted on a shaft. Due to flow characteristics around blades a force is induced and a shaft rotation is obtained. A part of the rotating energy is used to compress the combustion air. In electrical power stations the remnant of the energy is used to drive a generator. In propulsion applications, the remnant is used as thrust. An increase in the turbine inlet temperature rises a gas turbine cycle efficiency. A drawback is that the temperature exceeds the melt temperature of turbine elements. In order to prevent thermal damages of critical turbine components, film cooling is applied. Film cooling concerns the bleeding of internal component cooling air through a components shell to form a protective layer of cooling between the hot gases and the component external surfaces [6]. A schematic cross-section of a turbine blade with flow directions of the coolant gasses are schematically illustrated in figure 1.1. The figure also shows a simplified drawing of one film cooling hole and its flow field.

The effect of geometry of a film cooling hole on a film cooling effectiveness is widely investigated. The best cooling performance would be obtained by film cooling slots with uniformly distributed cooling supply [6]. Though, aerodynamics, thermal and mechanical stresses and fabrication methods prevent its appropriateness. Therefore, film cooling is mostly performed through discrete holes and rows of equally spaced holes.

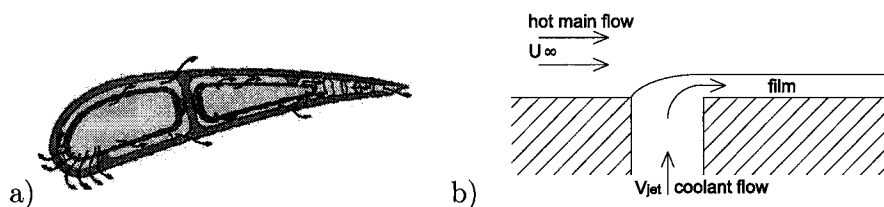


Figure 1.1: Schematic illustration of a) coolant gas flow in the cross-section of a turbine blade and b) a simplified flow field of one film cooling hole.

1.2 Literature survey

Film cooling can be ranked in the fundamental flow configuration where a jet is injected into a cross-flow. This configuration is common in a wide range of processes like mixing of different streams, pollutant dispersion from chimneys and cooling or heating purposes. Because of their importance in these applications many studies have been performed on flow features in such a configuration. From these studies it can be concluded that a highly complex flow field is generated due to jet cross-flow interaction. The flow is influenced by geometric parameters such as shape of the film cooling hole and the streamwise jet injection angle. Also dynamic parameters determine flow characteristics such as the turbulence level of the cross-flow and the jet-flow and mass flux ratio $M = \frac{\int \rho_{jet} U_{jet} dA_{jet}}{\rho_{\infty} U_{\infty} A_{jet}}$, or in the situation of an equal fluid density of both streams, velocity ratio

$$VR = \frac{V_{jet}}{U_{\infty}}. \quad (1.1)$$

The present study arises from the work of Jovanović et al. [13]. They investigated experimentally the influence of discrete inaccuracies in a round hole on jet cross-flow interaction. These inaccuracies represent obstacles in the hole that are created during the production process of a film cooling hole. Turbine blades are made from an alloy with high strength against creep at high temperatures. Turbine vanes are made from a heat-resisting alloy in order to avoid thermal impact and oxidation. Film cooling holes can be produced by laser drilling. This method works well for the applied alloys, but has the disadvantage that the production accuracy is imprecise. An inaccuracy that can occur due to laser drilling is solidification of vaporized material inside the film cooling hole. Observations showed that they can decrease the hole cross sectional area with 25%. This creates an obstruction for the coolant fluid and thereby influences the flow. Jovanović et al. injected a jet into a cross-flow with various velocity ratios. In the case of $VR > 0.5$, a positive windward vortical structure was generated by the inaccuracy which was absent in the smooth hole. This vortical structure enhances mixing of the jet and cross-flow with the result that the film cooling effectiveness decreases. The question raise whether this additional windward vortical structure was the result of three-dimensional effects or will it also develop in a ‘two’-dimensional situation? A reliable numerical model can in that situation operate as a powerful tool to predict film cooling effectiveness by different hole configurations. The present work is a first step towards such a numerical model and therefore focusses upon a two-dimensional approach. A large amount of studies on jet cross-flow formations have been reported in literature. The investigations closely related to two-dimensional slot jets examined in this study are mentioned here.

Fitt et al. [9] illustrated the general flow characteristics induced by the slot jet injection normal to the cross-flow as shown in figure 1.2. The cross-flow boundary layer may produce an interaction with the jet near the leading edge of the slot. At the boundary between the jet and cross-flow a shear layer is formed. The injected flow may separate at the trailing edge of the slot and subsequently reattach. Instabilities inside the shear layer will cause the flow to become turbulent further downstream.

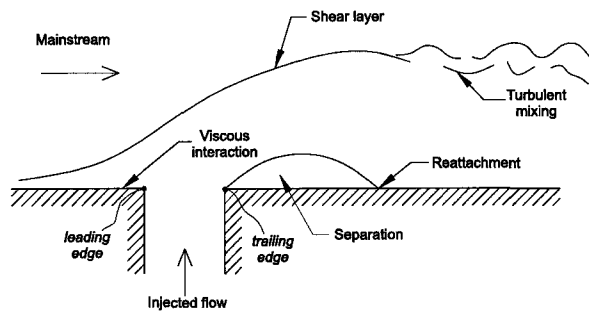


Figure 1.2: A general description of the two-dimensional flow field (from Fitt et al. [9]).

Fitt et al. [9] proposed an analytic theory to determine the mass flow within the film. It was assumed that the flow is two-dimensional, irrotational and inviscid. This theory does not include the effect of downstream separation, upstream boundary layer thickness and turbulent mixing downstream. They reported jet separation from the windward wall of the slot. The cross-flow acts as a lid over the slot which forces jet fluid to emerge near the lee side of the slot. This feature was denoted as the ‘lid’-effect. This was experimentally validated by pressure measurements along the surface of a configuration where a slot jet was injected into a cross-flow over a flat plate.

Miron et al. [17] measured the flow field induced by slot jet injection into a main stream by means of laser Doppler velocimetry. Time-averaged streamlines showed the presence of a circulation zone downstream of the slot at injection angles larger than 30° . For jets injected under an angle of 40° , a stronger jet flow seems to generate a smaller circulation zone. Among the tested injection angles, a 30° inclined jet provides the highest film cooling effectiveness in addition to a velocity ratio of one.

Aly [2] presented time-averaged velocity profiles in the downstream field of a slot jet injection, under angles varied from 15° to 90° , into a developed turbulent boundary layer along a flat surface with film cooling applications. Velocity was measured in a wind tunnel. Injection angles larger than 45° create a separation bubble downstream of the injection slot. A jet injected, using angles smaller than 30° , diffuses fast.

Numerical experiments of a two-dimensional perpendicular jet issuing into a cross-flow at velocity ratios ranging from 0.1 to 0.8 were conducted by Kassimatis et al. [15]. The time-averaged Navier-Stokes equations were solved with an additional model for turbulence. They concluded that the ‘lid’ effect was the strongest for a low velocity ratio, furthermore the length of a separation bubble downstream of the slot increases linearly with velocity ratio.

Sarkar and Bose [23] solved the two-dimensional time-dependent, mass-averaged Navier Stokes equations coupled with an additional turbulence model. For large injection angles, the coolant jet penetrates more into the cross-flow resulting in greater turbulence generation, followed by enhance mixing and a rapid turbulent diffusion which leads to a faster decay of film cooling effectiveness.

Miron et al. [17] solved in their numerical model the time-averaged Navier-Stokes equations and tested three turbulence models for a slot jet injection into a cross-flow with various injection angles. The condition of the upstream cross-flow boundary layer has only little effect on film-cooling effectiveness. A circulation zone was computed upstream of the injected jet. A downstream circulation bubble was predicted longer than obtained in experiments conducted in a wind tunnel. They suggested that this was the result of three-dimensional influence in the measurements.

It can be concluded from these studies that velocity ratio and jet injection angle are of significant importance in slot jet configurations. The formation of a recirculation bubble downstream of the injection slot should be avoided to gain an improved film cooling effectiveness. This can be achieved by injecting a slot jet into the cross-flow under an angle with the horizontal between 30° and 40° with a velocity ratio around one. Obtained experimental data are presented as time average results. The numerical codes mentioned above were all modified by a turbulence models. Data obtained numerically give information about film cooling effectiveness, time-averaged pressure distribution along the surface in streamwise direction, time-averaged velocities, turbulent kinetic energy and turbulence intensities. None of the studies regarding slot jet injection into a cross-flow give a detailed description of instantaneous flow fields.

1.3 Objectives and research approach

The geometry of film cooling slots affects the flow field and therefore the film cooling effectiveness. A numerical model of the slot-jet injection into a cross-flow may be used as an effective preliminary design tool to screen alternative slot configurations. The goal of this study is to investigate the influence of the jet geometry on the flow field. To this end numerical and experimental investigations are performed with different geometries. Variations of the flow field, induced by slot jet injection into a cross-flow, are studied. Numerical and experimental data are compared.

The commercial software package ‘Comsol’ offers a user-friendly interface, which enables relatively easy geometry variations. This package gives the opportunity to solve the Navier-Stokes equations coupled with the energy equation. The outcome are pressure, velocity components and temperature. A first step towards reliable numerical predictions is to determine and quantify the flow field without solving the energy equation. Flows, induced by a perpendicular slot-jet injection into a cross-flow through different slot geometries, are predicted numerically. The slot jet injection into a cross-flow is experimentally studied in a water channel. The flow field, generated by three different slot geometries, is measured by means of particle image velocimetry. The experimental flow conditions are different than in the preliminary computations. Therefore additional two-dimensional computations are implied to calculate the flow field induced by similar geometric and flow conditions as in the water channel experiments. Finally a comparison between the two-dimensional numerical simulations, the slot jet experiments and data from Jovanović et al. [12] is performed.

Chapter 2

Numerical experiments Part I

2.1 Modeling the problem

Short introduction to Comsol

Comsol is an environment for modeling and solving a large range of scientific and engineering problems based on partial differential equations. A user defines a geometry and the physical properties regarding the problem, for example material properties, fluxes and loads. Comsol uses these quantities and compiles internally a set of differential equations which represents the entire model. There are two ways to use Comsol, one as a stand alone product through a graphical interface (GUI) and second by script programming in the Matlab language. To solve the set of partial differential equations, Comsol uses the finite element method.

The software contains diverse options to present the data. One can create velocity plots, pressure and/or vorticity field in the background. The cross-section option can be used to draw a graph of the mentioned quantities on an arbitrary trajectory. To analyse the data set, also a movie of the stored time steps can be made. To analyse the data with an other software, the data must be exported. Exportation can be realized as an ASCII-file or as 'Fem-structure'. The latter can extract the data from Comsol into Matlab in such a way that postprocessing in Matlab can be done.

Governing equations

The two-dimensional isothermal time-dependent problem modeled here, is described by the equation expressing conservation of mass:

$$\nabla \cdot \underline{v} = 0 \quad (2.1)$$

and the equation describing conservation of momentum:

$$\rho \frac{\partial \underline{v}}{\partial t} + \rho (\underline{v} \cdot \nabla) \underline{v} = -\nabla p + \eta \nabla^2 \underline{v} + \rho \underline{g}, \quad (2.2)$$

in which ρ is the fluid density, t is the time, \underline{v} is the velocity vector $\underline{v} = (u, v)$ with u and v the velocities in x respectively y -direction, p the pressure, η the dynamic viscosity, \underline{g} the gravitational acceleration and ∇ is the 'nabla'-operator (a symbolic vector: $(\frac{\partial}{\partial x}, \frac{\partial}{\partial y}, \frac{\partial}{\partial z})$). Equation 2.1 and 2.2 are generally known as the incompressible Navier-Stokes equations. Comsol solves the pressure p and the velocity components u and v .

Boundary conditions

A Comsol stand alone application was chosen to build the model. The geometry was build with lines and curves which form the boundaries of the model. The boundaries are schematically shown in figure 4.1 and form a closed contour which is denoted as subdomain in Comsol. Each line or curve represents a solid boundary or a part of the fluid. This means that every line must get a boundary condition to describe the model. A subdomain describes the fluid density, viscosity and volume forces like in the present study gravitational acceleration ($F_y = \rho g$). The problem that is modeled here represents a cross-flow of water over a flat plate from left to right. A water jet issues perpendicular into the cross-flow through an injection slot.

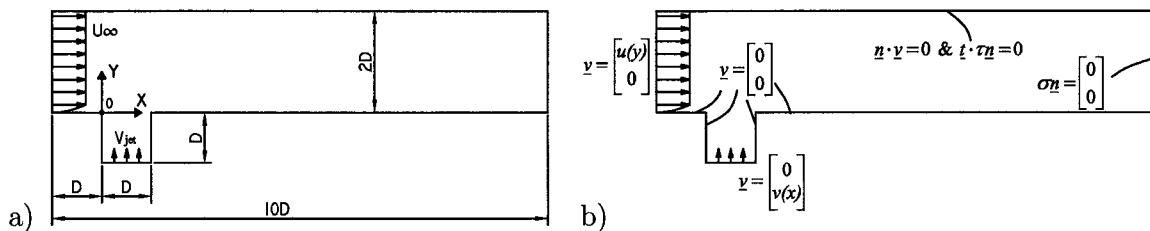


Figure 2.1: Schematic view of a) the computational domain and b) the boundary conditions.

The applied boundary conditions are illustrated in figure 4.1. The inlet boundaries for the cross-flow and the slot jet both have an inflow condition. These conditions were prescribed with velocity profiles. The inlet velocity, which becomes the jet, differs in the computations and was prescribed by either a parabolic or trapezoidal distribution, see section 2.1. The velocity profile which describes the inlet of the cross-flow is given by

$$u(y) = \begin{cases} U_\infty \sin(\zeta y) & , \quad 0 \leq y \leq \frac{\pi}{2\zeta} \\ U_\infty & , \quad y \geq \frac{\pi}{2\zeta} \end{cases} \quad \text{where } \zeta = \sqrt{\frac{U_\infty}{\nu x} \left(\frac{4 - \pi}{8} \right)}. \quad (2.3)$$

This velocity profile describes an approximation of a laminar boundary layer over a flat plate at position x . In equation 2.3 U_∞ is the cross-flow velocity above the laminar boundary layer. Prescribing this velocity profile saves memory and calculation time, due to the fact that the development of the boundary layer does not have to be computed. A slip/symmetry condition was applied on the top boundary of the model. This means that the normal component of the velocity is zero $\underline{n} \cdot \underline{v} = 0$ and the tangential component of the viscous force vanishes $\underline{t} \cdot \underline{\tau} \underline{n} = 0$. \underline{n} is the unit normal vector on the boundary, \underline{t} is the unit tangent vector on the boundary and $\underline{\tau}$ is the viscous stress tensor defined as $\underline{\tau} = \eta(\nabla \underline{v} + (\nabla \underline{v})^T)$. A neutral boundary condition was applied as an outflow condition on the right hand side of the domain, which means that the total force vanishes, defined as $\underline{\sigma} \underline{n} = 0$, where $\underline{\sigma}$ is the total stress tensor given by $\underline{\sigma} = -p \underline{I} + \eta(\nabla \underline{v} + (\nabla \underline{v})^T)$, where \underline{I} is the identity matrix. Vosse [27] showed that the outflow boundary condition influences the solution of the numerical calculations. Therefore it was chosen to extend the length of the domain with the expectation that the flow field near the slot will not be influenced by the outflow boundary condition. All the other boundaries have the no-slip condition $\underline{v} = 0$.

Mesh

An unstructured/adaptive mesh of triangular shaped Lagrange elements was employed with a second order element for the velocities and a linear element for the pressure. Cmsol generates the mesh automatically. A user has several possibilities to manipulate this generation, for example prescribing mesh dimensions and element grow rates on boundaries and subdomains. In the present model grid refinement was adapted near the trailing edge of the slot, along the solid walls and near the outlet boundary. The mesh created approximately 52.000 degrees of freedom.

Solution procedure

The problem that Cmsol has to solve is nonlinear of nature because of the second term in the momentum equation (eq: 2.2). A direct solver breaks down the nonlinear problem into the solution of a linear system of equations. The solver solves this system by Gaussian elimination. The solver chooses its time steps arbitrarily.

A pentium(R) 4 CPU 3.4GHz with 1.0Gb of RAM was used to solve the model. An initial value along the domain was chosen as $\underline{v}_{t=0} = 0$ and $p_{t=0} = 0$. First computations were conducted with a velocity ratio of 0.01. The velocity ratio was increase stepwise to the final number of 0.25. The solver computed solutions for a numerical time of 10s. The solution at $t = 10s$ was used as an initial value for further calculations. Main calculations were conducted for a numerical time of $t = 9s$. Data was stored every 0.1s and imported into Matlab for postprocessing along a rectangular grid along the whole domain with spatial distances of Δx , $\Delta y = 2mm$.

Configurations

This investigation focusses upon the prediction of a flow field induced by a slot jet injection into a cross-flow and the influence of slot geometry variations to this flow field. Four slot geometries were composed where the first one has smooth walls. Three others where provided with discrete imperfections on the leading and trailing wall of the slot. The shape of an imperfection differs from triangular, round and rectangular. They were in all three cases located at a depth of $0.3D$ inside the slot and forming a blockage of $0.4D$, where D is the width of the slot. An additional configuration was composed to analyse the influence to the flow field of a jet inlet velocity distribution in the smooth wall configuration. The five configurations are schematically represented in table 2.1 and referred to as 1 till 5. The velocity profile in configuration 2 was parabolic and defined as

$$v(x) = V_{jet} \left[-6 \left(\frac{x}{D} \right)^2 + 6 \left(\frac{x}{D} \right) \right]. \quad (2.4)$$





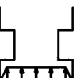
The velocity distribution in the other four configurations was trapezoidal defined as

$$\left. \begin{aligned} v(x) &= V_{jet} \left[10 \left(\frac{x}{D} \right) \right] & , & \quad 0 \leq \frac{x}{D} \leq 0.1 \\ &= V_{jet} & , & \quad 0.1 \leq \frac{x}{D} \leq 0.9 \\ &= V_{jet} \left[-10 \left(\frac{x}{D} \right) + 10 \right] & , & \quad 0.9 \leq \frac{x}{D} \leq 1 \end{aligned} \right\}. \quad (2.5)$$

An experimental study of the flow field generated by jet injection into a cross-flow has been reported by Moerkerken [18]. A film cooling geometry was imitated in a water channel

set-up located at Technische Universiteit Eindhoven. A slit was made in a flat plate which was fixed inside the water channel. A main stream was forced over the flat plate where it formed the cross-flow. A secondary flow entered a space under the flat plate and was forced to leave the space through the slit in the plate, where it became the jet. The width/length ratio of the slit was 2 and therefore assumed to induce a two-dimensional behavior along the symmetry plane of the channel. The flow was measured by means of particle image velocimetry (see section 3.1 for information about this measurement method). This study has been chosen as a benchmark to set the geometric properties of the present numerical domain. The applied fluid properties and flow characteristics are listed in table 2.1. The slit was located $1300mm$ downstream of the plates leading edge. The theoretical boundary layer thickness at the leading edge of the slot is $\delta_{0.99} = 14.1mm$.

Table 2.1: Fluid properties, flow characteristics and configurations.

Quantity	Symbol	Value	Unit		
density	ρ	$1 \cdot 10^3$	kg/m^3		
kinematic viscosity	ν	$1 \cdot 10^{-6}$	m/s^2		
cross-flow velocity	U_∞	150	mm/s		
velocity ratio	VR	0.25	—		
Reynolds number	Re_x	$2 \cdot 10^5$	—		
Reynolds number	Re_D	$3.7 \cdot 10^3$	—		
width of the slot	D	100	mm		
configuration	1	2	3	4	5
					

2.2 Preliminary flow description

An instantaneous flow field obtained in configuration 1 is represented by streamlines in figure 2.2. The cross-flow lifts up above the slot and streams over the bounded jet. The lid-effect above the slot is recognizable which means that the cross-flow forces jet fluid towards the lee wall of the slot. The jet fluid has to pass a decreased passage to enter the cross-flow. This results in acceleration of the jet. A small circulation zone is present near the leading edge of the slot between the cross-flow and the jet. The downstream field is dominated by negative vortical structures. They develop near the trailing edge of the slot and are advected downstream.

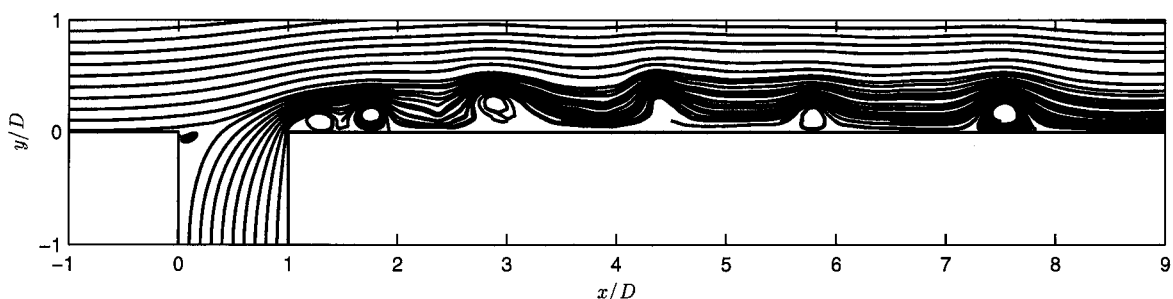


Figure 2.2: Instantaneous streamlines of configuration 1.

2.3 Mean flow

A normalized time-averaged velocity is given by

$$\bar{\underline{v}} = \frac{1}{NU_\infty} \sum_{j=1}^N \underline{v}(t_j), \quad (2.6)$$

where \underline{v} is the velocity vector $\underline{v} = (u, v, w)$ at a position in the domain, j is the time integer and N is the amount of time samples taken into account. The streamlines of $\bar{\underline{v}}$ for configuration 1 and 5 are depicted in figure 2.3. The streamlines indicate that the jet pushes the cross-flow above the slot, which results in a lift up of the cross-flow. The jet bends into the direction of the cross-flow after impingement. The penetration height of the jet into the cross-flow is approximately $0.4D$ for the five configurations. Downstream of the trailing edge a negative circulation is observed. The length of this circulation zone in configuration 1 is $0.86D$, for configuration 2 $0.74D$ and for the configurations with imperfections $0.66D$. One circulation zone is present inside the slot near the leading edge regarding the two configurations without imperfections. This is a negative circulation zone. A second positive circulation area is detected in the cases with imperfections (see figure 2.3). A leading edge circulation blocks the exit of the slot for $0.3D$ in configuration 1 and 2 (without imperfections) and with $0.5D$ in the cases with imperfections. A penetration angle α , which the fluid has with the horizontal at the exit of the slot, is influenced by the imperfections. The largest difference is present near the trailing edge. α is smaller when an imperfection is present and the smallest in the case of a squared imperfection. The jet inlet distribution does not influence the penetration angle.

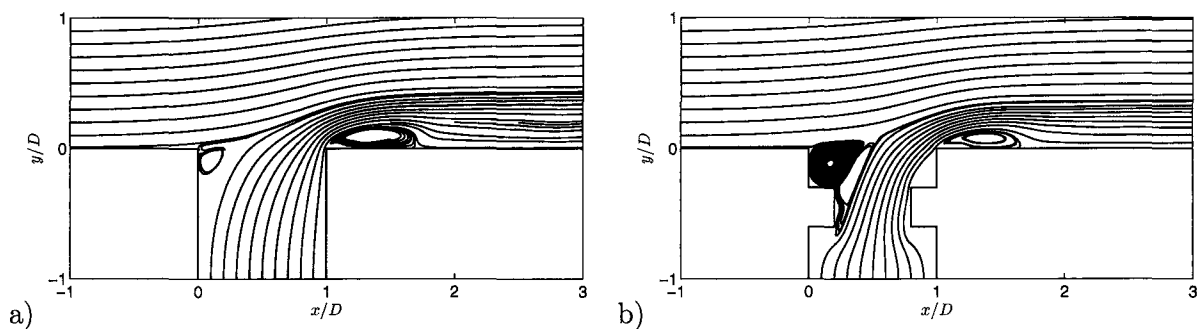


Figure 2.3: Streamlines of time-averaged velocity for configuration a) 1 and b) 5.

Profiles of the mean velocity \bar{v} are provided in figure 2.4 for configuration 1 and 5 at different y -positions to examine the development of the jet. The jet inlet distribution changes at increasing y -position. A maximum \bar{v} shifts towards the downstream wall of the slot. This maximum changes in a high local velocity near the exit of the slot ($y = 0$). The high value smears out when it leaves the slot. An imperfection reduces the width of the slot locally which results in an acceleration of the jet inside the slot. In both cases a concave velocity distribution is present at the exit of the slot.

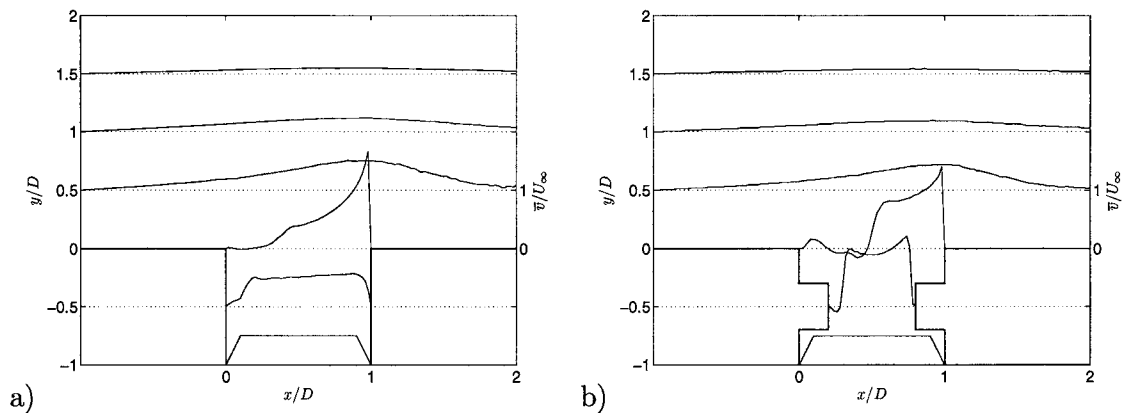


Figure 2.4: Development of \bar{v} inside and above the slot in configuration a) 1 and b) 5.

Figure 2.5 shows contour plots of \bar{u} concerning configuration 1. An area with $\bar{u} > 1.3U_\infty$ is present downstream of the trailing edge, above the bounded jet. This is due to acceleration of the cross-flow as a result of continuity where the flow has to overcome the obstacle created by the jet. Two shear layers can be distinguished. The first one seems to originate from the cross-flow boundary layer and forms a recognizable interface between the injected jet and the cross-flow. The second shear layer starts at the trailing edge of the slot and diverges further downstream. The velocity goes to zero at the wall. Small differences are present in quantitative values of \bar{u} regarding the other configurations, but the trends are similar.

A turbulence intensity in percents of U_∞ is calculated by

$$Tu_a = 100 \frac{a_{rms}}{U_\infty}, \quad a = u, v, w \quad (2.7)$$

where a_{rms} is defined as

$$a_{rms} = \sqrt{\frac{1}{N-1} \sum_{j=1}^N a'(t_j)^2} \quad (2.8)$$

with a' the fluctuating velocities in the three directions according to Reynolds decomposition

$$\underline{v} = \underline{\bar{v}} + \underline{v}'. \quad (2.9)$$

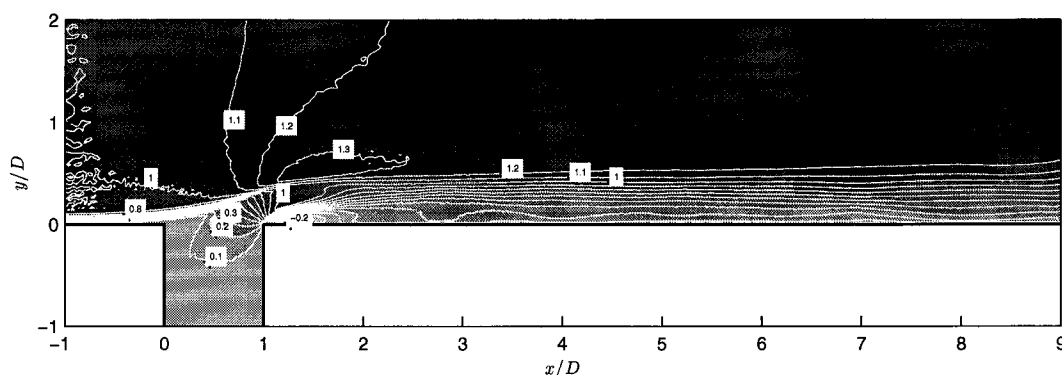


Figure 2.5: \bar{u} -contour plots of configuration 1.

Tu_u and Tu_v for configuration 1 are depicted in figure 2.6. Turbulence intensities are zero inside and above the slot, which indicates that the flow is stable in these regions. Thus, the leading edge circulation is a stagnant bubble and the shear layer originating from the cross-flow boundary layer is stable. The downstream field shows fluctuations to 50%. The largest turbulence intensity in x -direction is present near the wall, where fluctuations in y -direction are low. This is caused by suppression of v' by the solid wall. The high fluctuations are the result of the advected structures on the lee side of the jet. The turbulence intensity inside the detected circulation zone downstream of the jet is high, which means that it is no recirculation bubble. Comparing configurations shows a minor increase in Tu_u and Tu_v above the slot. The trends are similar in the downstream field. This indicates that the imperfections have a local contribution to the turbulence level of the flow.

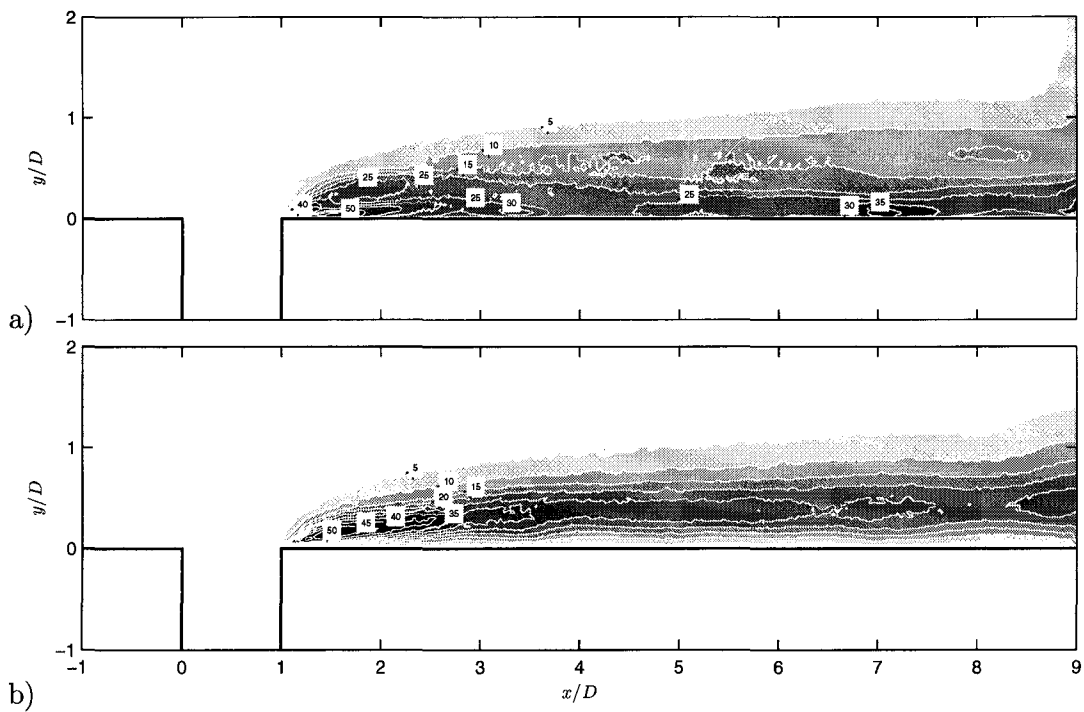


Figure 2.6: Contour plots of turbulence intensity a) Tu_u and b) Tu_v of configuration 1.

2.4 Instantaneous flow

The generation frequency of advected vortical structures is not constant in time. Also the size and advection velocity of these structures differs. It has been noticed that sometimes one structure catches up with another one, with the result that they might merge to one larger structure. Comparison of the instantaneous data between the configurations shows similar flow features. Vortical structures are advected downstream in all five configurations. The predicted flow fields have been used to analyse the time-dependent flow with special interest in the large scale vortical structures. A number of algorithms are suggested in literature to identify vortical structures within a discrete flow field. After an analysis of three detection algorithms it was chosen to proceed with the Γ_1 -method, proposed by Graftieaux et al. [7]. A detailed description of the Γ_1 -method and the other two test cases is provided in appendix A. The thresholds were $N = 169$ and $|\Gamma_1| > 0.8$ in this analysis.

Figure 2.7 shows seven vortical structures identified in the same velocity field as presented by streamlines in figure 2.2. All the structures have a negative rotation. Their centers are marked with a white dot inside every structure. This mark represents the center of that structure. A comparison between the streamlines and the detected vortical structures shows that the circulation zones downstream of the slot are vortical structures. It is interesting to see that the Γ_1 -method detected a structure at $x = 6.7D$. The streamlines did not indicate the presence of such a structure there. This means that a vortical structure can be hidden in an instantaneous velocity field. This issue is enlightened in chapter 3.6.

The detected centers of the vortical structures are drawn in a place-time diagram. This results in a diagram which indicates the advective path of a vortical structure. Figure 2.8 illustrates the diagram for configuration 1 and 5. Some vortical structures stay present in time once they are identified, some appear out of the blue and some disappear suddenly. The place-time diagram can be misleading at some places. It can occur that one structure passes another one which is represented as one dot in the diagram. It can also be the case that two structures merge in time. Apart from that, a relative good indication about the advective path in time is gained. These diagrams give the opportunity to estimate an average vortical structure generation frequency \bar{f}_{vor} as

$$\bar{f}_{vor} = \frac{1}{3} \sum \frac{N(x)}{\Delta t}, \quad x = 0.4, 0.6, 0.8 \quad (2.10)$$

where $N(x)$ is the number of vortical structures passing location x in time Δt . An average vortical structure advection velocity \bar{U}_{vor} was also determined from those diagrams. This was performed by fitting a linear curve through the clear paths. An average over the inverse direction coefficients of the curves gives \bar{U}_{vor} . The values of \bar{f}_{vor} and \bar{U}_{vor} are listed in table 2.2. These values show minor differences between the configurations. In first approach it seems that \bar{f}_{vor} and \bar{U}_{vor} for the rectangular imperfection case are higher but taking into account the accuracy by fitting and the chosen thresholds for the vortical structure identification procedure, no significant conclusions can be drawn. Therefore it is stated that $\bar{f}_{vor} \approx 1Hz$ and $\bar{U}_{vor} \approx 0.8U_\infty$ for all the configurations. Figure 2.8 shows all the detected center points. The spreading in y -direction becomes larger in downstream direction. The figure indicates that structures tend to move away from the wall. It can also be the case that a structure grows in time due to merging with another structure and thereby increases the y -coordinate of the center point.

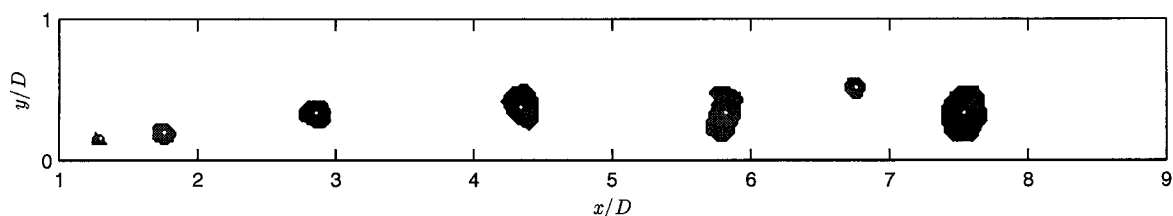


Figure 2.7: Vortical structures identified by the Γ_1 -method for configuration 1 at the same time as used to represent the instantaneous flow field in figure 2.2. A white dot represents the center point the vortical structure.

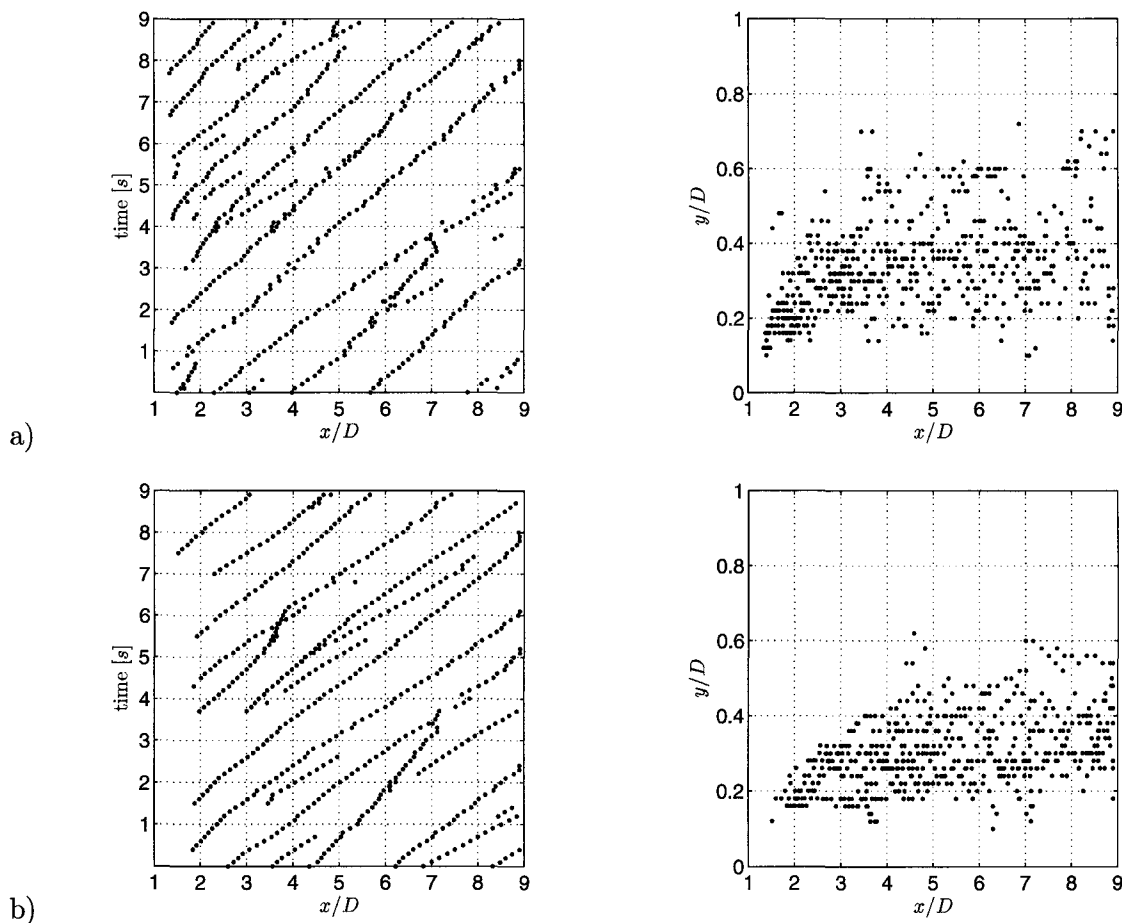


Figure 2.8: The left column: place-time diagram of downstream vortical structures, the right column: all the detected vortical structures for configuration a) 1 and b) 5.

Table 2.2: \bar{f}_{vor} and \bar{U}_{vor} .

configuration	\bar{f}_{vor} [Hz]	\bar{U}_{vor} [-]
1	0.8	$0.73U_{\infty}$
2	0.9	$0.80U_{\infty}$
3	1.0	$0.80U_{\infty}$
4	0.9	$0.73U_{\infty}$
5	1.1	$0.86U_{\infty}$

2.5 Discussion

The velocity ratio can significantly influence a flow field due to an increase in shear rate between the jet and cross-flow [17]. The velocity ratio was set to 0.25 in the computations, which in film cooling applications is $0.5 < VR < 2$. Therefore comparison with literature was conducted in a qualitative matter. The numerical predictions show similarities with studies found in literature. The lid-effect was described by Kassimatis et al. and Fitt et al. [9, 15]. This effect states that the cross-flow acts as a lid over the exit of the slot and thereby forcing

jet fluid to leave the slot through a reduced space near the trailing edge. This results in a high jet velocity value near the trailing edge of the slot and consequently in a lee shear layer after impingement. Both the high velocity near the trailing edge of the slot and the lee shear were detected in the numerical predictions. Kassimatis et al. reported a concave velocity distribution at the exit of the slot. The present velocity profile shows a similar shape (see figure 2.4).

The downstream circulation zone, detected in the mean flow (see figure 2.3), has been reported repeatedly [2, 15, 17]. They denoted this circulation as a recirculation bubble. The present computations pointed out that the downstream circulation on the mean flow is the result of an advected vortical structure. This means that the circulation zone is not a recirculation bubble. The downstream advection of a vortical structure that originates near the lee side of the jet was neither in experimental or numerical investigations reported. The presence of a stagnant leading edge bubble inside the slot, which was detected in all five the configurations, has not been reported.

Moerkerken [18] identified two shear layers on the mean flow. A first shear layer originates from the cross-flow boundary layer, starting at the leading edge of the slot. This shear layer was a structure between the jet and cross-flow. The second shear layer identified by Moerkerken started at the trailing edge of the slot and separates two flows. On the upper side it reaches U_∞ , while the lower side has low velocities. The zone with low velocities was indicated as a circulation zone. The two shear layers were also predicted by the numerical computations (see figure 2.5). The high values of \bar{v} at the exit of the slot near the trailing edge (see figure 2.4) were also detected by Moerkerken. The high cross-flow velocity, due to acceleration of the jet, was not detected in the study of Moerkerken, which can be due to a lack in measurement height. A turbulence intensity was also presented by Moerkerken. A comparison between that study and the present predictions shows that strong fluctuations dominate the circulation area downstream of the trailing edge in both cases. They were mainly caused by Tu_u near the wall and by Tu_v in the upper part. A difference is seen above the slot. The numerical model predicts a steady flow where the experiments clearly show an unsteady behavior.

It can be concluded that the numerical model predicts global flow features conform literature. Though differences were detected as well. Especially a steady windward shear layer and the advection of a vortical structure downstream of the slot. Since there are differences with the literature in flow characteristics and slot geometry, it is useful to preliminary determine the flow field by experimental means before additional effects are studied like grid/solver dependency and the implementation of the energy equation to determine a film-cooling effectiveness.

Chapter 3

Water channel experiments

3.1 Measurement technique and postprocessing method

Flow field measurements can be used to validate numerical predictions of a flow field induced by various film cooling slots as described in chapter 2. As a measurement technique particle image velocimetry (PIV) has been chosen. PIV is a quantitative whole field measurement technique. A schematic diagram of a measurement set-up is shown in figure 3.1. A sheet of green light ($\lambda = 532nm$) was generated by a dual-pulse Nd:Yag laser beam using a negative lens and a rectangular diaphragm with a width of $4mm$. Polyamid buoyant neutral seeding particles with an averaged diameter of $20\mu m$ in water were illuminated. A CCD camera was capturing images of particles with a resolution of 1008×1018 pixels during $68s$. The sampling frequency of PIV was set to $14.8Hz$ resulting in a total of 1005 correlated image pairs per measurement plane. The time (Δt) between two correlated images was varied between different measurements. The software package Pivview2C has been used to compute displacements of particles. In the experiments an interrogation window of 16×16 pixels, with an overlap of 50%, has been employed. This means that for every instantaneous measurement a two-dimensional pixel-displacements, on a 125×126 equally spaced rectangular grid, are obtained. The amount of wrong vectors is decreased by using a multi-grid interrogation scheme. Outlier vectors have been removed by setting a maximum displacement and maximum displacement difference. A median filter with a 5×5 kernel was used to smoothen the data. An equally spaced grid was placed in the field of view and captured by the CCD camera. This image has been used to determine a factor ($[pixel/mm]$) to convert pixel-displacements in velocities with Matlab scripting.

The accuracy of PIV results depends on various factors. In plane displacements $\Delta x, \Delta y$ should be $\Delta x \leq \frac{1}{4}\Delta X_0$, $\Delta y \leq \frac{1}{4}\Delta Y_0$, where ΔX_0 and ΔY_0 are the sizes of an interrogation window. Out of plane displacements should be $\Delta z < \frac{1}{4}\Delta Z_0$, where ΔZ_0 is the width of the light sheet. A perspective error increases when Δz is larger. Lost pairs can be formed, when a particle moves in or out the light sheet, in the time between two correlation images. High velocity gradients in one interrogation window should be avoided by zooming in or decreasing the interrogation window size. Alignment and positioning of a laser sheet and camera set-up should be as accurate as possible. When using a dual pulsed laser, like in these experiments, both laser sheets should have similar intensity and be projected along the same plane. All kind of reflections from internal and external surfaces, gas bubbles and especially sticking particles and should be avoided. In short, various factors influence the accuracy of PIV measurements.

In the situation that a particle is displayed by minimal six pixels, the correlation process itself has accuracies in the order of 0.1pixel [25, 4]. Particle image velocimetry is a useful measurement method to determine whole flow fields. Though it has its restrictions to the interpretation of obtained data. The behavior on a fine level can not be captured with this equipment. The images will always consist of blur and therefore decrease the accuracy. This results in a minimum turbulence intensity of 2% in the present study.

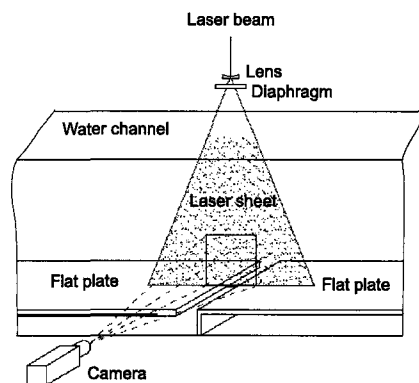


Figure 3.1: PIV set-up.

3.2 Experimental set-up

For these experiments an existing set-up, located in the laboratory of thermo fluids engineering at Technische Universiteit Eindhoven, has been used. The set-up consists of a closed-circuit recirculating facility with a $2500 \times 570 \times 450\text{mm}$ glass test section. Three centrifugal pumps are used to circulate water through the system. A volume flow can be adjusted manually by changing positions of butterfly valves, which have been mounted in the feed ducts. The maximum velocity in the test section is 200mm/s . Detailed information regarding this set-up is presented in Cremers [8].

The outline of the test section is schematically drawn in figure 3.2. A fluid enters the test section from the left. At the inlet of the channel two similar flow straighteners have been placed. Each flow straightener has been made out of squared channels with the width of 5.2mm and the length of 50mm . They have been provided with a screen with a typical mesh size of 1.5mm . This combination should bring the turbulence level to a value smaller than 2%. An acrylic flat plate ($1420 \times 570 \times 10\text{mm}$) was placed inside the test section, parallel to the channels floor, at a height of 65mm . The flat plate has a sharp leading edge (45°). One part of the fluid streams under the plate and generates the jet, while the other part flows over the flat plate and it forms the cross-flow. A suction unit has been placed under the leading edge of the flat plate, with a goal to prevent separation on the plate leading edge and also stabilize a boundary layer on the upper plate surface. A flow straightener was also placed under the plate to suppress large turbulent structures in the jet flow. Preliminary measurements have been conducted using the configuration without a flow straightener on the top of the flat plate. These measurements were performed with the cross-flow velocity $U_\infty = 200\text{mm/s}$ and $VR = 0.3$. Vortical structures are induced the cross-flow separation near the leading edge of the flat plate. This formation leads to the development of a turbulent boundary layer over the flat plate. Since the goal is to conduct experiments on two-dimensional flow, this

must be prevented. An additional flow straightener, 120mm downstream of the leading edge, has been placed to suppress a turbulent flow and to enable the development of a laminar boundary layer. To obtain the laminar boundary layer, the cross-flow velocity was set at $U_\infty \approx 90\text{mm/s}$, which results in a velocity ratio VR of 0.75. At the same height as the first flat plate, a second flat plate was placed 55mm downstream of the first plate trailing edge. In order to create an injection slot, the lower channel was blocked below the leading edge of the second flat plate. The lower flow impinges against this blockage and forms the jet. The jet flows through the injection slot and interacts with the cross-flow. The total amount of fluid leaves the test section at the right-hand side. A drawback of this configuration is that the velocity ratio VR can not be controlled.

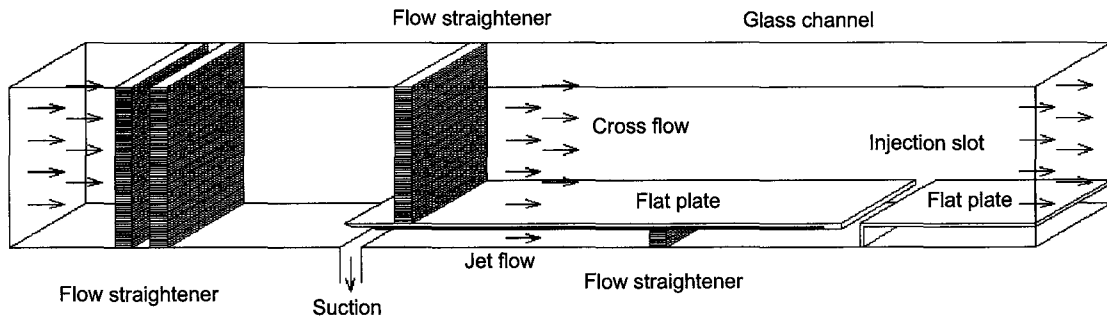


Figure 3.2: Schematic view of the test section in the experimental set-up.

Scaling of the set-up from, engine conditions to measurement conditions, was performed by the Reynolds number based on the cross-flow velocity and the length of the plate ($Re_x = \frac{U_\infty x}{\nu}$) and the jet velocity and the width of the slot ($Re_D = \frac{V_{jet} D}{\nu}$). In the experiments $Re_x = 1.3 \cdot 10^5$ and $Re_D = 3.8 \cdot 10^3$. In film cooling applications $Re_x = (1 - 2) \cdot 10^5$ and $Re_D = (1 - 2) \cdot 10^4$ (see [18]).

The influence of slot geometry has been investigated. Three different geometries of the slot were composed and they are illustrated schematically in figure 3.3. In order to label each configuration they are named: perfect slot, imperfect slot and inclined slot. The imperfect slot is composed to compare relatively small geometry variations with respect to the perfect slot. A first expectation of the perfect and imperfect slot is that a vortical structure will develop in the 90° corner. This vortical structure changes probably in shape and it induces three-dimensional motion. This should be avoided because of the comparison with a two-dimensional numerical model. A third configuration is composed to prevent this vortical structure. To that end a flat plate was mounted under an angle of 45° , which creates an ‘inclined’ slot. For all three configurations $D = 55\text{mm}$.

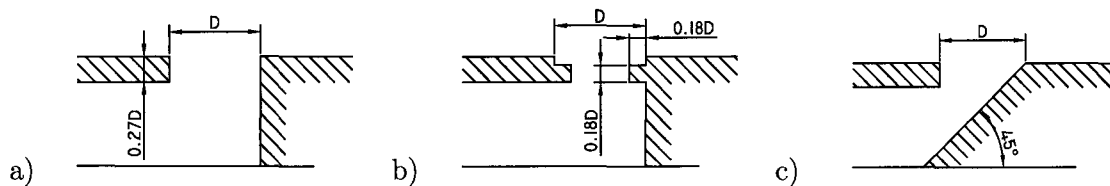


Figure 3.3: Schematic view of the three configurations. They are denoted as a) perfect slot, b) imperfect slot and c) inclined slot.

PIV measurements have been conducted along the central plane of the channel. The area above the plate covers a width of $8.3D$ and a height of $1.8D$, recorded at 5 different planes. In the perfect and imperfect configuration measurements were conducted under the plate and in the slot at two planes covering an area of $2D \times 1.0D$ (see figure 3.4). To get insight in the third component of the velocity, measurements were performed in a plane parallel to the flat plate. This has been recorded at three positions above the plate around $y = 0.3D$ in the case of the inclined slot, along an area of $5.8D \times 1.8D$ located above the slot. All measurements have been conducted with one camera, which means that all planes are measured at different times.

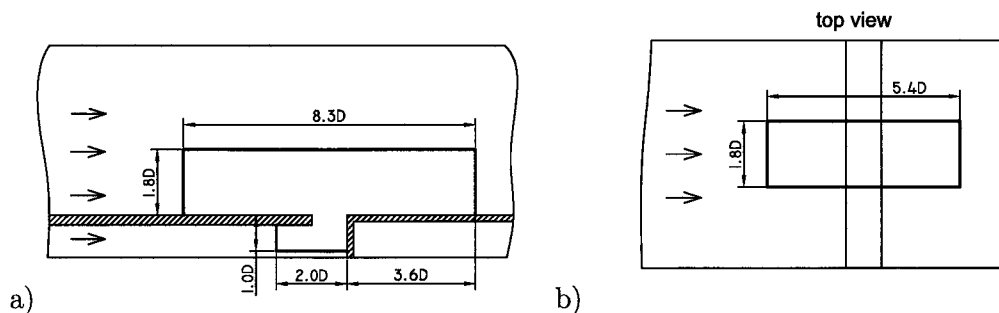


Figure 3.4: Schematic view of the measurement locations a) along vertical plane and b) the horizontal plane.

3.3 Preliminary flow description

This section describes the flow field of the ‘two-dimensional’ jet in the cross-flow. The origin of the coordinate system is set at the leading edge of the slot (see figure 3.5). Positions and velocities have been normalized by the slot width $D = 55mm$ and the cross-flow velocity $U_\infty = 90mm/s$ respectively.

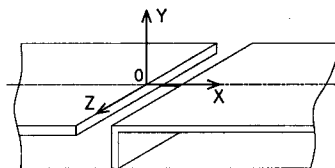


Figure 3.5: Location of the origin.

Figure 3.6 illustrates velocity fields generated through the perfect slot. The figure shows four instantaneous velocity fields which are measured at different times, at four positions. The cross-flow streams from left to right. The cross-flow boundary layer and the main stream are lifted due to the pushing of the jet. The jet fluid leaves the feeding duct with a highest velocity near $y = -0.3D$. The jet bends smoothly towards the exit of the slot where it has the highest velocity near the trailing edge. The jet issues into the cross-flow at $0.4D < x < D$ under an angle with the horizontal of approximately 70° . The jet is bent towards streamwise direction due to the composed cross-flow. An area with small velocities is present under the lifted boundary layer for $0 < y < 0.4D$ and $-0.3D < x < 0.4D$. Small velocities near the windward and lee side of the discharged jet induces a shear. Analyzing more time steps shows that these shear regions are not stable and that the fluid starts to rotate. This rotational

area travels through the interface showing a wavelike motion. Velocities are relatively low in an area bounded with the jet and flat plate. The flow within this area near the plate is directed in negative x -direction which indicate circulation. Further downstream, above the circulation zone, the flow is directed streamwise. Summarizing, the jet cross-flow interaction has an unsteady character and vortical structures are developing at the boundaries of the jet. Near the wall, on the lee side of the jet, fluid flows in negative x -direction.

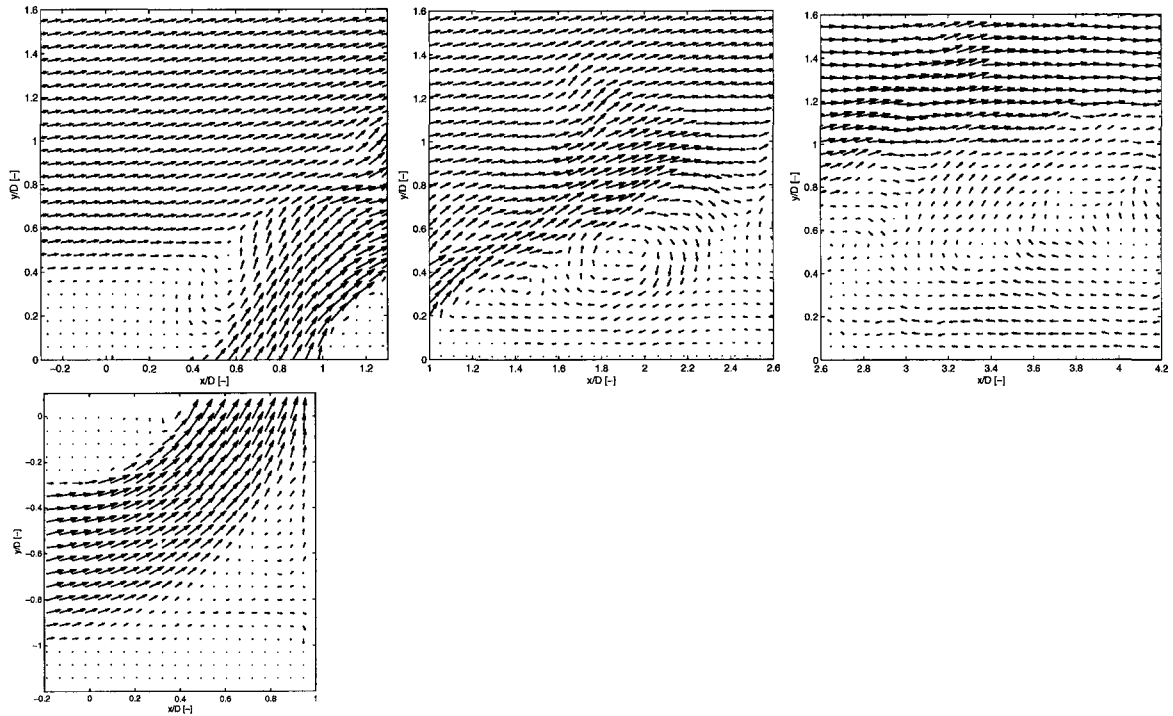


Figure 3.6: Instantaneous velocity vectors in the perfect slot configuration. Measurements were taken at different times.

3.4 Two-dimensionality

For a detailed comparison of PIV measurements with the two-dimensional numerical model, a two-dimensionality of the flow is essential. A first indication if the cross-flow is laminar is given by measuring the cross-flow boundary layer. According to the theory, the laminar boundary layer over a flat plate has a Blasius velocity distribution for x -values where transition from laminar to turbulent does not take place. The transition is affected by the Reynolds number, pressure distributions of the outer flow roughness of the plate and the turbulence intensity of the outer flow [24]. The time-averaged velocity \bar{u} (eq: 2.6) at $x = -3.6D$ above the plate is illustrated in figure 3.7. Also the theoretical Blasius boundary layer, based upon $U_\infty = \bar{u}_{max}$, is drawn in that figure. The boundary layer itself is in good agreement with the Blasius solution. Although an unexpected declination is detected in the outer flow where $y > \delta_{99}$, with δ_{99} a boundary layer thickness. It seems that the flow is accelerated due to an unexpected phenomenon of the test facility. The graph also shows the maximum and minimum velocities that were measured during the same sequence. The deviation is in the order of 10%. A boundary layer displacement thickness has been determined from the measurements by using

equation (see [24]):

$$\delta_1 = \sum_{i=1}^N \left(1 - \frac{\bar{u}_i}{U_\infty}\right) \Delta y, \quad \bar{u}_1 = 0, \quad \bar{u}_N = 0.99U_\infty, \quad (3.1)$$

where Δy is the distance between two grid points and δ_{99} a boundary layer thickness. With $\delta_{99} = y$ at a position where $\bar{u} = \bar{u}_{max}$, δ_1 is $0.302\delta_{99}$. The displacement thickness according to the theory is $0.344\delta_{99}$ (see [24]). It can be concluded with this deviation of 12% that the cross-flow boundary layer is close to laminar.

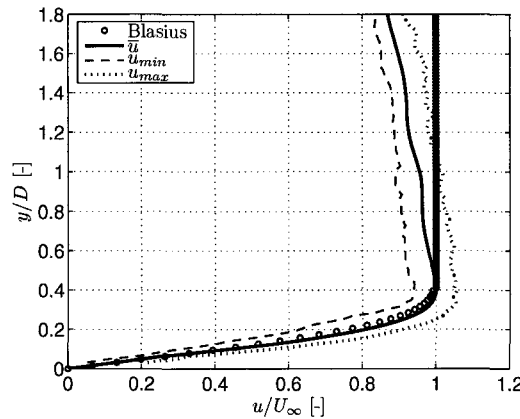


Figure 3.7: Time-averaged velocity distribution over the flat plate at $x = -3.6D$. The boundary layer is in good agreement with the Blasius solution. For $y > \delta_{99}$ a declination is obtained.

In order to check if the boundary layer is two-dimensional, an additional measurement has been performed, parallel to the plate. The horizontal plane was projected upstream of the slot in the cross-flow boundary layer around $y = 0.3D$. This measurement has been conducted in the inclined configuration. \bar{u} and \bar{w} are not constant in spanwise direction, as presented in figure 3.8. The instantaneous data shows that the flow is characterized by velocity streaks in the boundary layer. A streak with relatively high fluctuations is detected at $z = -0.6D$. Tu_u (eq: 2.7) reaches 15% at the position of the velocity streak. Tu_w is constant at $Tu_w = 2\%$. A positive \bar{w} in spanwise direction indicates that either the camera was positioned under an angle or the flow was partially directed in z -direction. Insinuating that the detection of positive \bar{w} is due to mistaken positioning of the camera, it can be concluded that a quasi-two-dimensional boundary layer interacts with the jet. Similar measurements were conducted downstream of the slot, see figure 3.8. In the far field $Tu_w = 13\%$ in addition with a low \bar{w} . Analyzing instantaneous data shows that the downstream flow is characterized by a stochastic shedding of vortical structures. Therefore, it is concluded that the area downstream of the slot is three-dimensional.

Main measurements were conducted in the xy -plane along the central plane. In order to check similarity with those measurements away from the central line, additional measurements were conducted at $z = -1.0D$ and $z = +1.0D$. An average velocity

$$\bar{U} = \sqrt{\bar{u}^2 + \bar{v}^2} \quad (3.2)$$

is determined for these measurements. The velocity profile of the jet fluid under the flat plate coincides between the z locations. With the knowledge that turbulence intensities are low in the jet feeding duct, it is concluded that the jet supply is two-dimensional.

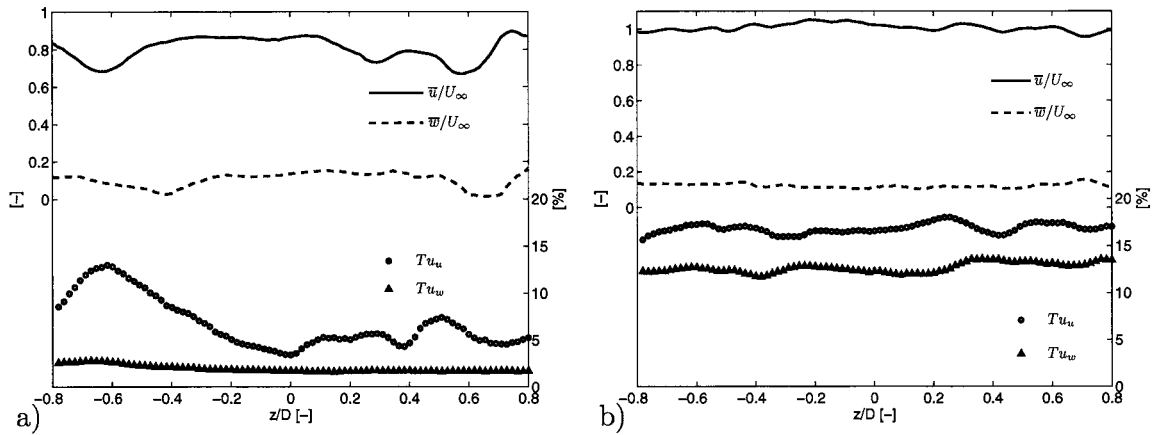


Figure 3.8: Average velocities and turbulence intensities in the horizontal plane around $y = 0.3D$. a) upstream of the slot $x = -1.5D$ and b) downstream of the slot $x = 2.5D$.

A comparison between the three planes above the plate is shown in figure 3.9. This figure shows the velocity distribution along $y = 0.5D$. Data are obtained from three successive planes which explains the interruption in the velocity profile near $x = -0.3D$. The velocity peak is at the same position with the same value. Large deviation is detected upstream of the peak value. Both profiles, away from the middle plane, show lower velocities than the main measurement plane. This can be caused by velocity streaks in the boundary layer. It should also be noted that the turbulence intensity goes to 15% in that area. In the far field the average velocity fields are similar. To conclude, the interaction between the two-dimensional jet and quasi-two-dimensional cross-flow boundary layer induces three-dimensional motion downstream of the slot trailing edge.

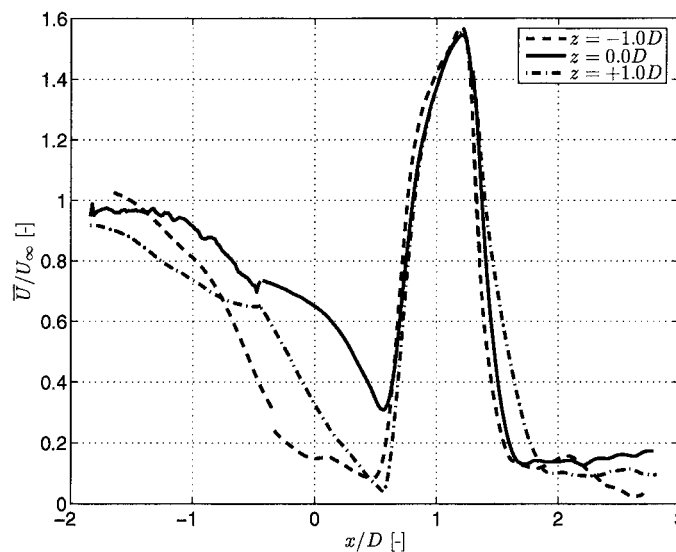


Figure 3.9: \bar{U} at $y = 0.5D$ in three xy -planes. The profiles were composed from three successive measurement planes at different z positions.

3.5 Mean flow

The time average velocity components \bar{u}, \bar{v} (eq: 2.6) and the turbulence intensities Tu_u, Tu_v (eq: 2.7) have been determined from the instantaneous data. Planes upstream of the slot have been used to determine the cross-flow velocity ($U_\infty = 90\text{mm/s}$). It should be noted that a variation in U_∞ is detected between the different measurements of 10mm/s . The turbulence intensities of the cross-flow are typically $Tu_u = 2\%$ and $Tu_v = 3\%$. The jet velocity V_{jet} is defined by $V_{jet} = \frac{1}{N} \sum_{i=1}^N \bar{U}_i$, along a horizontal line at $y = -0.27D$ inside the slot. A variation of 9mm/s is detected between different measurements. The jet velocity is $V_{jet} = 70\text{mm/s}$ which results in a velocity ratio $VR = 0.75$. Turbulence intensities of the jet flow under the plate are typically $Tu_u = 2\%$ and $Tu_v = 3\%$. The origin of the deviations in mean velocity can be unstable butterfly valves and the blockage of flow straighteners induced by gas bubbles.

Figure 3.11 shows streamlines of the mean flow for the three configurations. Streamlines start close to the plate on the left-hand side of the slots leading edge. It should be noticed that the beginning of these streamlines are not correct due to measurement errors close to the plate. Contour plots of \bar{u} and \bar{v} above and in the plane directly downstream of the slot are depicted in figure 3.10. In order to give more insight in the behavior of the flow, contour plots of Tu_u and Tu_v , above and in the plane downstream of the perfect slot, are depicted in figure 3.12.

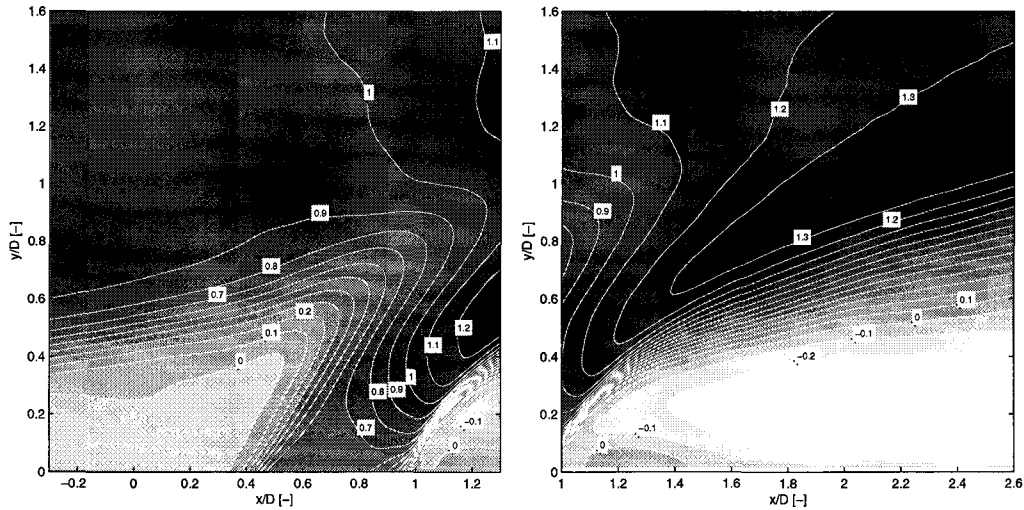


Figure 3.10: Contour plots of \bar{u} in the perfect configuration. A lifted boundary layer meets a shear layer from the slot. A second shear layer starts at the trailing edge of the slot. The jet is accelerated.

The jet flows over a vortical structure, which is present in the corner of the slot. It bents towards the exit of the slot and forms an obstruction for the cross-flow resulting in a lift up of the cross-flow boundary layer. This is illustrated in figure 3.13 where \bar{u} -profiles are drawn at increasing x -positions above the plate. The cross-flow streams over a circulation area which is present near the leading edge area. This circulation zone rotates in a negative direction and is named here windward circulation. The average velocities in the region of the windward circulation are small together with small turbulent intensities. This suggests the presence of a stagnant bubble. The jet exit is partly blocked by the windward circulation. A region

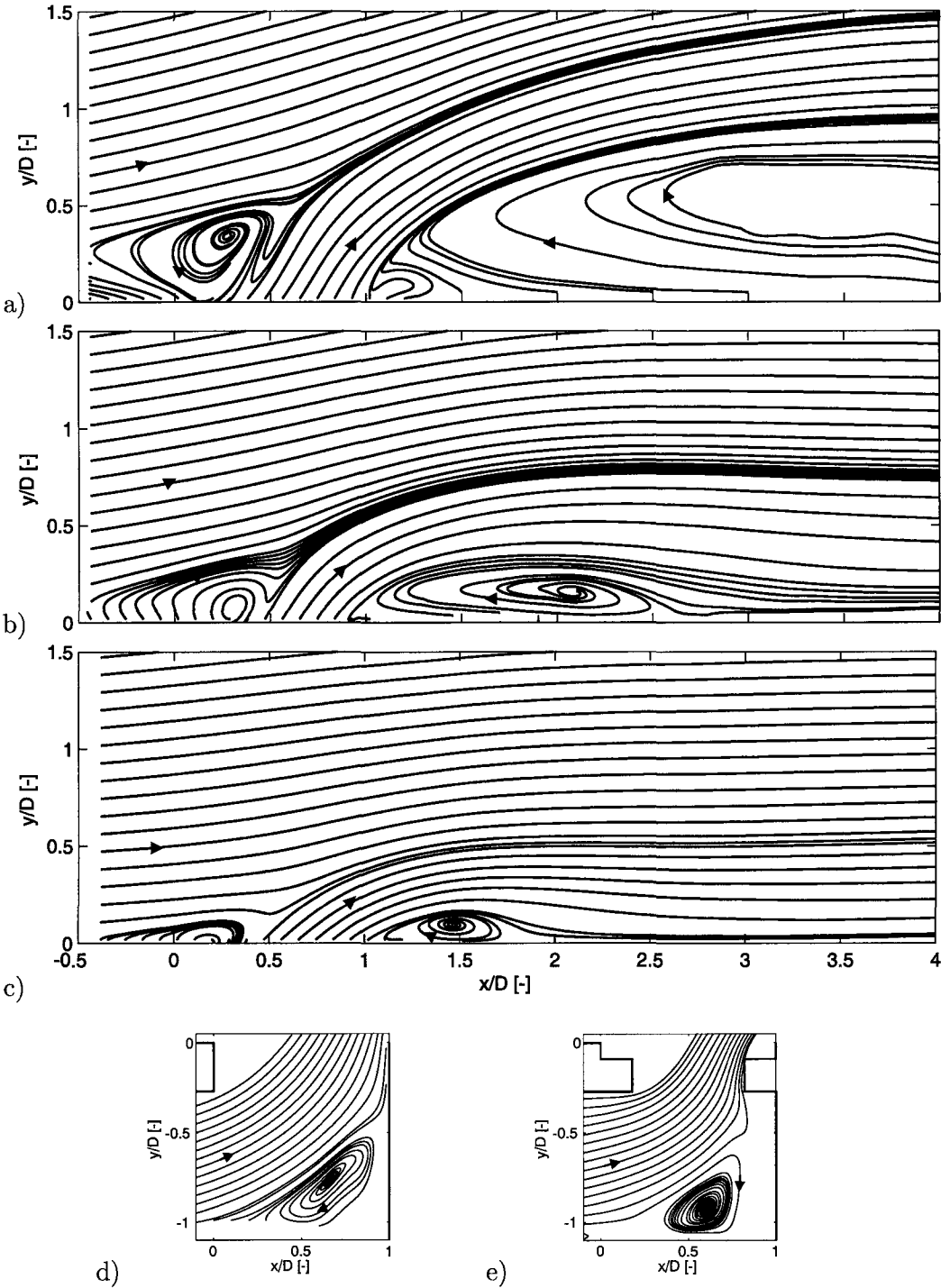


Figure 3.11: Streamlines of the average velocity field above the slot in the a) perfect b) imperfect and c) inclined case and below the slot exit in the d) perfect and e) imperfect case. Negative circulation is generated in the corner of the slot, near the leading edge of the slot and downstream. Jet penetration into the cross-flow is the highest in the perfect configuration.

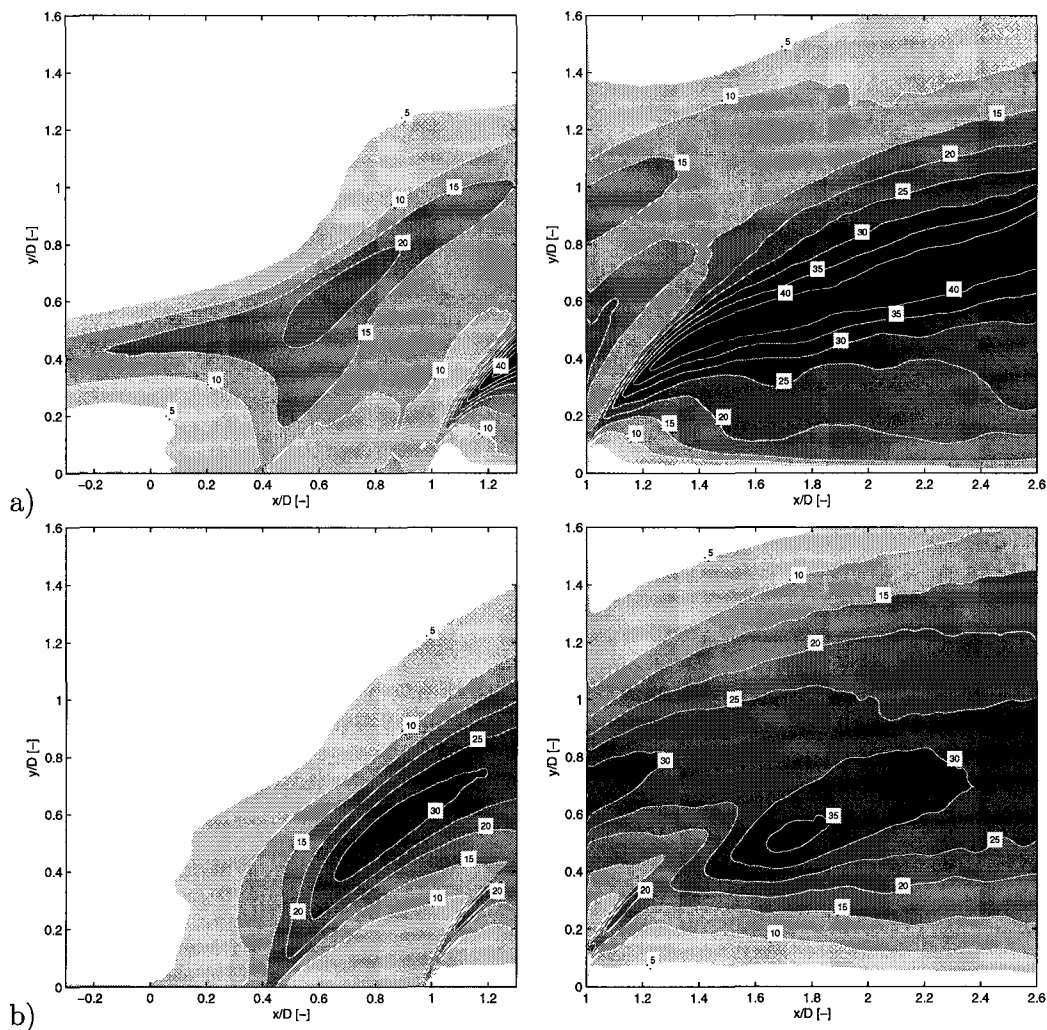


Figure 3.12: Turbulence intensities for the perfect slot configuration a) Tu_u and b) Tu_v . Two unsteady shear layers are generated by the jet cross-flow interaction.

with high velocity gradients can be distinguished above the slot. This region is named the first shear layer. The first shear layer starts inside the slot where the jet fluid separates from the bottom of the flat plate. It then follows the path of the streamline which indicates the border of the jet fluid in figure 3.11. The first shear layer is characterized by high fluctuations. The cross-flow side of the first shear layer is dominated by u -fluctuations where the jet side is dominated by v -fluctuations. Velocities in the first shear layer are not close to zero. It can be stated that the motion inside the shear layer can either be chaotic or more organized like advected vortical structures. A second circulation area is detected downstream of the trailing edge in between the jet and flat plate. It has a negative rotation and an elliptic shape. This circulation zone is named here leeward circulation. Velocities in the leeward circulation are small where Tu_u and Tu_v are relatively high. A second area with high velocity gradients, named here as the second shear layer, starts at the trailing edge of the slot. It bends around the leeward circulation and grows along the path of the streamline indicating the border of the jet and leeward circulation. The second shear layer diverges downstream from the trailing edge.

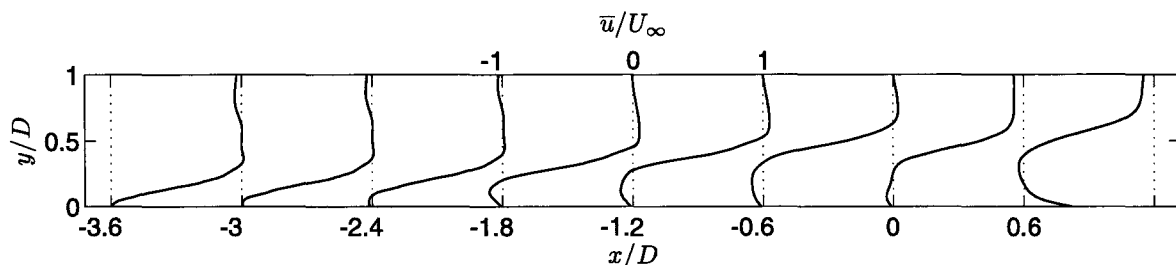


Figure 3.13: \bar{u} -distributions along equally spaced x -positions above the flat plate. The profiles show upstream separation of the cross-flow boundary layer.

The jet accelerates inside the slot. Acceleration is the lowest in the perfect slot where the exit of the slot has a width of $1D$. Followed by the imperfect case where it has a space between the imperfections of $0.64D$. The acceleration is the highest in the inclined configuration, where the jet fluid has a passage of $0.36D$ between the leading edge of the slot and the 45° inclined plate. The windward circulation is present in all three configurations. The center of this circulation is located at position $(0.3D, 0.3D)$ in the perfect case and $(0.3D, 0.1D)$ in the imperfect case. It is outside of the measurement plane in the inclined case. The size of the windward circulation strongly depends on the slot configuration. Although the centers are positioned differently, the blockage of the jet at the exit of the slot is approximately $0.4D$ for all three configurations. The first shear layer reaches a height of $1.5D$ in the perfect case, $0.75D$ in the imperfect case and $0.5D$ in the inclined case. This indicates the highest penetration in the perfect configuration. Also the leeward circulation is much higher in the perfect case, namely $0.9D$ where it is $0.3D$ in the imperfect case and $0.2D$ in the inclined case. The length of the leeward circulation in the perfect case is not determined because it falls outside the measured area. For the imperfect case it is $1.7D$ and in the inclined case $0.7D$. The angle, which the first shear layer has with respect to the horizontal, is approximately 70° at the exit of the slot in the perfect and imperfect case. In the inclined case it is 45° , which is equal to the inclination angle of the slot. In the first shear layer, Tu_u reaches 15% in the inclined case where it goes to 20% in the other two configurations. In the same area Tu_v reaches 30% in the perfect and imperfect case where it reaches 35% in the inclined slot configuration. The total area which is covered by the first shear layer is the largest in the perfect configuration and the smallest in the inclined case. The cross-flow velocity above the jet is higher in the imperfect case than in the inclined case. The second shear layer starts from the trailing edge of the slot in the perfect and inclined case. It starts from the right-hand side imperfection in the imperfect case. The upper region of the second shear layer is characterized by high velocities, with a highest region of $1.7U_\infty$ in the inclined case. Tu_u in this upper region consists of areas where $Tu_u = 40\%$ in the perfect and inclined configuration, where it is 50% in the imperfect case. Tu_v reaches 30% in the imperfect case where it is 35% in the other cases. Turbulence intensities in the slot corner area are $Tu_u = 10\%$ in the perfect configuration. In the imperfection case turbulence intensity goes to $Tu_u = 30\%$ near the right-hand side imperfection. Fluctuations in y -direction are not influenced by the imperfection and remain at $Tu_v = 10\%$.

Figure 3.14 shows \bar{u} and \bar{v} -profiles of the three configurations at a distance of $0.01D$ above the slot. All three profiles show a high velocity gradient at the windward side at $x = 0.4D$. At the lee side also steep gradients are present but at different x -positions. For the perfect case it is at $x = 1.0D$, for the imperfect $x = 0.9D$ and for the inclined case $x = 1.1D$. These steep gradients are the result of the lid-effect which enforces fluid to the lee wall of the slot.

\bar{u} in the inclined case has the highest peak at $1.4U_\infty$. In the imperfect case it is $0.9U_\infty$ and in the perfect case it is almost a flat profile with $\bar{u} = 0.6U_\infty$. The imperfect and inclined case have peaks in both the velocities at $x = 0.8D$ and $x = 1.0D$ respectively. In the perfect case a peak in \bar{v} is present with a maximum $\bar{v} = 0.9U_\infty$. The \bar{v} -profile is flatter in the inclined case than in the two other cases. Negative values of \bar{v} can indicate the presence of the windward circulation.

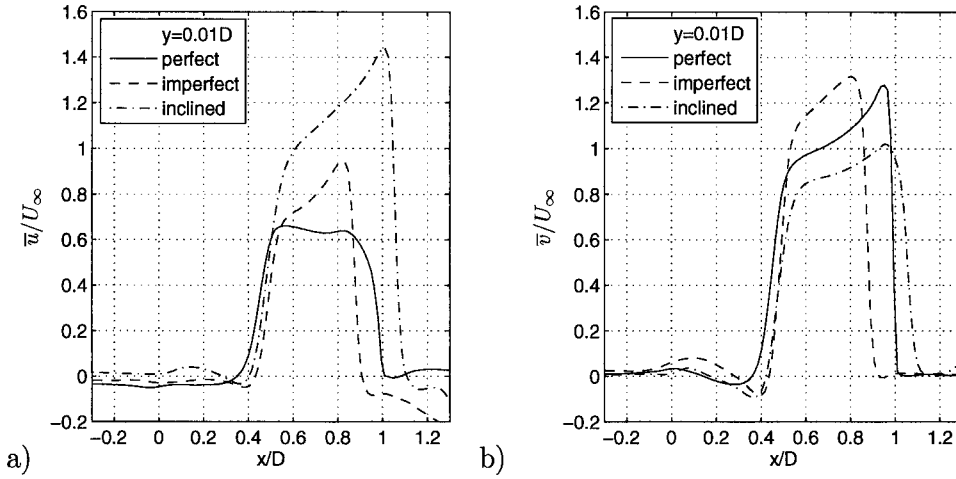


Figure 3.14: Mean velocity profiles $0.01D$ above the slot a) \bar{u} and b) \bar{v} . Two strong velocity gradients indicate a windward and lee shear layer. The jet is partly blocked near the leading edge of the slot.

Summarizing, the flow is characterized by flow features schematically drawn in figure 3.15. A negative windward circulation is present in the area where the jet separates and meets the boundary layer of the cross-flow. The flow along both shear layers is unsteady. Placing imperfections in the slot reduces the penetration height of the first shear layer into the cross-flow with 50%. A 45° inclined slot reduces the penetration height with 66%.

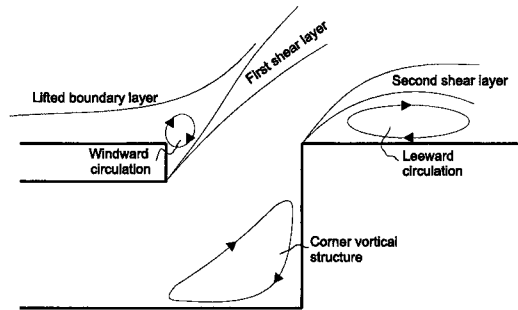


Figure 3.15: Schematic view of detected flow features.

3.6 Instantaneous flow

A first analysis of the flow field has been performed on statistical data. The instantaneous data can enlighten the flow within the corner region, first shear layer and downstream region. Snapshots of instantaneous velocity vectors for the three configurations, above and downstream of the slot, are depicted in figure 3.16. These figures illustrate the difference in

penetration height between the configurations. The cross-flow boundary layer is lifted the most in the perfect configuration and little in the inclined configuration. The windward side of the jet shows a wavy character. The downstream field contains vortical structures in the three configurations.

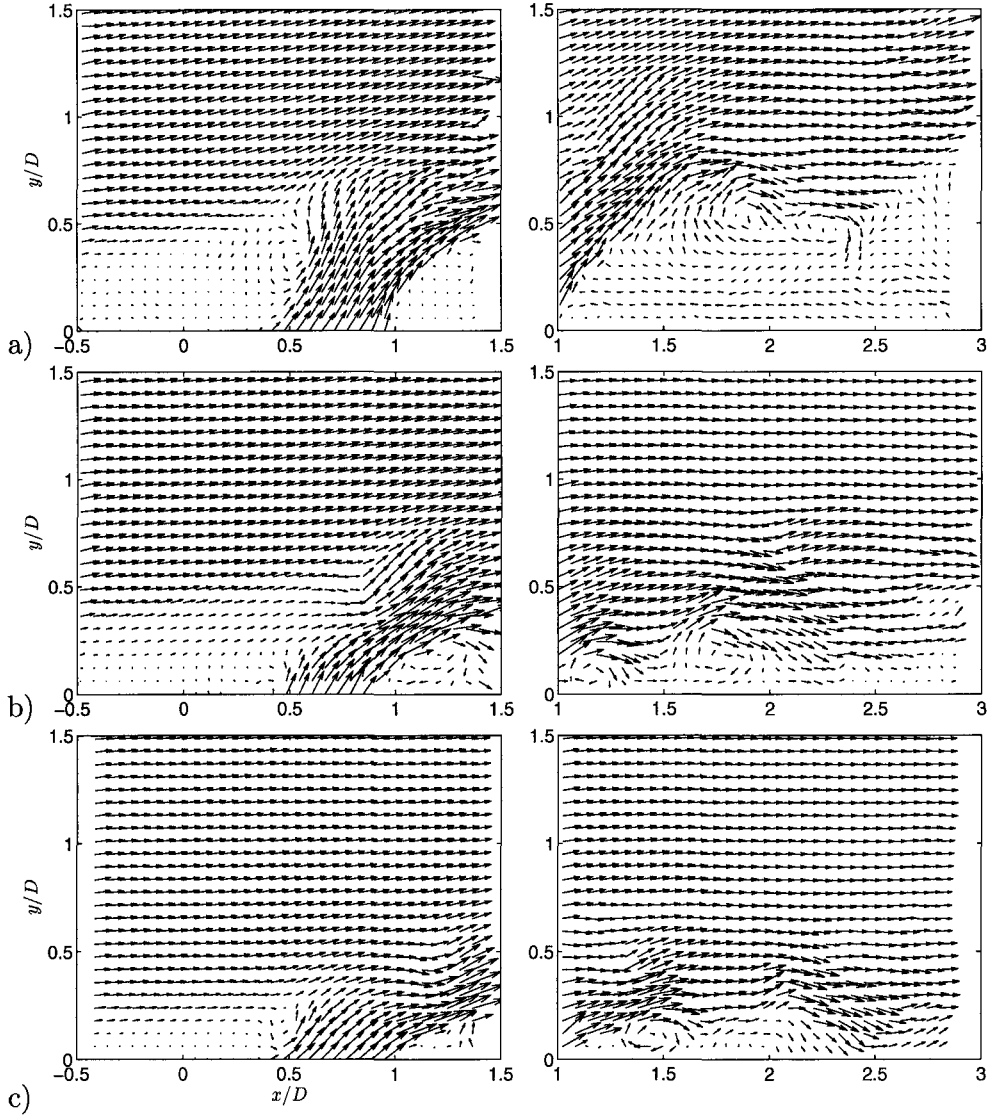


Figure 3.16: Snapshots of instantaneous velocity fields in the a) perfect case, b) imperfect case and c) inclined case. Measurements are taken at different times. The cross-flow boundary layer is lifted. The windward side of the jet is unsteady. Negative vortical structures are generated at the lee side. The perfect case shows a reverse flow downstream above the plate.

The analysis is focussed to detect vortical structures. It is chosen to make use of the Γ_1 -method which has been proposed by Graftieaux et al. [7] (see appendix A). They asserted in their work that a flow is locally dominated by rotation if $|\Gamma_1(t)| > \frac{2}{\pi}$. Therefore, it is decided to define all locations in the flow where $|\Gamma_1(t)| > \frac{2}{\pi}$ as a part of a vortical structure. The threshold N was chosen as 169 in this analysis. The main focus in this discussion is on the periodic movement of vortical structures. A vortical structure detected at the windward

side of the transverse jet is denoted with 'wv' followed by a 'p' for a positive and 'n' for a negative structure. Vortical structures generated at the lee side of the jet are named 'lv'.

In order to determine the behavior of the vortical structures, contour plots of $\Gamma_1(t)$ have been analyzed for all times in the three configurations. An example of eight successive time steps above the slot and downstream of the slot are depicted in appendix A. These figures were obtained in the inclined configuration. A time-dependent signal has been obtained from the $\Gamma_1(t)$ fields. This signal was employed to determine a vortical structure shedding frequency f_{vor} via the discrete fourier transformation (see [5]). First the observations in the perfect configuration are discussed followed by the imperfect and inclined configuration. Main differences compared to the perfect configuration are noticed. When vortical structures are referred to as large or small, this is with respect to the typical sizes.

Perfect configuration

Two types of vortical structures appear around the leading edge in the perfect case. A positive structure develops at the exit of the slot near the windward border of the jet, named as positive windward structure ('wvp'). This structure is advected along the first shear layer. The shedding is periodic with dominant frequencies $0.8Hz < f_{vor} < 2Hz$. A second vortical structure, at the leading edge, has negative rotation and it is named here as negative windward structure ('wvn'). This structure is present almost every time and 'dances' in the region bounded by the lifted cross-flow boundary layer and the jet. Its size varies drastically in different times. It is noticed that occasionally small negative structures are present in the cross-flow boundary layer which join the negative windward structure. Instead to be only one structure, it can also consist of more smaller structures. When the positive windward structure is advected, a part of the negative structure advects too. The size of these advected parts varies strongly from time to time.

A first view at the measurement plane downstream of the slot shows a field with a large diversity of unorganized structures. Though a shedding of a negative structure can be distinguished in the first part of the second shear layer ('lvn'). The shedding is periodic with dominant frequencies ranging from $0.8Hz$ to $2Hz$ along the second shear layer. The size of this lee structure mostly increases fast. It often merges with a previous advected structure which then form one larger structure together. This structure can be very large. The structure follows the path of the second shear layer which means that it not only moves in x -direction but also in positive y -direction. This larger structure occasionally breaks up in smaller structures but might as well preserves its shape. If the structure breaks, some of these structures travel further along the shear layer and some are moving into the circulation area under the transverse jet. A structure in the circulation area sometimes disappears or merges with the large structure that is formed by the advected structures. Small structures with a positive rotation appear regular in the area close to the surface of the downstream circulation. A small stagnant positive structure is detected in the circulation area immediately downstream of the second shear layer. The positive windward structure occasionally breaks up into smaller structures in the downstream field, but can also preserve its size till $x = 2.8D$. The negative windward structure deforms often in an elongated streamwise shape with sometimes a relatively large size, but can also stay small or vanish. If the positive windward structure does not break in the downstream field it normally follows its own path and does not penetrate the lee structure. When it breaks, smaller structures can follow their own path, and others can vanish or stay close to the lee structure and subsequently vanish. The

flow in the far field is mostly characterized by a diversity of large, small, positive and negative vortical structures.

The flow within the slot region is mostly dominated by a jet which flows smoothly towards the exit of the slot. A snapshot of this flow is depicted in figure 3.17. The fluid impinges to the perpendicular plate where it bents towards the exit of the slot. The velocity near the trailing edge is directed parallel to the flat plate. In that case several negative vortical structures are present in the interface between the bounded jet and the corner area. These structures oscillate in size and sometimes break up into more smaller structures. Than an unexpected phenomenon happens (see figure 3.17). A flow comes from the end wall which pushes the jet in upstream direction. This means that fluid comes from the backside of the jet. This reverse flow can push the jet in negative x -direction up to $x = 0.8D$. There is no characteristic time detected between the pushing and not pushing.

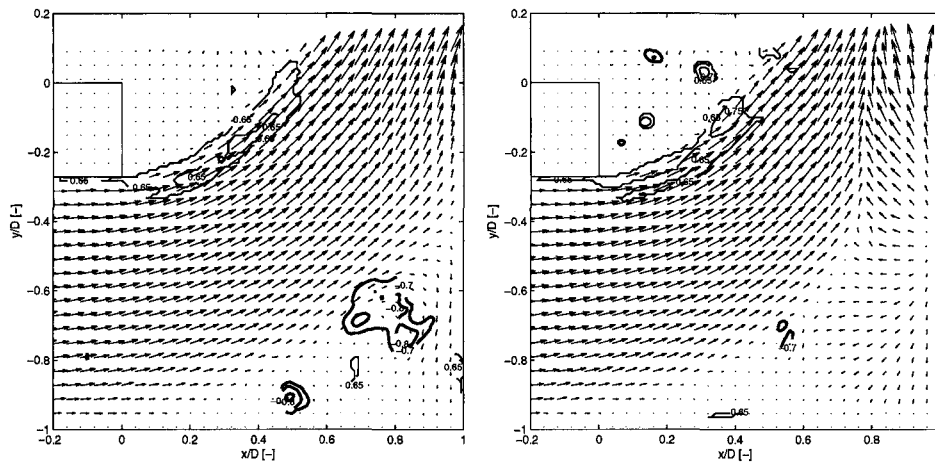


Figure 3.17: Snapshots of an instantaneous velocity field in the perfect case. Contour plots of $|\Gamma_1(t)| > \frac{2}{\pi}$ are depicted in the background.

To conclude, vortical structures were detected within the cross-flow boundary layer, a positive and negative structure shed the first shear layer, circulation is present upstream of the jet, the corner of the slot is mostly characterized by several vortical structures and a negative structure sheds the second shear layer. A schematic overview of the detected structures is shown in figure 3.18.

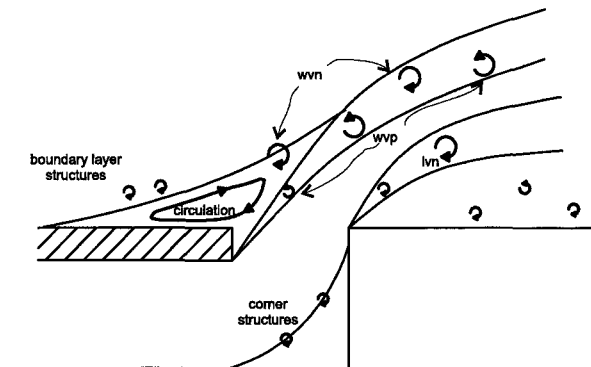


Figure 3.18: Schematic overview of identified vortical structures.

Imperfect configuration

Similar as in the perfect case a positive windward vortical structure ('wvp') is detected along the first shear layer in the imperfect configuration. This structure is advected with dominant frequencies ranging from $1.5Hz$ to $2.3Hz$. A negative vortical structure ('wvn') is present in the region bounded with the lifted cross-flow boundary layer and the jet. This negative structure increases in size until it breaks up in smaller structures. A smaller structure advects along the shear layer. This is a periodic behavior with a frequency similar to the shedding of the positive windward structure. The appearance of the negative windward structure in the downstream field differs during time. Sometimes it decreases in size but it can also maintain its size. Similar as in the perfect configuration, vortical structures are present in the cross-flow boundary layer. These structures join the negative structure near the leading edge or merge with the advected negative structure. At the trailing edge of the slot, a negative vortical structure ('lvn') is formed and advected with a shedding frequency of $1.5Hz < f_{vor} < 2.8Hz$ along the second shear layer. It starts as a small structure and mostly grows to a size that covers the space to the flat plate. It is advected downstream and shows all kind of behavior: stretching, splitting or merging. No space is left between the second shear layer and the flat plate, which is clearly present in the perfect configuration. This means that positive structures are absent near the plate. The lee structure tends occasionally to move away from the plate. The positive windward structure mostly breaks up in smaller structures which dissipate or are advected parallel to the plate. The positive windward structure is sometimes nicely advected over the lee structure and deflects towards the plate in the far field. The corner area is characterized by several structures that dance around in this area. These structures undergo mostly a negative rotation and appear in a broad range of sizes. Similar as in the perfect case, a back flow can be present on the right-hand side of the slot. In this case a small negative structure is induced near the right-hand side imperfection.

Inclined configuration

In the inclined configuration, the shedding of positive ('wvp') and negative ('wvn') windward vortical structures is detected in the leading edge area. They are advected with a frequency ranging from $2.1Hz$ to $2.8Hz$. The difference, compared to the perfect configuration, is that the negative windward structure appears as a small structure, grows and is advected in total along the first shear layer. Along the second shear layer, negative lee vortical structures ('lvn') develop and grow. They travel parallel to the plate in downstream direction. The lee structure is generated with a frequency similar to the windward frequency ranging from $2.1Hz$ to $2.8Hz$. Lee structures mostly start to break up at $x = 2.5D$. The positive windward structure preserves its size until $x = 4D$. Although it can break before it reaches $x = 4D$. The positive structure advects over the lee structure and follows a line parallel to the plate. The positive structure occasionally comes close to the negative lee structure and deflects towards the plate. The negative windward structure appears normally as an elongated structure in the downstream field where it decreases in size. It often vanishes before it reaches $x = 2.5D$. Compared to the perfect and imperfect configuration, the most clear repeating pattern is detected in this flow, both above and downstream of the slot.

Quantitative comparison

It can be concluded from the visualization of vortical structures that the positive and negative windward and the lee structure develop in all three the configurations. In order to investigate the influence of the different geometries to these structures, a quantitative comparison has been introduced. Due to the wide variation in shedding frequency, structures size and advective path, a statistical approach is required. ξ represents the percentage of the total time along which a point in the flow is dominated by rotation ($|\Gamma_1| > \frac{2}{\pi}$). Contour plots of ξ are drawn in figure 3.19, together with a time-averaged vorticity of the flow $\bar{\omega}_z = \frac{\partial \bar{v}}{\partial x} - \frac{\partial \bar{u}}{\partial y}$. Figure 3.19 shows that ξ matches very well with $\bar{\omega}_z$. The lifted cross-flow boundary layer contains vortical structures from $\xi = 10\%$ to $\xi = 50\%$ near the position where it meets the first shear layer. Also the beginning of the first and second shear layer have a high concentration of vortical structures. The jet core does not contain vortical structures. As the second shear layer diverges further downstream, ξ also covers a wider area. It can be concluded that both the first and second shear layer are characterized by vortical structures. In order to determine quantitative properties of the vortical structures, five control windows were chosen, as indicated in figure 3.19 with A to E. If centers of vortical structures are detected within such a window, a quantitative analysis is performed on this structure. The width of these windows has been chosen in such a way that the center of a structure is detected only ones, based upon an estimated advection velocity.

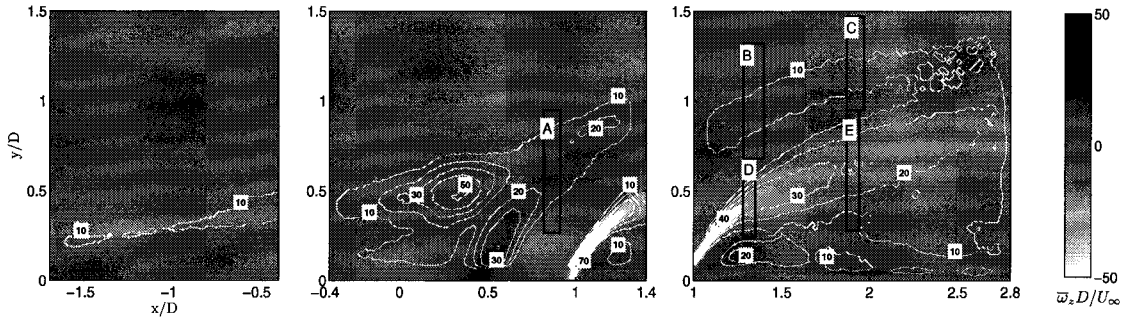


Figure 3.19: Contour lines of ξ with the time-averaged vorticity $\bar{\omega}_z$ in the background in the perfect configuration. A number indicates a percentage. The rectangular boxes marked from A to E are control windows.

The following properties of vortical structures are analyzed: advection velocity (U_{vor}), surface (s_{vor}), circulation (Γ) and average vorticity (Ω). The flow within the vortical structure can be decomposed as a sum of a local average velocity $\langle \underline{v} \rangle$ and a spatial fluctuating velocity $\hat{\underline{v}}$:

$$\underline{v} = \langle \underline{v} \rangle + \hat{\underline{v}}. \quad (3.3)$$

$\langle \underline{v} \rangle$ is defined by

$$\langle \underline{v} \rangle = \frac{1}{N} \sum_{i=1}^N \underline{v}_i, \quad (3.4)$$

where N is the amount of grid points within a vortical structure. A vortical structure advection velocity is the modulus of $\langle \underline{v} \rangle$ (eq: 3.4) and normalized by U_∞ :

$$U_{vor} = \frac{\sqrt{\langle u \rangle^2 + \langle v \rangle^2}}{U_\infty}. \quad (3.5)$$

The normalized surface of a vortical structure s_{vor} is defined as

$$s_{vor} = \frac{N\Delta x\Delta y}{D^2}, \quad (3.6)$$

where Δx and Δy are the spatial distances between two neighboring grid points and N the amount of grid points within a vortical structure. It is decided to restrict the analyse to structures with a minimum surface of 0.008. Circulation or strength is given by:

$$\Gamma = \frac{\Delta x\Delta y}{DU_\infty} \sum_{i=1}^N \omega_{z,i}, \quad (3.7)$$

which is a discretization of the formula that defines a normalized strength (see [10]). An average vorticity Ω of a structure is determined via

$$\Omega = \frac{D}{NU_\infty} \sum_{i=1}^N \omega_{z,i}. \quad (3.8)$$

A percentage of the total amount of vortices that are detected is represented by ς . Histograms, of the surfaces which pass through control window A and C, of positive and negative structures, are shown in figure 3.20. Histograms of the advection velocity, surface, strength and average vorticity are analyzed in appendix B. The most important issues are denoted here. The amount of data which has been used to compose the histograms, is listed in table 3.1.

The structures developed along the windward side of the jet undergo an acceleration. Further downstream, they decelerate in the imperfect and inclined configuration where this was not detected in the perfect configuration. The largest detected structure ($s_{vor} = 0.09$) in window A is detected in the perfect case. A typical size in window A, in the three configurations, is around $s_{vor} = 0.03$. The size of the positive and negative windward structure decreases along the first shear layer but occasionally a large structure is observed. The inclined configuration shows the most constant surface area. The circulation of the negative windward structure is low compared to positive structure and remains similar along the first shear layer in the three cases. The circulation of the positive windward structure in window A covers a broad range in the three configurations, where the most structures have a circulation of $0.1 < \Gamma < 0.4$. The circulation decreases along the shear layer and it decreases the slowest in the inclined configuration. The average vorticity of the negative vortical structure is low in all three configurations and remains low along the shear layer. The average vorticity of the positive structure is approximately similar in the imperfect and inclined case in window A and decreases along the shear layer. Ω of the structures generated in the imperfect case decays faster than in the inclined case. The vortical structures in the perfect case have initially a lower average vorticity and decreases as well along the shear layer.

Table 3.1: The amount of vortical structures analyzed in control window A to E, in the perfect (pc), imperfect (imc) and inclined (ic) configuration.

control window	A			B			C			D			E		
configuration	pc	imc	ic	pc	imc	ic	pc	imc	ic	pc	imc	ic	pc	imc	ic
positive	140	132	177	75	117	143	51	97	141	8	49	-	9	34	-
negative	92	117	99	40	176	77	29	105	60	116	274	251	98	195	147
total	232	249	276	115	293	220	80	202	201	124	323	251	107	229	147

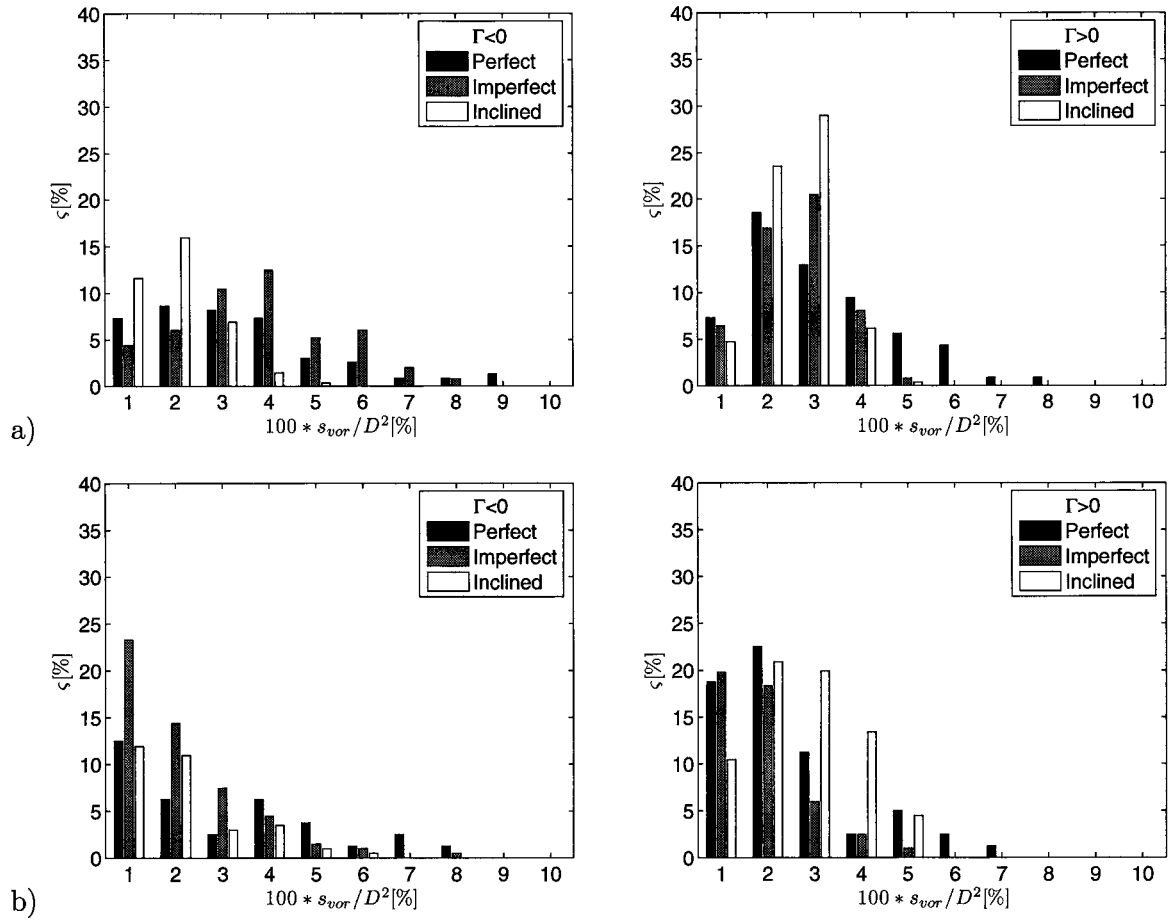


Figure 3.20: Histograms of vortical structure surfaces. Left column shows the amount of negative structures while the right one depicts the positive structures. Surfaces of control window a) A and b) C. The amount of smaller structures decreases along the first shear layer. Occasionally a large one is generated.

A small amount of positive structures is detected along the second shear layer in all three the configurations. They have a relatively small surface, circulation and average vorticity. Therefore it is decided to evaluate the negative lee structures only. The advection velocity in window D of the structures detected in the inclined configuration have a regular value around $U_{vor} = 1$. The velocities in the perfect and imperfect case are distributed over $0.6 < U_{vor} < 1.3$. In window E the velocities range from 0.1 to 1.5. Surfaces of the lee structures are the largest in the perfect and imperfect configuration and the most constant in the inclined configuration around $s_{vor} = 0.03$. They decrease in size along the second shear layer, although occasionally a large one is detected in the perfect and imperfect configuration. The circulation of the structures is spread along $0.01 < |\Gamma| < 1$ in window D. Mostly the circulation of the structures decreases in the downstream window E. A few structures are detected with a high circulation in the perfect and imperfect case. The average vorticity is the highest in the inclined configuration with a peak at $|\Omega| = 22$ and shows in the perfect and imperfect case a similar distribution where peaks are detected near $|\Omega| = 14$. The distributions in the three configurations are shifted towards lower $|\Omega|$ in window E.

The statistical analysis showed a general trend how the structures behave during their presence in the flow. In order to give inside the behavior of a single structure, a windward positive structure has been traced in downstream direction. A structure with a typical surface according to the histogram is chosen in the plane above the slot and downstream of the slot. This has been performed in the three configurations. The position of the structure is taken as their enters. The result is depicted in figure 3.21 where the individual quantities are drawn in downstream direction. It can be seen that the penetration height in the perfect configuration is the largest. The acceleration is seen in the advection velocity graph. The inclined case reaches its maximum first and starts to decelerate first as well. The average vorticity is high at the start and decreases fast in the beginning. Notice that these are examples of single vortical structures and that quantities can be rather different by following different structures. For example when the structure breaks up.

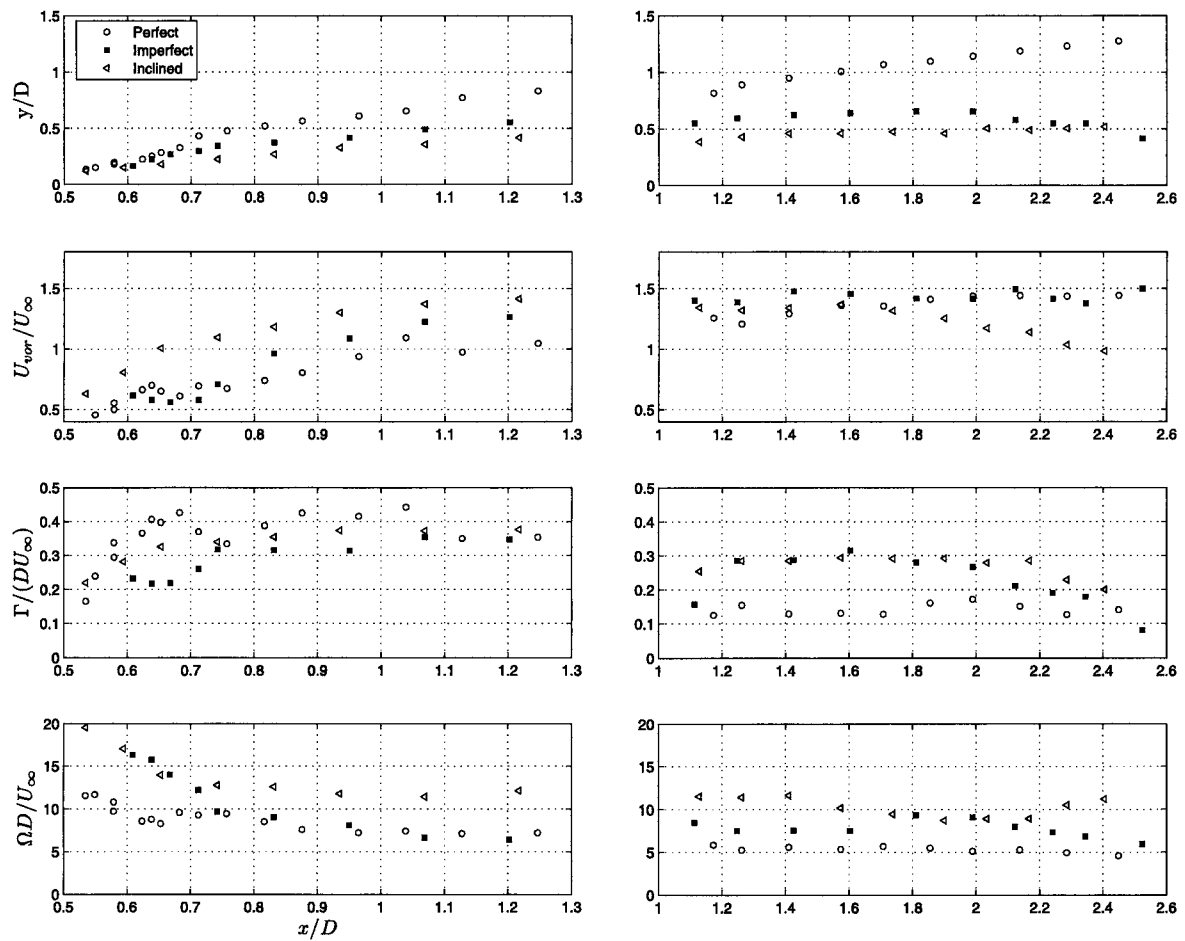


Figure 3.21: The path, advection velocity, circulation and average vorticity of a windward positive vortical structure detected in the three configurations. The left-hand side column is obtained above the slot where the right-hand side column is obtained downstream of the slot. Notice that the structures above the slot are different than the ones detected downstream of the slot.

All positive windward structures with a surface $0.015 < s_{vor} < 0.025$ detected in control window B have been quantitative compared in the perfect configuration. These structures have advection velocities $1.05 < U_{vor} < 1.40$, circulation $0.07 < \Gamma < 0.28$ and average vorticity $5 < \Omega < 12$. Which means that a specific surface is not consistent with other quantities.

3.7 Discussion

Previous analysis showed that the flow was characterized by vortical structures. Several vortical structures were identified and the ones with a repeating emergence have been named. In this section the probable origin of vortical structures is described.

A separation of the jet at the lower side of the flat plate, inside the slot, can be the beginning of the positive windward structure. The jet is forced to bend towards the exit of the slot due to the blockage by the perpendicular plate. This induces a high velocity of the jet near the separation from the flat plate. No-slip at the plate has to be satisfied which results in a strong shear near the separation edge. The shear is unstable after the separation. This instability causes the flow to rotate in positive direction. The rotation is the origin of the positive structure (see figure 3.22). This structure has a high average vorticity which decreases in time, attended by an increasing surface. One of Helmholtz vortex theorems stated that the circulation of a vortex tube remains constant in time [10]. This holds that $\Gamma = \Omega s_{vor} = const.$ In these experiments Γ increases over a short trajectory which indicates that the instability, set in after separation, enhances the circulation of the windward structure along a trajectory. A positive leading edge structure has been detected by studies on the flow field formation by hole-jet injection into a cross-flow. The formation of the positive windward structure can in that case be the result of in-hole jet separation along the windward wall of the hole due to penetration of the cross-flow into the hole [?, 3]. Which means that the formation of the positive windward structure in the present configuration has a different origin.

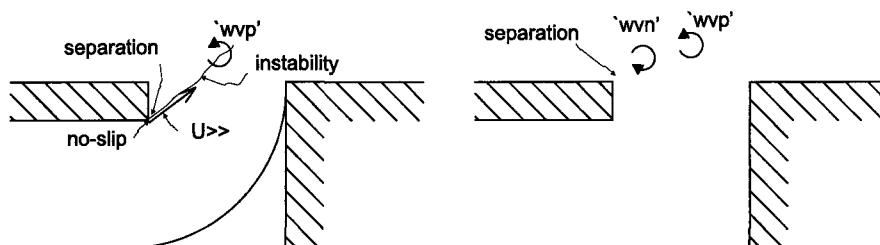


Figure 3.22: Schematic illustration of leading edge shedding. A positive windward structure is generated due to instability along the shear layer. A negative vortical structure sheds the shear layer due to separation at the leading edge of the slot.

A mechanism that contributes to negative circulation in the leading edge area is separation of the cross-flow boundary layer (see figure 3.13). An adverse pressure gradient parallel to the plate is induced until a point where $(\frac{\partial u}{\partial y})_{y=0} = 0$. The cross-flow boundary layer can not move into the high pressure area and will therefore deflect from the plate into the cross-flow [24]. This results in negative circulation upstream of the jet. The cross-flow boundary layer contains vortical structures. These structures have a negative rotation. They arrive at the circulation zone and increase the negative vorticity in this area. The relatively strong advected positive structure can attract cross-flow fluid towards the jet which subsequently results in separation of a patch of negative vorticity near the leading edge of the slot. This patch forms a negative vortical structure and sheds the first shear layer. The result is an alternated pattern of positive and negative vortical structures along the first shear layer.

The behavior of the corner vortical structure is probably related to the leading edge shedding. It was detected that this corner structure varied in shape during the measurements. A leading edge vortical structure induces velocity into its surrounding fluid, as can be explained

by the Biot-Savart relationship. This relationship considers a decomposition of a velocity field \underline{v} as an irrotational velocity field \underline{v}_1 and a rotational but divergence-free field \underline{v}_2 (see [10]):

$$\underline{v} = \underline{v}_1 + \underline{v}_2 \quad \text{with} \quad \nabla \times \underline{v}_1 = 0, \quad \nabla \cdot \underline{v}_2 = 0. \quad (3.9)$$

Biot-Savart relationship describes a velocity field \underline{v}_2 that is associated with a vorticity field:

$$\underline{v}_2 = -\frac{1}{4\pi} \iiint_{Vol} \frac{\underline{s} \times \underline{\omega}^*}{|\underline{s}|^3} dVol(\underline{r}^*), \quad (3.10)$$

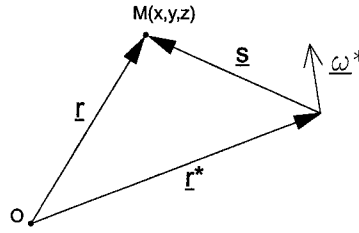


Figure 3.23: The Biot-Savart definition sketch.

where $\underline{\omega}^*$ is a vorticity distribution at position \underline{r}^* ($\underline{\omega}^* = \underline{\omega}(\underline{r}^*)$) and \underline{r} is a position vector at a point M of interest and $\underline{s} = \underline{r} - \underline{r}^*$. The volume integral is taken over the entire volume occupied by the fluid, denoted by Vol . This means that the positive and negative leading edge structures induces velocity in the corner region. Yao et al. [29] investigated flat plate trailing edge vortex shedding by three-dimensional direct numerical simulation. They stated that a shedding mechanism is not purely periodic and coherent in spanwise direction. Their work is related to the present study which means that the shedding of the leading edge vortical structures are not perfectly aligned in spanwise direction. The induced velocity in the corner region is therefore nonuniform. This suggests that the corner vortical structure oscillates in size, as schematically drawn in figure 3.24. This phenomenon can clarify the unexpected flow from the end wall of the slot that pushes the jet in upstream direction (see figure 3.17). Since it is impossible for flow to enter through the solid perpendicular plate, it has to be a product of three-dimensional motion. This motion can be induced by the unaligned corner structure via the Biot-Savart relationship.

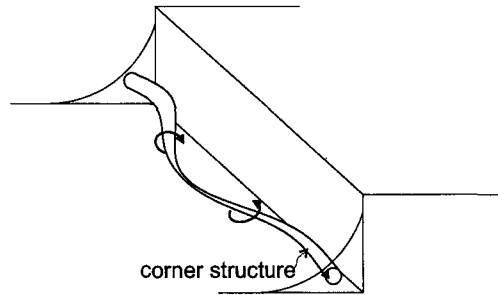


Figure 3.24: Schematic illustration of an unaligned vortical structure in the corner of the slot. The behavior of corner structures is probably connected to the shedding at the leading edge of the slot. The corner structure can induce three-dimensional motion due to cross-section variations and unaligned appearance.

Najjar and Balachandar [19] found in their experiments a quasi-periodic shedding of vortical structures at a rectangular trailing edge. It had an appearance of periodicity but never repeats itself. It even exhibits short bursts of strong shedding with intervals of relatively weak shedding in between. These findings can elucidate the wide range of f_{vor} detected in the present study.

Two main differences concerning the first shear layer can be distinguished between the three configurations. First, the average velocity in the near region of the shear layer is the lowest in the perfect case and the highest in the inclined case. Second, the penetration height of the first shear layer into the cross-flow is the highest in the perfect case and the lowest in the inclined case. It seems that the velocity influences the advection velocity, shedding frequency and average vorticity of the positive windward structures. These properties are the lowest in the perfect case and the highest in the inclined case, which is in accordance with the average velocities. The penetration height probably influences the properties of the windward vortical structures along the shear layer. The circulation decreases fastest in the case of a high penetration (perfect case) and slowest if the penetration is low (inclined case). Also structures break up fastest in the case of high penetration.

It was concluded that the circulation of one vortical structure can increase or decrease significantly between different times. This means that the vortical structure probably consists of more smaller structures that break or merge during the different times because the circulation of the structure should, within a calculation error, remain similar or decrease by means of diffusion.

The negative lee structure that develops near the trailing edge of the slot is the result of separation of a boundary layer. The velocity near the exit of the slot is relatively large, as was shown by the average velocity profiles in figure 3.14. An unstable shear layer is present after the separation. The instability causes the flow to rotate in negative direction which results in the lee structure. Because of a higher velocity near the trailing edge, compared to the velocity near the leading edge of the slot, the absolute circulation and absolute average vorticity of the lee structure is higher than of the positive windward structure. Again it seems that the velocity and penetration height determine the structures properties. In the inclined configuration, where the average velocity was the highest, the largest average vorticity was detected. The width range of advection velocities and circulations of the structures can be explained by the fact that the lee structure often breaks or merges in the downstream field. This influences the advection velocity and the circulation of vortical structures. In the perfect case, where the penetration is high, the structures are free of wall friction and have the opportunity to travel, merge or break up. In the imperfect and inclined case a lee structure develops and is advected parallel to the plate where it is under influence of wall friction. This results in a fast deformation of the structures and subsequently a fast dissipation.

Mixing characteristics of the main flow and coolant jet are important in film cooling applications. A high mixing rate enhances hot fluid to reach the downstream surface which decreases the insulation properties of the film and therefore the film cooling effectiveness. Two-dimensional PIV measurements do not reveal mixing characteristics of the flow. An other measurement technique, for example Laser Induced Fluorescence (LIF), should be applied in order to get insight in the mixing.

In film cooling a continuous supply of coolant fluid provides an insulating layer between a hot main stream and a protected surface. Penetration of coolant flow into the hot main stream should be low (see Glezer [14]). Miron et al. [17] concluded from their slot jet experiments that downstream circulation decreases the film cooling effectiveness. When this circulation is

absent or small, mixing is the weakest or the insulation effect is good. They also concluded that the optimal jet injection angle seems to be between 30° and 40° . In these measurements the downstream circulation, represented by average velocity streamlines, was smallest in the inclined configuration. Also the penetration of the jet is smallest in the inclined configuration. This makes the inclined configuration the most favorable. But, mixing of the cross-flow and coolant flow should be as less as possible. Since in all three the configurations a diversity of vortical structures develops, which enhance the mixing, none of these configurations is well suited. For instance the windward structures that occasionally deflect towards the surface can deteriorate a film cooling effectiveness. The major reason that these configurations do not satisfy film cooling applications is the high velocity of the jet near the separation from the flat plate inside the slot. This is probably the origin of vortical structures that enhance a mixing rate.

The slot geometry and flow characteristics were significantly different than the ones applied in the numerical model discussed in chapter 2. The velocity ratio was 0.75 instead of 0.25 and the Reynolds number based on the length of the plate was $1.3 \cdot 10^5$ instead of $2 \cdot 10^5$. The geometry subjected in the experiments induced a strong shear inside the slot which was absent in the numerical model. This means that a validation of the numerical predictions with the experimental data described in this chapter does not satisfy. An adapted numerical model with a slot geometry similar as in the experiments can enlighten the quality of numerical predictions.

Chapter 4

Numerical experiments Part II

4.1 Adapted numerical model

Limitations of the experimental set-up were the reason to conduct slot jet experiments by using different configurations than initially subjected in the numerical simulations. The measurements pointed out that the slot jet injection into a cross-flow is three-dimensional. Nevertheless it is interesting to predict two-dimensional results, by using a similar geometry and flow condition as employed in the experiments. Therefore a new two-dimensional numerical model has been composed to calculate a flow field under approximately similar conditions as in the water channel experiments.

Preliminar computations predicted a flow field which seems to contain elements of success, therefore Comsol's Navier-Stokes module has been used to compose the new model. The injection slot geometries correspond to the 'perfect' and 'inclined' slot configuration subjected in PIV measurements (see section 3.2) have been used in the new computations. The perfect case is chosen as a benchmark in this chapter and the inclined configurations is submitted as a reference. The model and its main dimensions are illustrated in figure 4.1. The domain was composed with a converging outlet. This was adapted to prevent singularities during the solving process near the outflow boundary of the domain. A singularity can occur when reverse flow is present near the outlet. The converging outlet artificially diffuses vortical structures that are the origin of a reverse flow. The length of the domain has been extended to prevent an upstream influence on the field of interest by this artefact.

The applied boundary conditions are illustrated in figure 4.1. The boundaries representing the inlet of the jet and the cross-flow, both need an continuous inflow condition. These conditions are prescribed with the time-averaged velocity profiles obtained by PIV measurements. Due to an uncomplete jet velocity profile, a linear extrapolation was applied towards zero at the lower wall. A velocity distribution measured $-3.6D$ upstream of the slots leading edge were implemented as a main stream velocity. The height of the measurement field was $1.8D$, which is smaller than the y -domain in the numerical model. The velocity at y -positions above $y = 1.8D$ were uniform as the velocity measured at $y = 1.8D$. A slip/symmetry condition was assigned at the top boundaries of the model. A neutral boundary condition was applied as an outlet condition at the right-hand side of the domain. The pressure was set to zero at the intersection point of the upper and outflow boundary. All other boundaries were provided with the no-slip condition $\underline{v} = 0$.

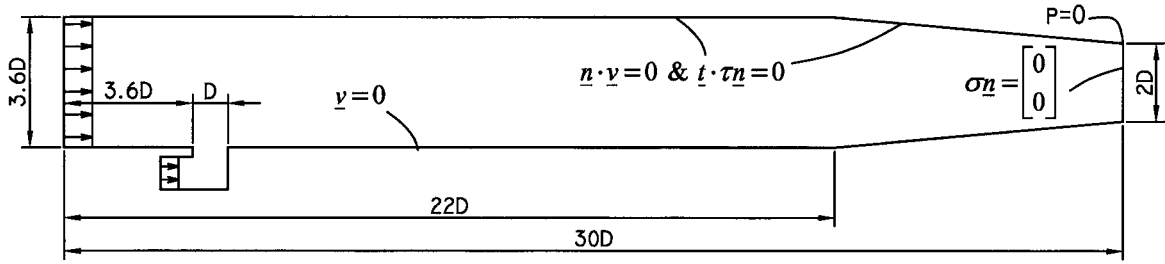


Figure 4.1: Numerical model with main dimensions and boundary conditions. The boundaries without indication have a no-slip boundary condition.

To solve the problem an unstructured mesh was used. The knowledge from the measurements was used to strategically refine the mesh at locations where velocity gradients are relatively high. Refinement was adapted near the slots leading and trailing edge and near the walls with the no-slip boundary condition. A coarser mesh was implemented along the converging outlet of the domain. This mesh configuration resulted in approximately 170.000 degrees of freedom.

An initial value for the main calculations was gained by solving the model with $u_{t=0} = 0$ and $p_{t=0} = 0$ along the whole domain. The solution at $t = 30s$ was an initial value for the main calculations. Comsol solved the model for an additional time of 68s, which was equal to the total sampling time in the PIV measurements. Data was stored by Comsol every $\Delta t = \frac{1}{14.8}s$, which was equal to the sampling frequency in the PIV measurements. The data has been imported into Matlab for postprocessing along a rectangular grid of $-D < x < 8D$ and $-1.2D < y < 2D$ with spatial step $\Delta x, \Delta y = 1mm$.

4.2 Preliminary simulation results

It is interesting to pinpoint the start up behavior of the flow before discussing the main predictions. Initial effects such as development of the cross-flow boundary layer towards the jet, oscillation of a corner vortical structure and wiggling effects near the leading edge area were seen during the first 30 seconds. Figure 4.2 a) till c) show snapshots of this start up behavior in the slot regions. Figure 4.2 d) shows the flow at $t = 30s$. The velocity vectors represented in this figure are normalized by their lengths to illustrate the direction of the flow. a) shows a positive vortical structure above the slot and a negative structure near the leading edge of the slot. b) and c) do not show those structures near these locations. The corner vortical structure in a) shows a clear triangular shape where b) and c) show a different form. The mentioned regions fluctuated during the initial stage of the calculations. The fluctuations become less severe in time and finally lead to a stable corner structure and a stable windward side of the jet in the form depicted in figure 4.2 d). A vortical structure develops at the trailing edge of the slot and is advected downstream. This process does not become stable.

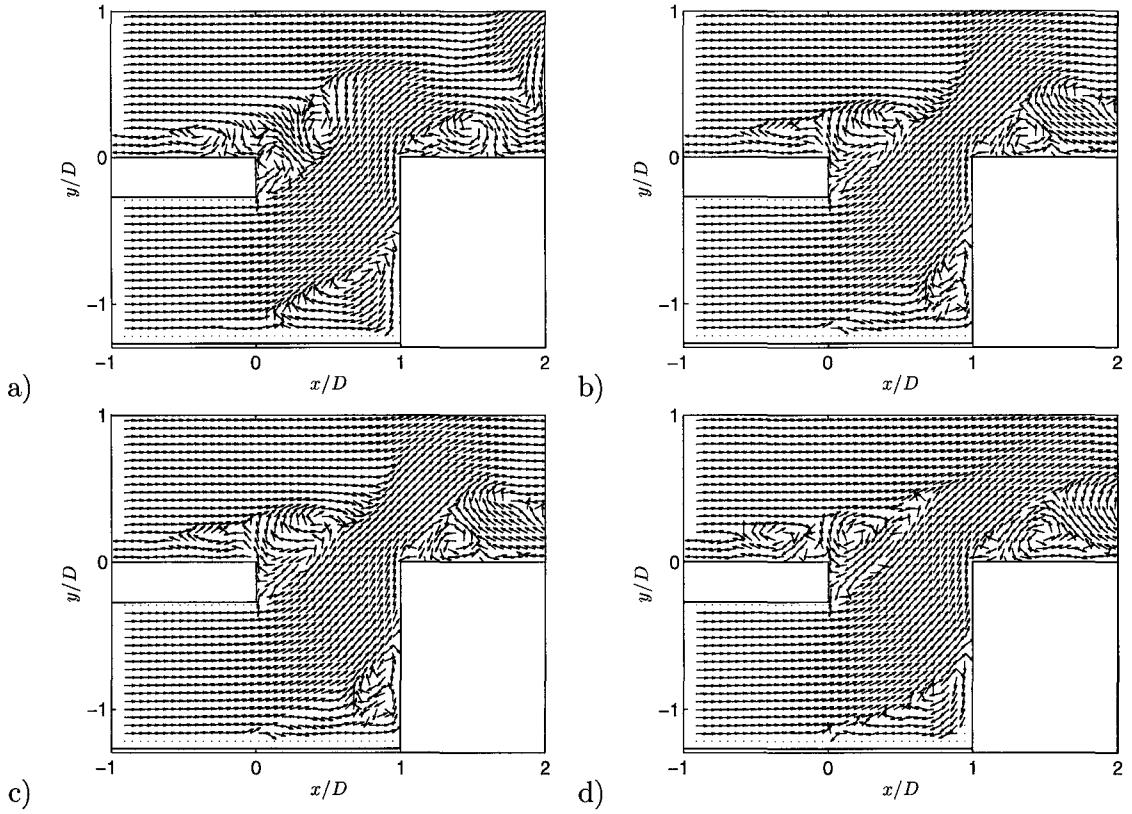


Figure 4.2: Snapshots of the predicted flow represented by velocity vectors normalized by their lengths. a), b) and c) are obtained during the start up process. The windward side of the jet and the corner of the slot is unsteady during the initial stage of the computations. These regions become stable at d) $t = 30s$.

4.3 Mean flow

Statistical data are represented by using streamlines of time-averaged velocity \bar{u} (eq: ??), contour plots of time-averaged velocity and contour plots of turbulence intensities (shown in figures 4.3, 4.4 and 4.5). A lifted cross-flow boundary layer and a windward shear layer are present. The jet fluid flows over a stagnant circulation zone in the corner of the slot and subsequently bends towards the exit of the slot. A relatively high jet velocity is present at its separation from the horizontal wall. The jet leaves the slot along $0.4D < x < D$ with a relatively high velocity in the vicinity of the slots trailing edge. It bends in streamwise direction after emerging from the slot. The windward side of the jet meets the cross-flow boundary layer near $(0.6D, 0.4D)$. Turbulence intensity is zero along the windward shear layer which means that the flow is steady in this region. Two stagnant negative circulation zones are present under the lifted cross-flow boundary layer. The jet is accelerated from $\bar{u} = 0.8U_\infty$ at the entrance to a maximum of $\bar{u} = 1.6U_\infty$ near $(2.2D, 0.8D)$. The cross-flow accelerates from $\bar{u} = U_\infty$ to $\bar{u} = 1.4U_\infty$ around $(1.2D, 3D)$. The streamline that separates the jet and cross-flow reaches a maximum height of $1.2D$ near $x = 1.2D$.

A downstream region enclosed by the jet and the wall is covered by two circulation zones with a total length of $3.3D$. A first circulation zone has its center near $(1.8D, 0.2D)$ and has a

positive rotation. The second circulation zone, with a center near $(3.3D, 4D)$, has a negative rotation and is significantly larger than the first one. It has an elongated shape and surrounds the first one. Turbulence intensities are reaching levels of 70% in this area. y -fluctuations are mainly present in the center of the large negative circulation zone and x -fluctuations are dominant close to the wall and in a region near $(2.4D, 0.5D)$. The velocity gradient is relatively high along the streamline that encloses the downstream circulation. This indicates the presence of an unsteady second shear layer. The far field is characterized by turbulence intensities to 30%.

The streamlines of the inclined slot configuration show that the penetration height of the first shear layer into the cross-flow is lower than in the perfect case. The height of the downstream circulation is also lower in the inclined configuration.

Summarizing, the two-dimensional jet cross-flow interaction induces two stagnant negative circulation bubbles under the lifted cross-flow boundary layer and one in the corner of the slot. A steady shear layer is present along the windward side of the jet and an unsteady shear layer is present along the lee side of the jet. The mean flow characterizes the downstream region by two counter-rotating circulation zones.

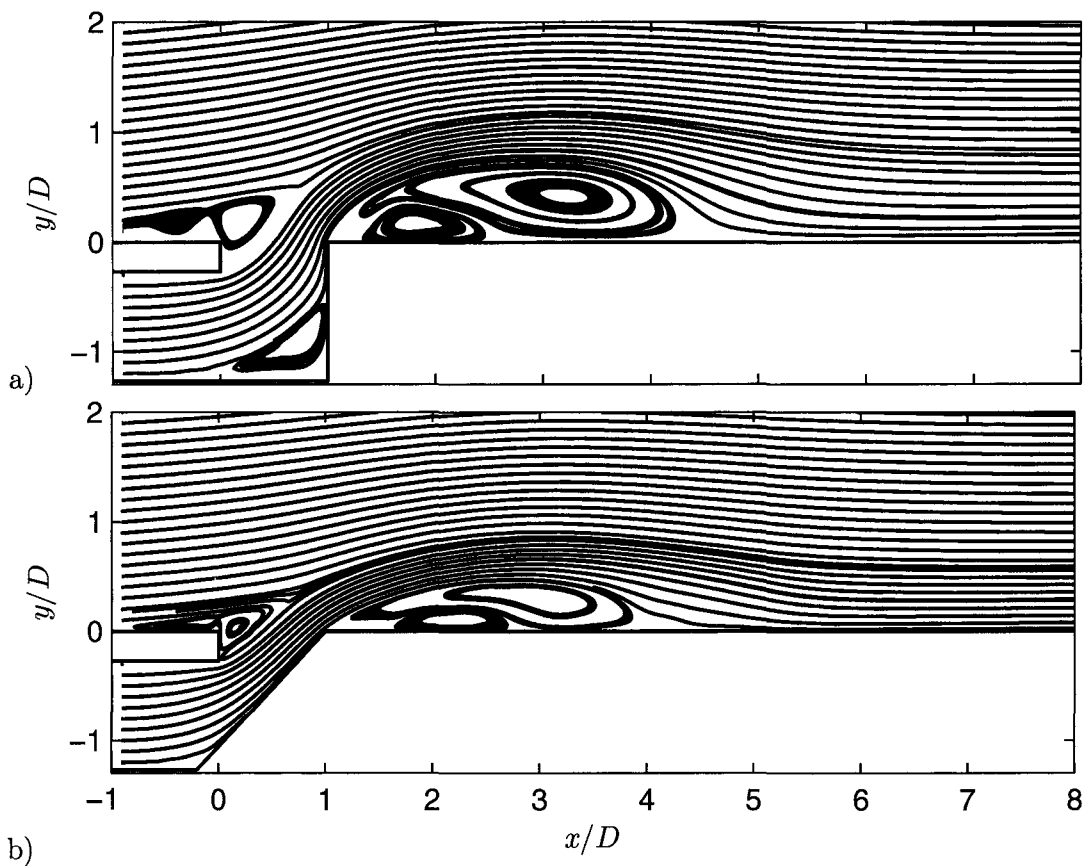


Figure 4.3: Streamlines of time-averaged velocity for the a) perfect and b) inclined configuration. The corner of the perfect slot is dominated by a negative circulation. A negative circulation is generated upstream of the jet. The downstream field shows a small positive circulation zone and a large negative one.

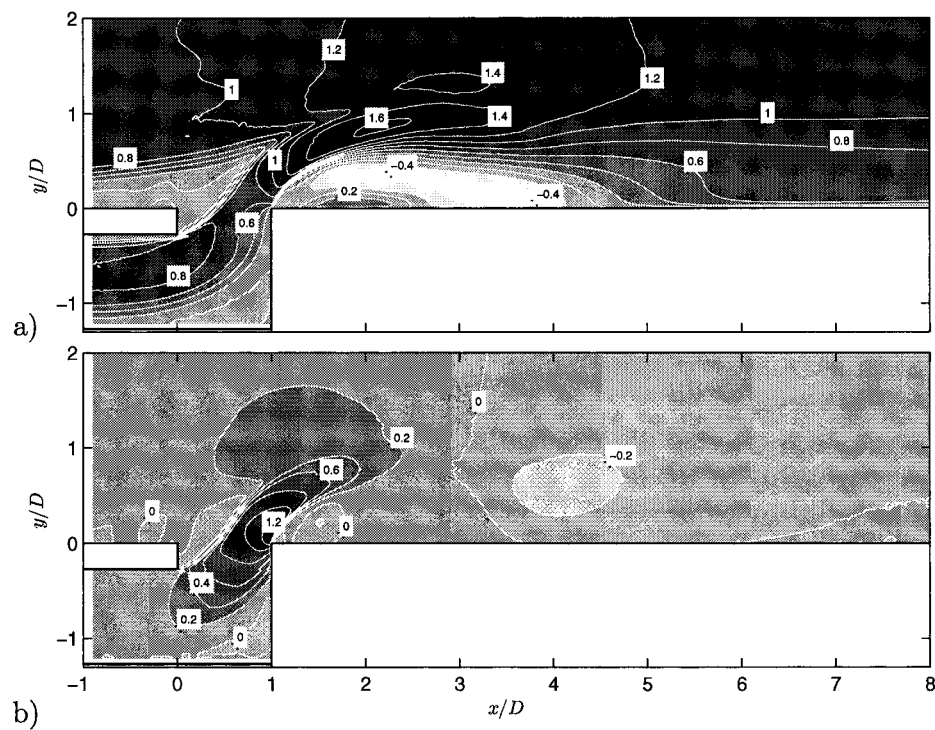


Figure 4.4: Contour regions of the mean flow in the perfect configuration in a) x -direction and b) y -direction. The jet accelerates after it emerges from the slot. The cross-flow is accelerated till above the jet. A shear layer starts at the leading edge of the slot and at the trailing edge of the slot.

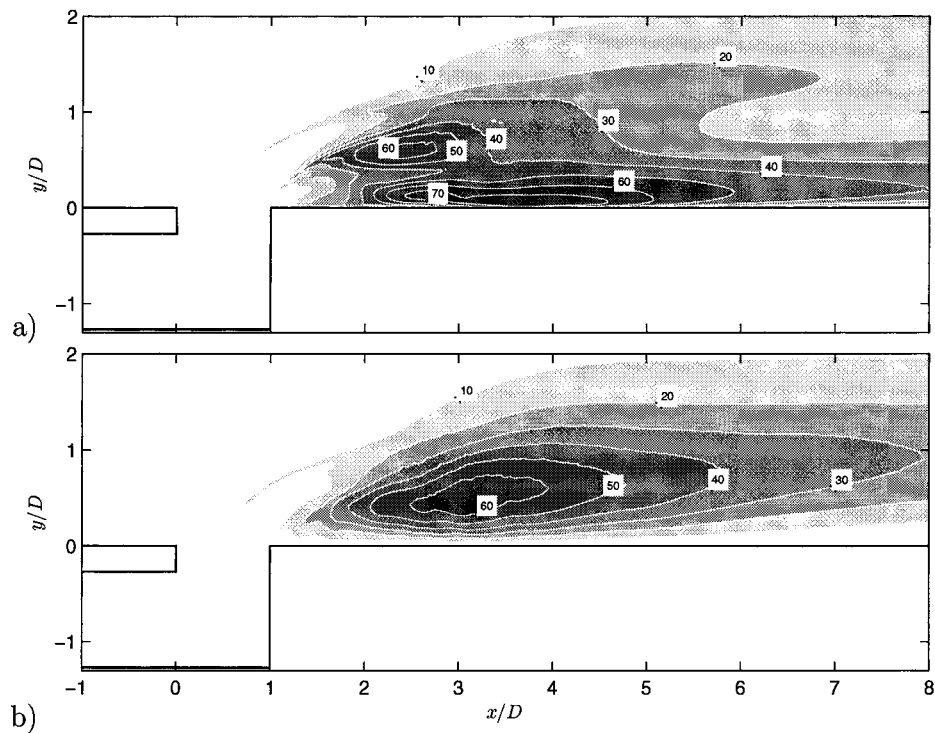


Figure 4.5: Contour regions of turbulence intensity in the perfect configuration in a) x -direction and b) y -direction. The downstream field is unsteady.

4.4 Instantaneous flow

A flow field at $t = 50s$ is illustrated by instantaneous velocity vectors in figure 4.6. The regions inside the slot, and above the slot are similar as represented by the mean flow. The downstream flow differs. A negative vortical structure, with its center near $(2.2D, 0.3D)$, covers a region between the bounded jet and the wall. A second negative vortical structure is detected further downstream and has its center near $(3.9D, 0.3D)$. The sizes of these two vortical structures are similar. A third negative vortical structure is detected near $x = 7.2D$. This structure is characterized by low velocities near the wall and it seems to have a larger size than the other two.

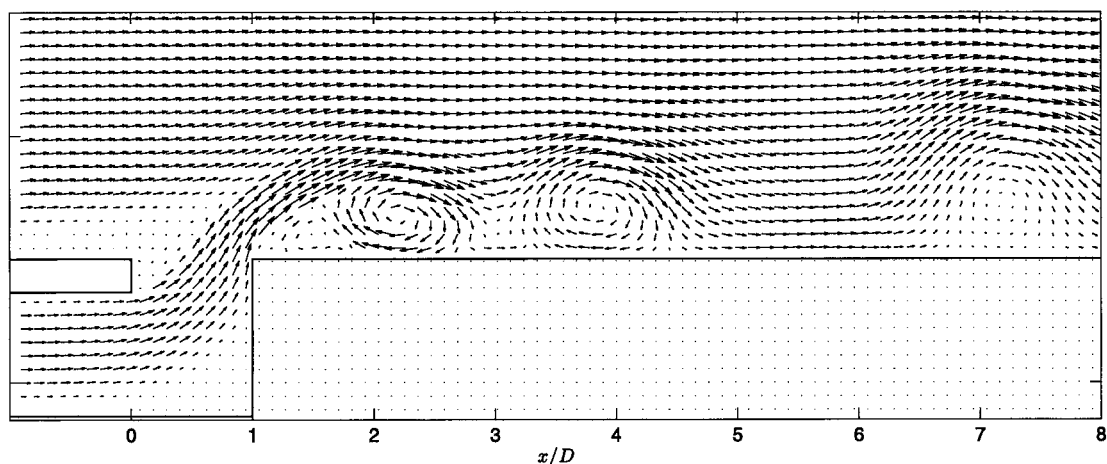


Figure 4.6: Instantaneous velocity vectors for the perfect case at $t = 50s$.

A movie of the instantaneous flow fields showed that the three negative vortical structures originate near the lee side of the jet. A vortical structure starts to develop, grows, merges with an previous advected structure and shed downstream. This process is illustrated in figure 4.7 with three instantaneous flow fields. Two structures (A and B) are present in the near field of the slot, they merge together and subsequently form a circular vortical structure which starts to travel downstream. This process has a periodic character. The size of a circular vortical structure differs for different structures. The size depends on the size of structures that merge together. The time between advection along the wall of two successive circular vortical structures is not regular and differs from $3s$ to $7s$.

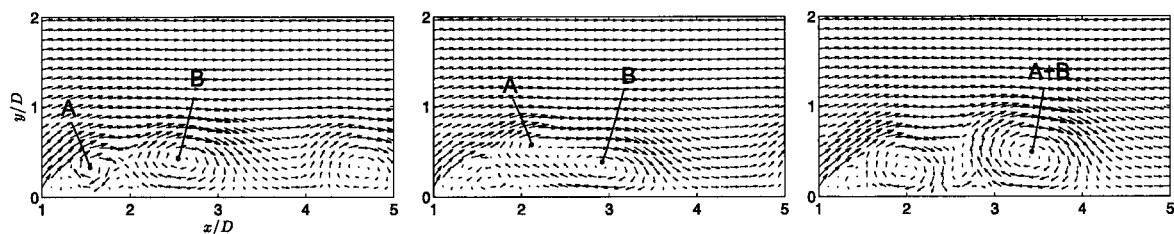


Figure 4.7: Merging process of two vortical structures downstream of the slot. The vectors represent instantaneous flow fields.

The Γ_1 -method (see appendix A) has been applied on the instantaneous flow fields to identify the advected vortical structures. The threshold was chosen as $N = 169$ and $|\Gamma_1| > 0.8$. Their centers are represented in a place-time diagram depicted in figure 4.8. The diagram shows short and long trajectories. A short trajectory represent the path of a vortical structure which merges with the following vortical structure. They form the circular vortical structure and are advected downstream. An average advection velocity is $\bar{U}_{vor} = 0.8U_\infty$ and an average vortical structure generation frequency of the circular structures is $\bar{f}_{vor} = 5Hz$.

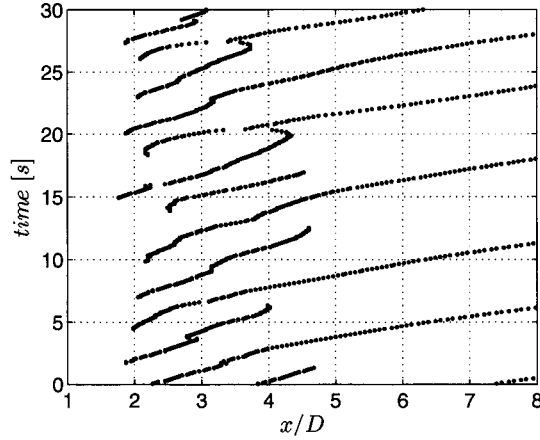


Figure 4.8: Place-time diagram of negative vortical structures detected in the perfect case for a time of $30s$.

The flow fields induced by two slot geometries were numerically predicted. These geometries were similar as applied in water channel measurements. A comparison between the computed flow fields and the experimental data is described in the following chapter.

Chapter 5

Comparison

5.1 Numerical predictions with slot jet experiments

A qualitative comparison between the numerical predictions and the experimental data verifies that several flow features appear in both cases. Namely: the development of a negative circulation in the corner of the slot, acceleration of jet fluid through the slot and in the first stage after injection, a first and second shear layer, a lifted cross-flow boundary layer, acceleration of the cross-flow to a maximum above the bounded jet and circulation upstream and downstream of the jet. Differences were also noticed: unsteady flow behavior inside the slot, upstream of the slot and above the slot in the experimental data, which where steady regions in the numerical simulation, just one downstream circulation zone by the time-averaged experimental data, which consists of a counter-rotating pair in the numerical predictions and downstream shedding of a negative vortical structure which in the numerical results remains its size along its path and in the experimental data breaks, merges or dissipates.

A quantitative comparison has been performed by the mean flow. Profiles of time-averaged velocity near the exit of the slot ($y = 0.07D$) are shown in figure 5.1. The computed velocities show a very good overall agreement with the experimental data. The largest deviations are present near the windward side of the jet. Numerical simulations show a stable shear in this region, where the experimental data is smoothen because of unsteady behavior. The numerical values between $x = 0$ and $x = 0.4$, near the exit of the slot, are linked to the stagnant circulation bubble upstream of the jet. The negative numerical \bar{u} values, just above the slot for $x > 1$, are induced by the positive circulation downstream of the orifice. Profiles of time-averaged velocity at different positions along the plate in x -direction are provided in figure 5.2. The computed axial and wall-normal velocities agree very well for $x \leq D$. Deviations close to the wall at $x = 2D$ are connected to the positive circulation in the downstream field. The \bar{u} -profile at $x = D$ and $x = 2D$ shows an ingestion that indicates the first shear layer. The shear layer is more severe in the numerical predictions than in the experiments. The computed \bar{v} -distribution deviates significantly in the far field from the measurements. It is approximately zero along y -direction at $x = 4D$, where it is negative in the computed case. This is the influence of the vortical structures that spend a relatively long time in that region due to the merging with a new advected vortical structure.

The velocity distributions near the exit of the slot in the inclined configuration shows a good overall agreement (see figure 5.1). A deviation with the experimental data is present near $x = 0.4D$, which indicates the presence of a stagnant circulation near that location. The

y -component of velocity shows an higher overall value. This can indicate that the velocity ratio in the experiments was lower in the inclined case than in the perfect configuration. Unfortunately no measurements were conducted within the jet feeding duct in the inclined configuration to confirm these assumptions. The flow upstream of the slot above the plate (see figure 5.2) is in good agreement with the experiments. The downstream field deviates significantly. The outer flow is accelerated more in the numerical predictions than in the experiments. This can be explained by the height of the computational domain, which is smaller than in the water channel. The length of the circulation zone downstream of the slot is $4D$ in the predictions and was $1.8D$ in the experiments. This explains the adverse velocity above the downstream wall.

It can be concluded that the numerical predictions of time-averaged data are in good agreement with the experimental data in the perfect case and less in the inclined case. The instantaneous data differs significantly in the first shear layer, which was unsteady in the experiments and steady in the computations. A development of a lee vortical structure was present in both cases but it is dissipated along its advective path in the experiments, where it forms a stable vortical structure in the computations.

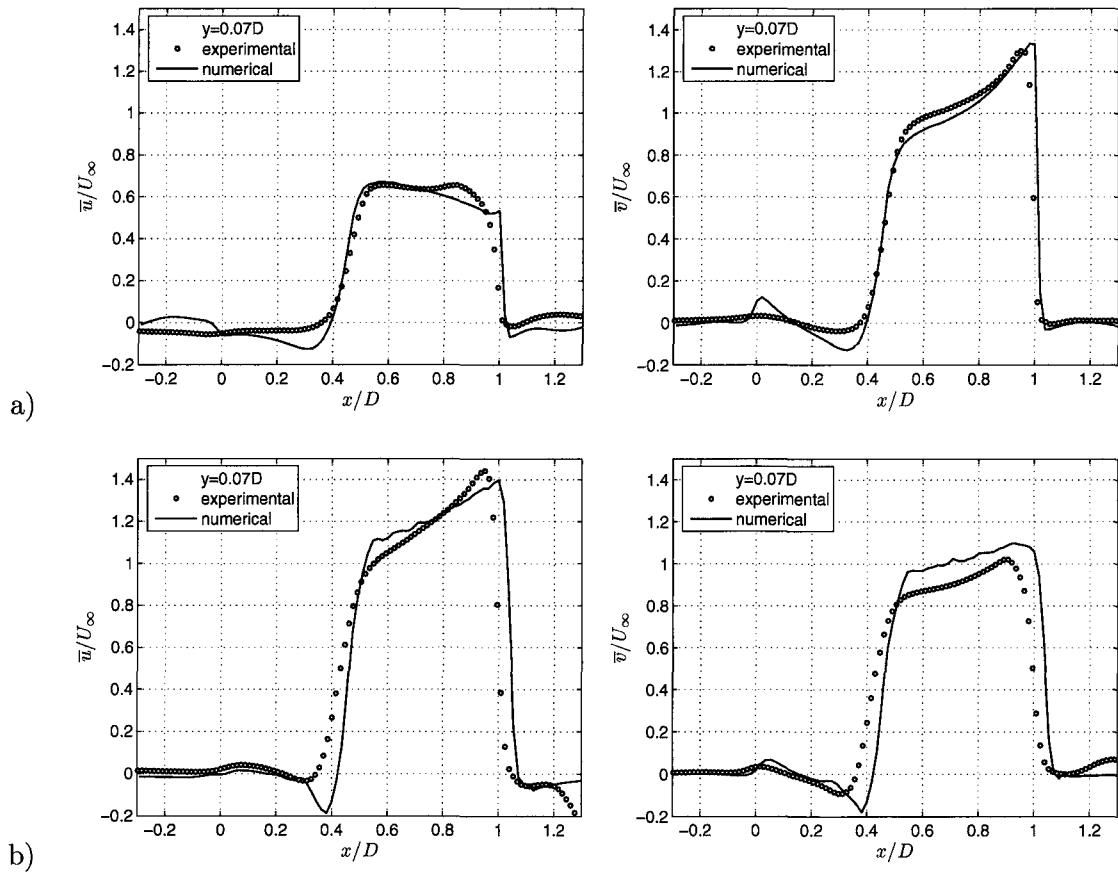


Figure 5.1: Numerical and experimental time-averaged profiles near the exit of the slot, left column x -component and right column y -component a) perfect configuration and b) inclined configuration. A good overall agreement is predicted. The largest deviations are present near the leading edge of the slot. This region consists of a stagnant bubble in the numerical predictions.

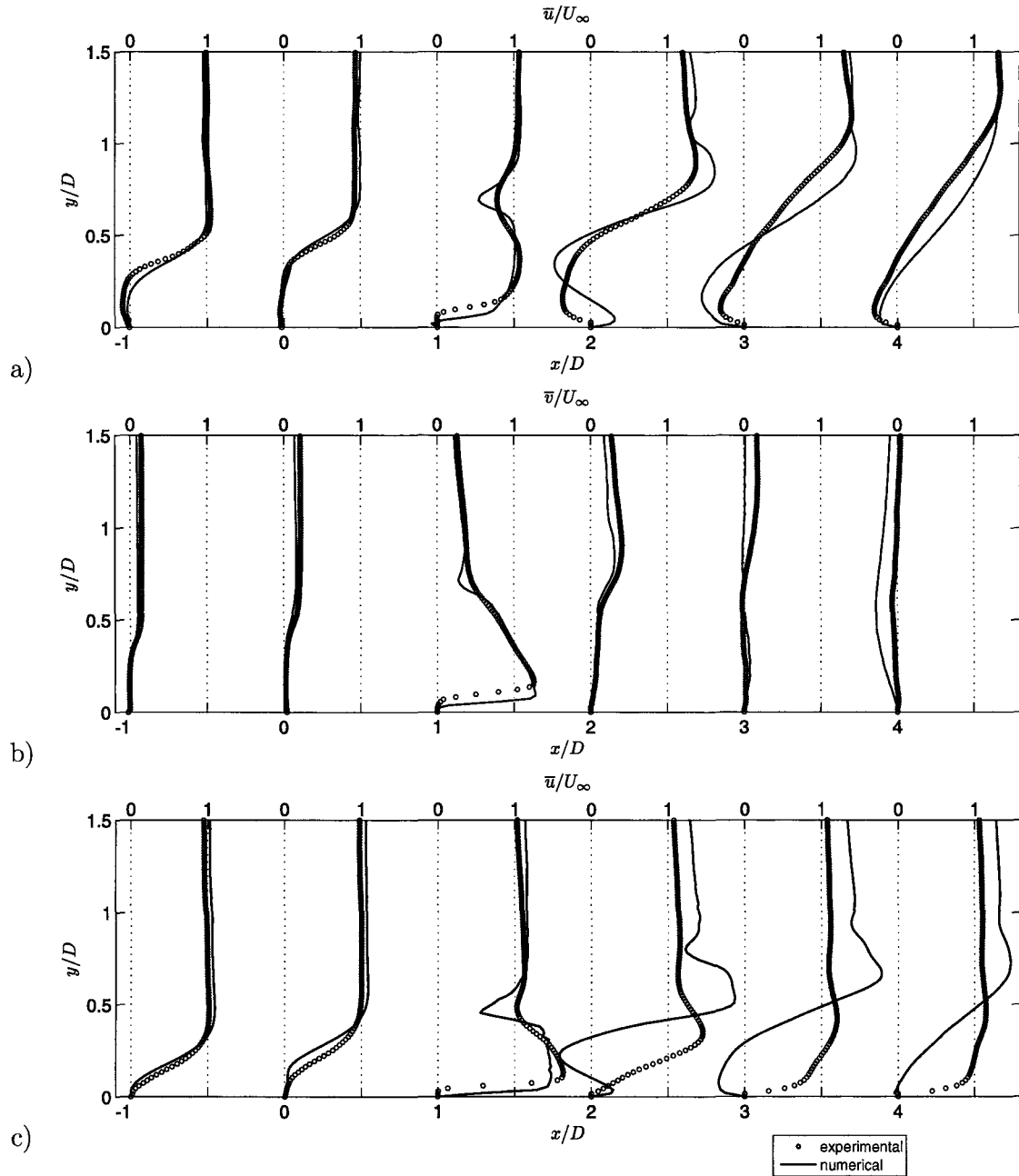


Figure 5.2: Numerical and experimental time-averaged velocity distributions at different x -positions a) axial and b) normal to the wall in the perfect configuration. c) axial to the wall in the inclined configuration.

5.2 Slot jet injection with round jet injection

This section describes a brief comparison between jet injection into a cross-flow through a slot and through a round hole. Jovanović [12] measured a flow field induced by a jet injected through a 37° inclined round tube characterized by $VR = 0.9$, $Re_x = 2.8 \cdot 10^5$ and $Re_d = 1 \cdot 10^4$.

(d represents the diameter of the tube $d = 57mm$) by means of particle image velocimetry. A Reynolds decomposed velocity field along the symmetry line of the hole ($z = 0$) is depicted in figure 5.3. The same figure shows fluctuation velocities obtained in the inclined configuration discussed in chapter 3. Notice that the x and y -axis are normalized by the diameter of the tube in figure 5.3 a) and by the width of the slot in b).

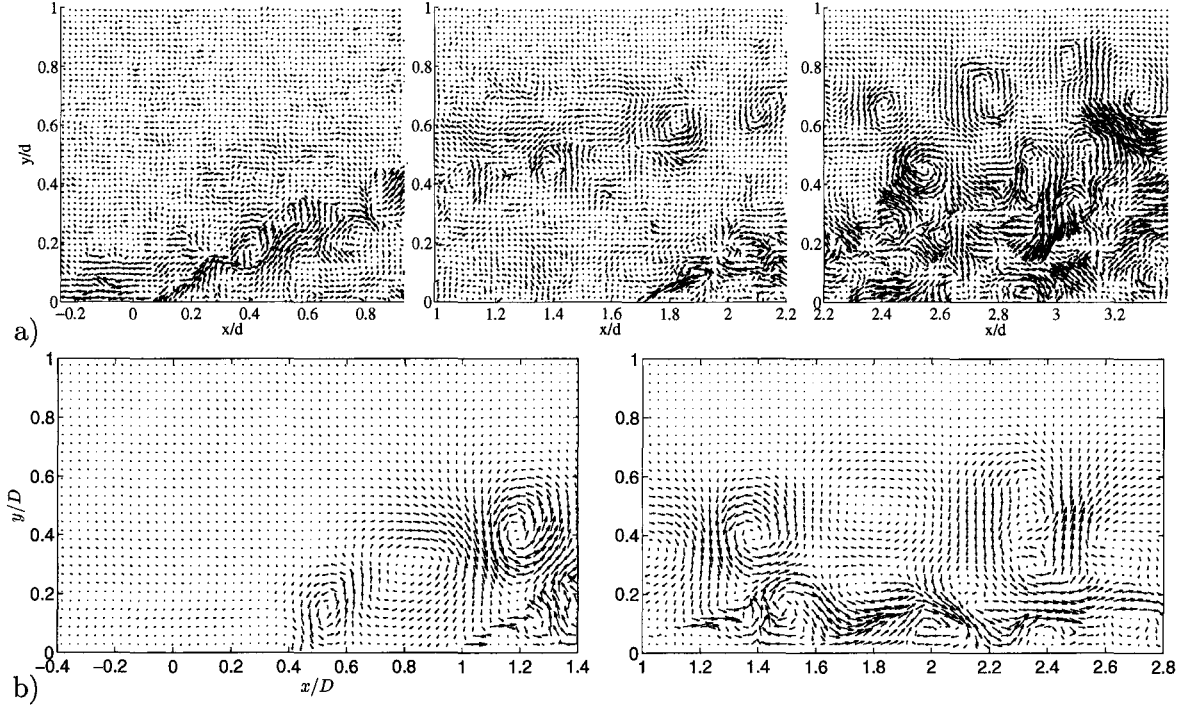


Figure 5.3: Instantaneous flow field obtained by Reynolds decomposition at $z = 0$ obtained by a) round jet injection under an angle of 37° ($VR = 0.9$), the development of positive vortical structures can be seen at the windward side while negative vortical structures are generated at the trailing edge of the hole and they are advected and lifted downstream (see [12]), b) inclined slot jet injection (see chapter 3), positive structures are present at the windward side and negative structures are produced at the trailing edge of the slot and they are advected and stay close to the plate ($VR = 0.75$).

Positive structures are detected along the windward shear layer in both cases. The distance between successive windward structures is smaller in the hole case. The shedding frequency of windward structures was dominant at $f_{vor} = 6.5Hz$ in the hole configuration and at $f_{vor} = 2.5Hz$ in the slot configuration. The size of the windward structures is smaller in the hole configuration. The windward structures developed in the hole configuration deflect in y -direction. They travel parallel to the plate in the slot configuration. Negative lee structures are developed in both cases. The lee structures in the hole case are lifted in y -direction. The lee structure in the slot configuration remains close to the wall. It seems that the windward and lee structure in the hole configuration lift together. All three windward structures in the downstream field have a lee structure close to them. The windward structure advects over the lee structure in the slot configuration. A chaotic field downstream of the trailing edge, above the plate, covers a larger area in the hole case.

5.3 Discussion

It was concluded that the numerical predicted instantaneous velocity fields are significantly different compared to the experimental data. An explanation for the difference in instantaneous flow fields can be found in the three-dimensional character of the experimental flow. The third velocity component w has an essential influence on the flow field. Its influence can be explained by the vorticity equation (see [20]):

$$\frac{\partial \underline{\omega}}{\partial t} + (\underline{v} \cdot \nabla) \underline{\omega} = (\underline{\omega} \cdot \nabla) \underline{v} + \nu \nabla^2 \underline{\omega}, \quad (5.1)$$

in which $\underline{\omega}$ is the vorticity distribution $\underline{\omega} = (\omega_x, \omega_y, \omega_z)$. This equation can be normalized:

$$\tilde{\omega} = \frac{L\omega}{V}, \quad \tilde{t} = \frac{Vt}{L}, \quad \tilde{v} = \frac{v}{V}, \quad \tilde{\nabla} = \nabla L, \quad \tilde{\nabla}^2 = \nabla^2 L^2,$$

where L and V represent a length and a velocity respectively. Equation 5.1 becomes

$$\frac{\partial \tilde{\omega}}{\partial \tilde{t}} + (\tilde{v} \cdot \tilde{\nabla}) \tilde{\omega} = (\tilde{\omega} \cdot \tilde{\nabla}) \tilde{v} + \frac{1}{Re} \tilde{\nabla}^2 \tilde{\omega}, \quad (5.2)$$

where $Re = \frac{VL}{\nu}$. In the present study L can for example be the width of the slot or the length of the flat plate. V can be a local velocity. In a two-dimensional situation $\frac{\partial}{\partial z} = 0$ and $w = 0$, which holds that $\omega_x = 0$ and $\omega_y = 0$ and therefore equation 5.2 becomes

$$\frac{\partial \tilde{\omega}_z}{\partial \tilde{t}} + (\tilde{v} \cdot \tilde{\nabla}) \tilde{\omega}_z = \frac{1}{Re} \tilde{\nabla}^2 \tilde{\omega}_z. \quad (5.3)$$

This means that the first term on the right-hand side of equation 5.2 is zero due to the absence of w . Nieuwstadt [20] proposed a hypotheses in three-dimensional turbulence which takes this term into account as a relevant element in the energy cascade from macro structures to micro structures. This term describes stretching and tilting of a vortex tube. He interpreted this mechanism in a way that large eddies deform small eddies and thereby handing over their energy to the smaller eddies. This mechanism results in an increased vorticity of the smaller eddies because their circulation remains similar. The smaller eddies are deformed to sizes which fit the microstructure and vorticity will be dissipated under influence of friction produced by viscosity. Thus, by forcing the w -component to be zero, as in the numerical computations, an important mechanism that leads to dissipation of vorticity is excluded, if this hypothesis is valid.

The term on the right-hand side in equation 5.4 describes diffusion of vorticity due to viscosity. Which states that it becomes of significant influence when the Reynolds number is small. In the present situation the Reynolds number is small near boundaries where the no-slip condition holds. In the central part of the flow $Re \gg 1$ and therefore, equation 5.4 becomes

$$\frac{\partial \tilde{\omega}_z}{\partial \tilde{t}} + (\tilde{v} \cdot \tilde{\nabla}) \tilde{\omega}_z = 0 \quad (5.4)$$

which means that vorticity generated in the boundary layers will not be diffused and can only be transported in time. This analysis explains that vortical structures, which originate near the lee side of the jet, do not dissipate in a two-dimensional situation. This was the case in the experiments.

The first shear layer was shed by positive and negative vortical structures in the experiments. The main computations did not predict shedding of vortical structures along the first shear layer. They determined a stagnant negative vortical structure near the leading edge. It is interesting that the start up process of the calculations was unsteady in such a way that vortical structures were formed along the first shear layer. Also the unsteady behavior of a corner vortical structure was seen. This indicates that development of a vortical structure in that area does not have to be the result of a three-dimensional motion. The development can than be the result of velocity perturbations which initially are large in the computations and during time become less and finally go to zero. Perturbations in the velocity are probably present in the experimental set-up which can trigger an instability and subsequently form the vortical structure.

Preliminary computations described in chapter 2 show some similarities with the computations described in this chapter. The velocity distribution near the exit of the slot shows a concave shape and a maximum velocity near the trailing edge of the slot in both cases. A stagnant negative leading edge vortical structure was present. The mean flow indicates circulation downstream of the slot in both cases. Also the advection of vortical structures downstream of the slot was detected along the instantaneous fields, although the average shedding frequency was $1Hz$ instead of $5Hz$, which can be the result of the velocity ratio. Bearing in mind that predictions of the mean flow in the perfect configuration are relatively good, it can be expected that the mean flow in the first computations is also well predicted. This means that a first screening of slot-geometries in a two-dimensional numerical approach can give a reliable insight in some flow features. It should be noticed that the sample amount N of velocity fields in the first computations was 90 which was 1005 in the latter numerical predictions. This difference can have an effect on the statistical downstream data. In an engine application perturbations and three-dimensional effects can not be neglected which means that one should thoroughly test a numerical chosen geometry experimentally before implementation.

Comparison between experimental jet injection through a round hole and a slot pointed out that windward shedding of a positive structure and lee shedding of a negative structure appears in both cases. The formation of a lee structure is probably the result of jet separation near the trailing edge in both configurations. The windward shedding can be different. A jet supply through a tube is influenced by the lid-effect which creates a low local jet velocity near the leading edge of the hole. The local jet velocity near the lower side of the flat plate inside the slot is high due to blockage of the co-flow by the end wall of the slot. This probably affects the generation of vortical structures at the windward side of the jet.

Chapter 6

Conclusions and recommendations

Conclusions

The influence of geometry variations on the flow field, which is generated by the slot-jet injection into a cross-flow, was numerically and experimentally studied.

The time-dependent flow induced by an isothermal slot-jet injection into a cross-flow was simulated numerically with five different perpendicular feedings ($VR = 0.25$, $Re_x = 2 \cdot 10^5$, $Re_D = 3.7 \cdot 10^3$). The Comsol package was applied to conduct these numerical experiments. The interaction between the steady upstream cross-flow and ejected jet produces a steady windward shear layer, stagnant leading edge circulation and unsteady lee shear layer. The jet cross-flow interaction induces a downstream shedding of negative vortical structures which appear as a ‘re-circulation’ zone in time-averaged flow field. The influence of a jet inlet velocity distribution to the flow field is negligible but an imperfection inside the slot produces an additional ‘circulation’ zone near the leading edge of the slot. The shape of an imperfection has minor influence to the flow field. An imperfection does not significantly influence the downstream flow field.

Velocity fields induced by three different co-flow slot configurations (see figure 3.3) of a jet ejection into a cross-flow were measured by means of particle image velocimetry ($VR = 0.75$, $Re_x = 1.3 \cdot 10^5$, $Re_D = 3.8 \cdot 10^3$). The geometry and flow conditions were different from the preliminary computations due to set-up limitations. The flow was unsteady and three-dimensional. The mean flow is characterized by the following regions: negative circulation in the corner of the slot, lifted cross-flow boundary layer, negative circulation upstream of the jet, first shear layer at the windward side of the jet, second shear layer at the jet lee side and downstream circulation. In the instantaneous flow fields, positive and negative vortical structures are detected along the first shear layer. Only negative vortical structures are measured along the second shear layer. The global similarity of flow features is recognized in all three configurations. A difference between the configurations is the penetration height of the jet into the cross-flow. A slot imperfection reduces the penetration height by 50% while a feeding side inclination decreases the penetration height by 68%. The time-averaged ‘re-circulation’ detected in the mean flow field is the smallest in the inclined configuration. The highest shedding frequency of vortical structures along the first and second shear layer and the strongest vortical structures are detected in the case of the inclined slot.

A very similar two-dimensional time-dependent flow was also simulated by means of Comsol. The simulation reveals a steady flow inside the slot, upstream of the slot and above the slot. The downstream flow field is unsteady due to downstream shedding of negative vor-

tical structures. Time-averaged flow characteristics correspond relatively good to the mean experimental data. The instantaneous flow field does not coincide with the experiments. Three-dimensional effects have a significant influence on the flow and they can not be neglected.

Recommendations

The current design of the jet feeding duct in the experimental set-up has probably a significant influence on the formation of flow structures. The experimental set-up should be redesigned to study the specific processes that are hypothesized to most likely alter flow structures at the windward side.

Three-dimensional effects can not be neglected in slot jet flows. Numerical modeling of three-dimensional slot jet flows should therefore be conducted in order to provide a physics-based interpretation of flow structures. In addition, computations with implementation of the energy equation should be conducted in order to quantify the effect of flow characteristics to a film cooling effectiveness.

Bibliography

- [1] Adrian, R., Christensen, K., Liu, Z., 2000, Analysis and interpretation of instantaneous turbulent velocity fields, *Experiments in Fluids*, vol 29, pp. 275-290.
- [2] Aly, S.E., 2000, Injection effect on two dimensional boundary layer, *Energy Conversion & Management*, vol 41, pp. 539-550.
- [3] Andreopoulos, J., 1982, Measurements on a pipe flow issuing perpendicular into a cross stream, *ASME J. Fluids Eng.*, vol. 104, pp. 493-499.
- [4] Bastiaans, R.J.M., 2000, Cross-correlation PIV: theory, implementation and accuracy, Technische Universiteit Eindhoven.
- [5] Beckwith, T.G., Marangoni, R.D., Lienhard V, J.H., 1995, *Mechanical measurements*, United States of America.
- [6] Bunker, R.S., 2005, A review of shaped hole turbine film cooling technology, *Journal of Heat Transfer*, vol. 127, pp. 441-453.
- [7] Graftieaux, L., Michard, M., Grosjean, N., 2001, Combining PIV, POD and vortex identification algorithms for the study of unsteady turbulent swirling flows, *Meas. Sci. Technol.*, vol 11, pp. 1422 -1429.
- [8] Cremers, M.F.G., 2001, Het ontwerp van een 3D-PIV opstelling voor bypass transitie, Master's Thesis, Technische Universiteit Eindhoven.
- [9] Fitt, A.D., Ockendon, J.R., Jones, T.V., 1985, Aerodynamics of slot-film cooling: theory and experiment, *J. Fluid Mech*, vol. 160, pp. 15-27.
- [10] Heijst, G.J.F. van, 1992, *Voortgezette stromingsleer 1*, Technische Universiteit Eindhoven.
- [11] Hyams, D.G., McGovern, K.T. and Leylek, J.H., 1996, Effects of Geometry on slot jet Film Cooling Performance, *ASME 96-GT-187*.
- [12] Jovanović, M.B., 2006, *Film Cooling Through Imperfect Holes*, PhD thesis, Printed at Technische Universiteit Eindhoven, ISBN-10:90-386-2888-9 and ISBN-13: 978-90-386-2888-2.
- [13] Jovanović, M.B., de Lange, H.C. and Steenhoven, A.A. van, 2006, Influence of hole imperfection on jet cross-flow interaction, vol. 27, pp. 42-53.

- [14] Glezer, B. 2003, Handbook of Turbomachinery: Second Edition, chapter 8. ISBN: 0-8247-0995-0.
- [15] Kassimatis, P.G., Bergeles, G.C., Jones, T.V. and Chewc, J.W., 2000, Numerical investigation of the aerodynamics of the near-slot film cooling, *Int. J. Numer. Meth. Fluids*, vol. 32, pp. 97-117.
- [16] Maassen, S.R., Clercx, H.J.H. and Heijst, G.J.F. van, 2002, Self-organization of quasi-two-dimensional turbulence in stratified fluids in square and circular containers, *physics of fluids*, vol. 14, nr. 7.
- [17] Miron, P. and Léger, B., 2005, A numerical and experimental investigation of the slot film-cooling jet with various angles, *Journal of Turbomachinery*, vol. 127, Nr. 3, pp. 635-645
- [18] Moerkerken, A., 2002, Experiments on flow field variations due to productions inaccuracies of a film cooling nozzle, Master's Thesis, Technische Universiteit Eindhoven.
- [19] Najjar, F.M., and Balachandar, S., 1998, Low-frequency unsteadiness in the wake of a normal flat plate, *J. Fluid Mech.*, vol. 370, pp. 101-147.
- [20] Nieuwstadt, F.T.M., 1998, *Inleiding in de theorie en toepassingen van turbulente stromingen*, Epsilon Uitgaven, Utrecht.
- [21] Orlandi, P., Carnevale, G.F., Lele, S.K. and Sharik, K., 1998, DNS study of stability of trailing vortices, Center for Turbulence Research, Proceedings of the Summer Program.
- [22] Peterson, S.D. and Plesniak, M.W., 2004, Evolution of jets emanating from short holes into crossflow, *Exp. Fluids*, vol 33, pp. 889-898.
- [23] Sarkar, S. and Bose, T.K., 1995, Numerical simulation of a 2-D jet-crossflow interaction related to film cooling applications: Effects of blowing rate, injection angle and free-stream turbulence, *Sādhanā*, vol 20, part 6, pp. 915-395.
- [24] Schlichting, H. and Gersten, K., 2000, *Boundary Layer Theory*, Springer, Berlin.
- [25] Schreel, K.R.A.M. and Steenhoven, A.A. van, 2002, *Fysische Meetmethoden versie 4*, Technische Universiteit Eindhoven.
- [26] Shannon, D.W., Morris, C.S., 2004, Visualization of blunt trailing edge turbulence, 11th International Symposium on Flow Visualization, University of Notre Dame, August 9-12.
- [27] Vosse, F.N. van de, 1987, Numerical analysis of carotid artery flow. PhD thesis, Eindhoven University of Technology, The Netherlands.
- [28] Volmers, H., 2001, Detection of vortices and quantitative evaluation of their main parameters from experimental velocity data, *Meas. Sci. Technol.*, vol 12, pp. 1199-1207.
- [29] Yao, Y.F., Thomas, T.G., Sandham, N.D., Williams, J.J.R., 2001, Direct numerical simulation of turbulent flow over a rectangular trailing edge. *Theoretical and computational fluid dynamics*, vol. 14(5), pp. 337-358.

Appendix A

Identification of vortical structures

A number of algorithms are suggested in literature to identify vortical structures within a two-dimensional flow field. Three of these algorithms were applied on an arbitrary flow field obtained from PIV measurements (see figure A.1). The first algorithm is based on identifying regions of significant vorticity ($\omega_z = \frac{\partial v}{\partial x} - \frac{\partial u}{\partial y}$) (see [1]). The vorticity field shows regions with positive vorticity along the first shear layer and negative in the lifted cross-flow boundary layer and along the second shear layer (figure A.1). A few regions with relatively high vorticity are present in the first shear layer. The vorticity detects the core of a vortical structures and secondly shear in the velocity field. This makes it extremely difficult to use vorticity maps to identify vortical structures.

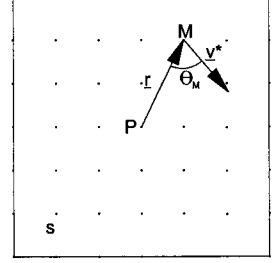
The second identification algorithm has been proposed by Adrian et al. [1] and Vollmers [28]. They stated that the local velocity gradient tensor, of a two-dimensional flow field, will either have two real eigenvalues or a pair of complex conjugate eigenvalues λ . They proposed that the strength of any local swirling motion is quantified by the imaginary part of the eigenvalue λ_{im} , therefore is λ_{im} defined as the swirling strength. Plotting iso-regions of $\lambda_{im} > 0$ leads to the identification of vortical structures, see figure A.1. A relatively large structure is present in the beginning of the first shear layer. Further downstream along this layer, more smaller ones have been identified. The second shear layer consists of three structures. A drawback of this method is that the sense of rotation is unknown, which requires an additional operation, for example plotting vectors in the reference frame of the structure. The threshold of λ_{im} can be varied in order to locate strong or weak cores.

The third method was proposed by Graftieaux et al. [7] and named here as the Γ_1 -method. They developed a function Γ_1 that makes it possible to characterize the location of a vortical structure, by considering only the velocity field, without the use of derivatives. The function Γ_1 at location P is defined as

$$\Gamma_1(P) = \frac{1}{N} \sum_s \frac{\underline{r} \times \underline{v}^* \cdot \underline{z}}{||\underline{r}|| \cdot ||\underline{v}^*||} = \frac{1}{N} \sum_s \sin(\theta_M), \quad (\text{A.1})$$

where s is a domain of fixed size, centered on P , M is a location in s , N is the amount of points M inside s and \underline{z} is the unit vector normal to the xy -plane. \underline{r} is a space vector, $\underline{v}^* = \underline{v}_M - \langle \underline{v}_P \rangle$ with \underline{v}_M the velocity vector at location M and $\langle \underline{v}_P \rangle$ the local space averaged velocity vector defined by

$$\langle \underline{v}_P \rangle = \frac{1}{N} \sum_s \underline{v}_M.$$



The angle between \underline{r} and \underline{v}^* is represented by θ_M . In the situation that $|\Gamma_1(P)| = 1$, point P is the center of an axisymmetric vortical structure. The sign of Γ_1 indicates the direction of rotation of the vortical structure. The number of points N within s has been chosen as $N = 169$ in this study. Graftieaux et al. [7] considered that a flow is locally dominated by rotation if $|\Gamma_1(t)| > \frac{2}{\pi}$. Contour lines of $|\Gamma_1| > \frac{2}{\pi}$ are shown in figure A.1. The filled regions indicate a structure with negative rotation and the black closed lines indicate positive rotation. This method also identifies a structure at $(0.7, 0.6)$ and near $(0.5, 0.2)$. Downstream of the first shear layer three positive structures are shown. The second shear layer consists of an elongated structure and a smaller one.

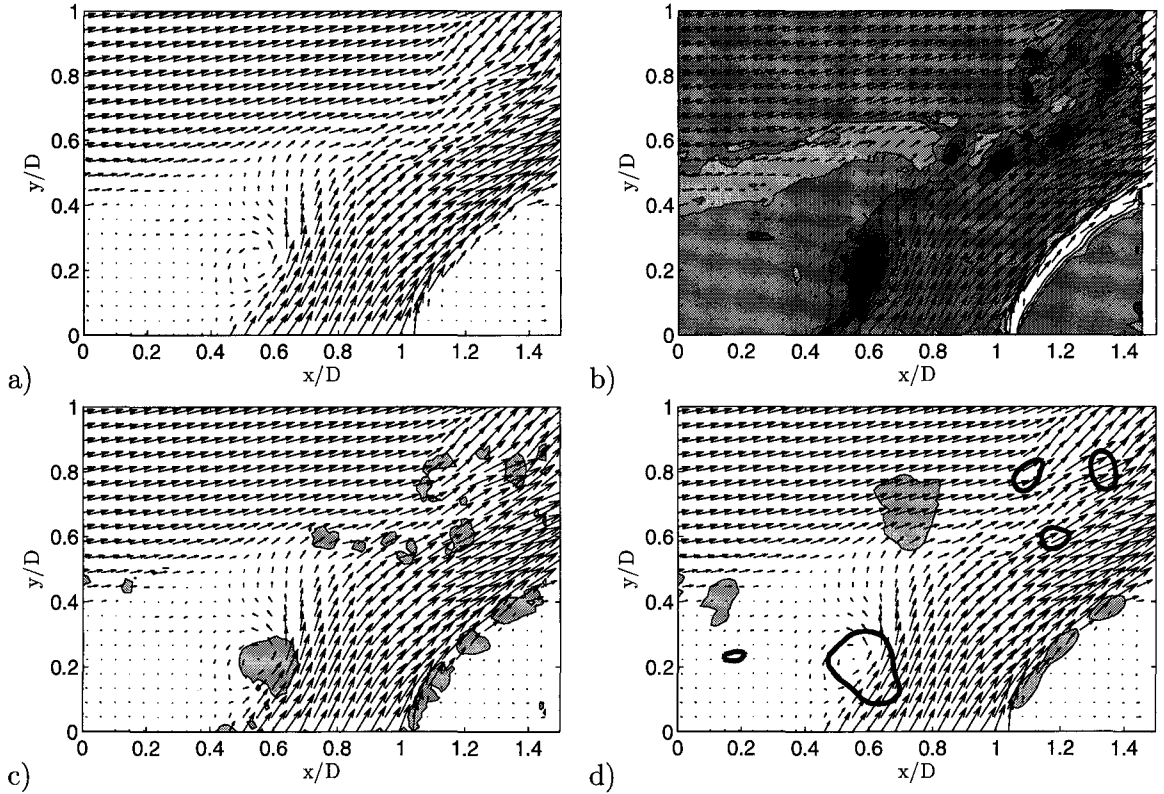


Figure A.1: Vortical structure identification algorithms. a) The test case, instantaneous velocity field above the perfect slot, b) vorticity (ω_z) (a dark color indicates positive vorticity and light color negative), c) swirling strength (λ_{im}) and d) Γ_1 -method, a filled region indicates negative rotation and a thick black line is positive.

The detected vortical structures are the less noisy in the case of the Γ_1 -method. It has the advantage to immediately determine the sense of rotation and derivatives do not have to be calculated. Computing derivatives of a velocity field obtained by PIV-measurements can be inaccurate, especially in regions with high shear. With this method, reliable vortical structures statistics can be obtained. Therefore it is decided to analyse the instantaneous data with the Γ_1 -method. Figure A.2 is depicted to illustrate center points of the detected structures.

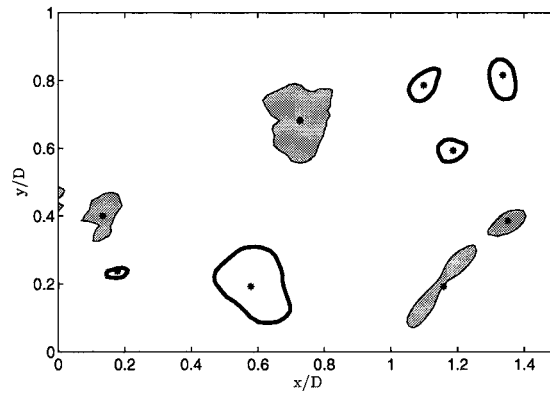


Figure A.2: Center points of vortical structures detected by the Γ_1 -method.

In order to illustrate the impact of the Γ_1 -method on the PIV measurements, figure A.3 is displayed. This figure shows instantaneous \underline{v} and fluctuating \underline{v}' vectors, obtained above and downstream of the slot, in the inclined configuration. In the background contour plots of $|\Gamma_1(t)| > \frac{2}{\pi}$ are drawn. A dashed line indicate positive rotation, a closed line indicates negative. Islands enclosed with the contour line $|\Gamma_1(t)| = \frac{2}{\pi}$ are denoted as vortical structures. A variety of vortical structures is detected by the Γ_1 -method. Some are small in size, some have a relatively large size. Values of $|\Gamma_1|$ ranges from 0.65 till 0.95. It is interesting to see that the structures 'wvn2' and 'wvp3' in figure A.3 have been detected by the Γ_1 -method, where they are not identified by viewing the instantaneous velocity field. The fluctuating field shows the core for 'wvp3' very well but this is not the case for 'wvn2'. This structure has its center near $y = 0.35D$, which is according to the fluctuating velocity expected at $y = 0.2D$. This is explicitly noticed to make a reader aware of the fact that identifying vortical structures by only viewing the fluctuating field may give an other interpretation of flow. Vortical structures detected by the Γ_1 -method are often hidden in the instantaneous flow, which is for example the case regarding 'wvn2'. This is nicely illustrated in figure A.4 where first \underline{v} within 'wvn2' is shown and secondly $\hat{\underline{v}}$. A typical vortical structure is obtained by $\hat{\underline{v}}$.

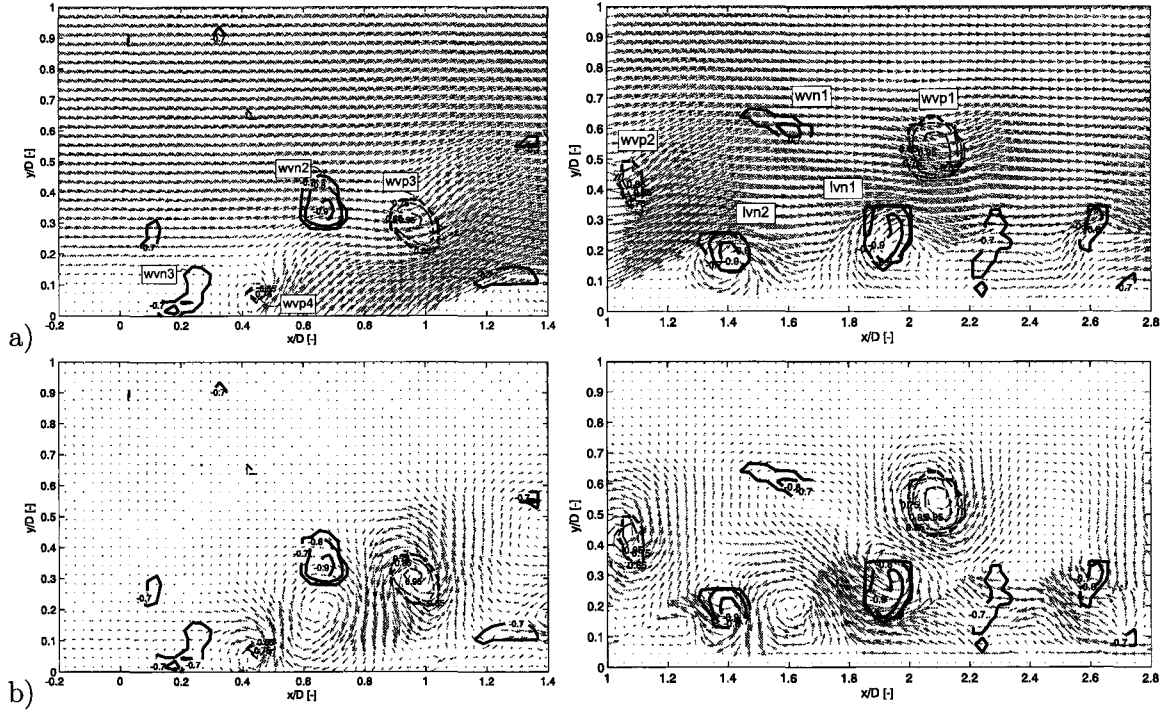


Figure A.3: Vortical structures detected by the Γ_1 -method in the inclined case at an arbitrary time step with a) the instantaneous velocity field \underline{u} and b) velocity fluctuations \underline{u}' . Positively numbered and closed contour lines indicate locally dominated flow with a positive rotation.

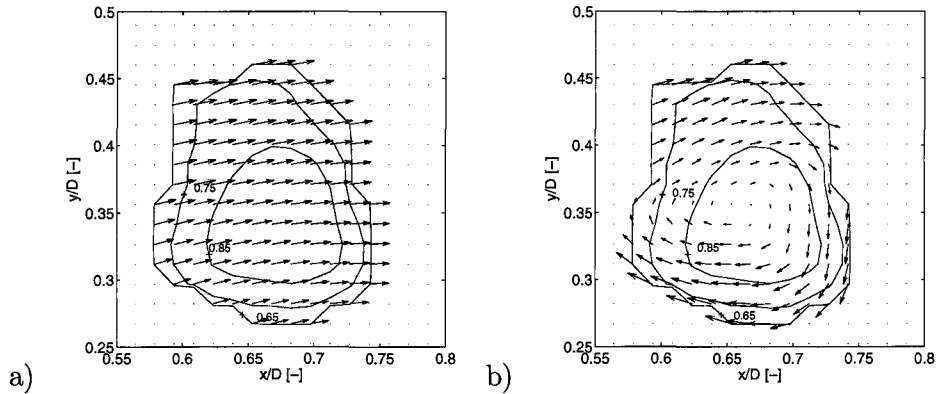


Figure A.4: Vortical structure 'wvn2' detected by the Γ_1 -method with a) \underline{u} and b) \underline{u}' vectors.

In order to enlighten the shape and position of the detected vortical structures in the instantaneous velocity fields, an example of eight successive times is depicted here. These structures were detected in the inclined configuration. Figure A.5 shows them above the slot and figure A.6 downstream of the slot. Figure A.5 shows nicely the development of 'wvn' and 'wvp' near the leading edge of the slot and their advection along the first shear layer. Windward structures are still present in the downstream field. 'wvn' was dissipated along its path. The presence of a lee vortical structure 'lvn' is also indicate in figure A.6. 'wvp' travels over an lee structure and keeps its shape.

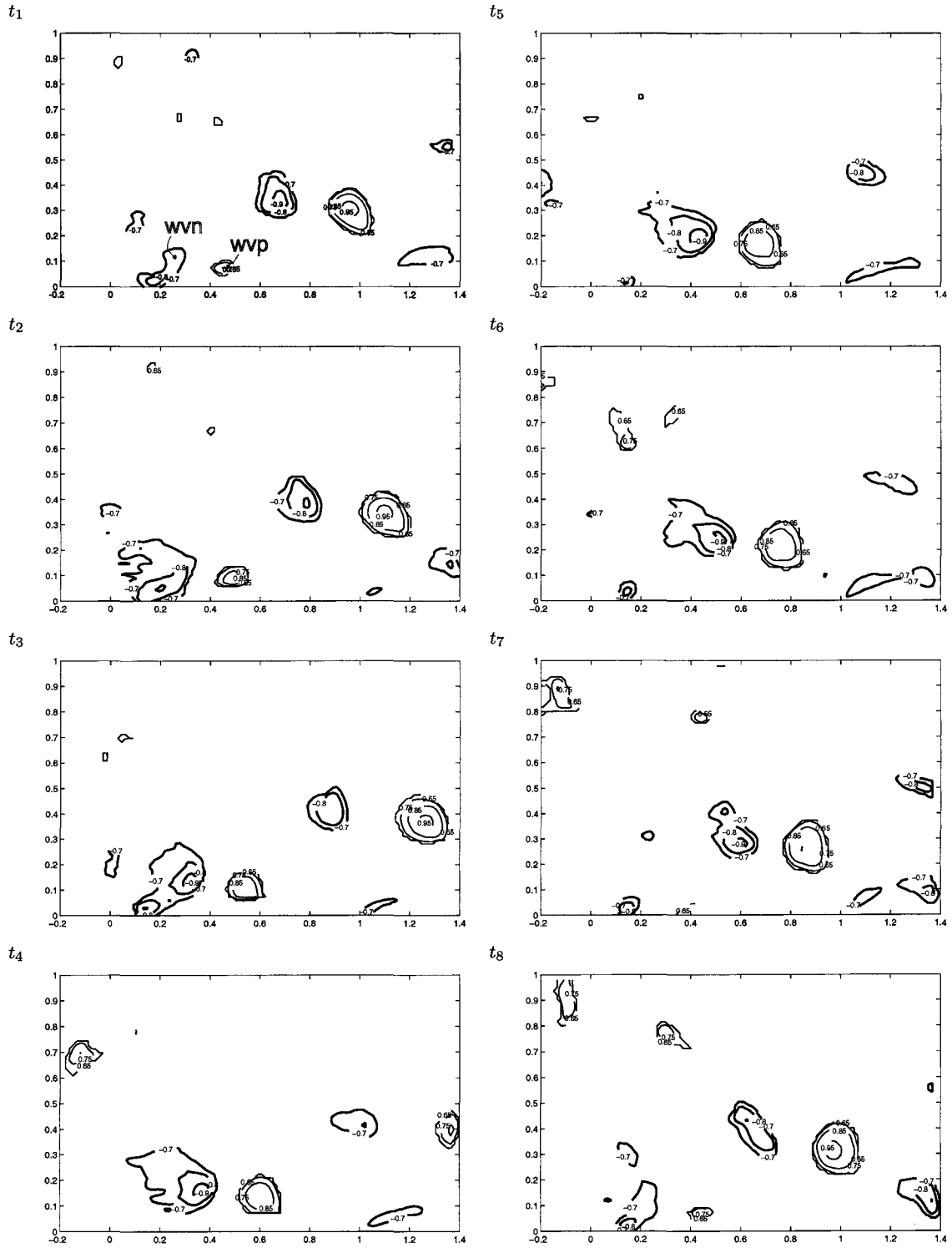


Figure A.5: Contour plots of $|\Gamma_1(t)| > \frac{2}{\pi}$ in the inclined configuration for eight successive times indicated by t_j , $j = 1, 2, \dots, 8$ and $\Delta t = \frac{1}{14.8} s$. Figures have been obtained above the slot with the leading edge of the slot located at $(0, 0)$. x -axis and y -axis are normalized positions.

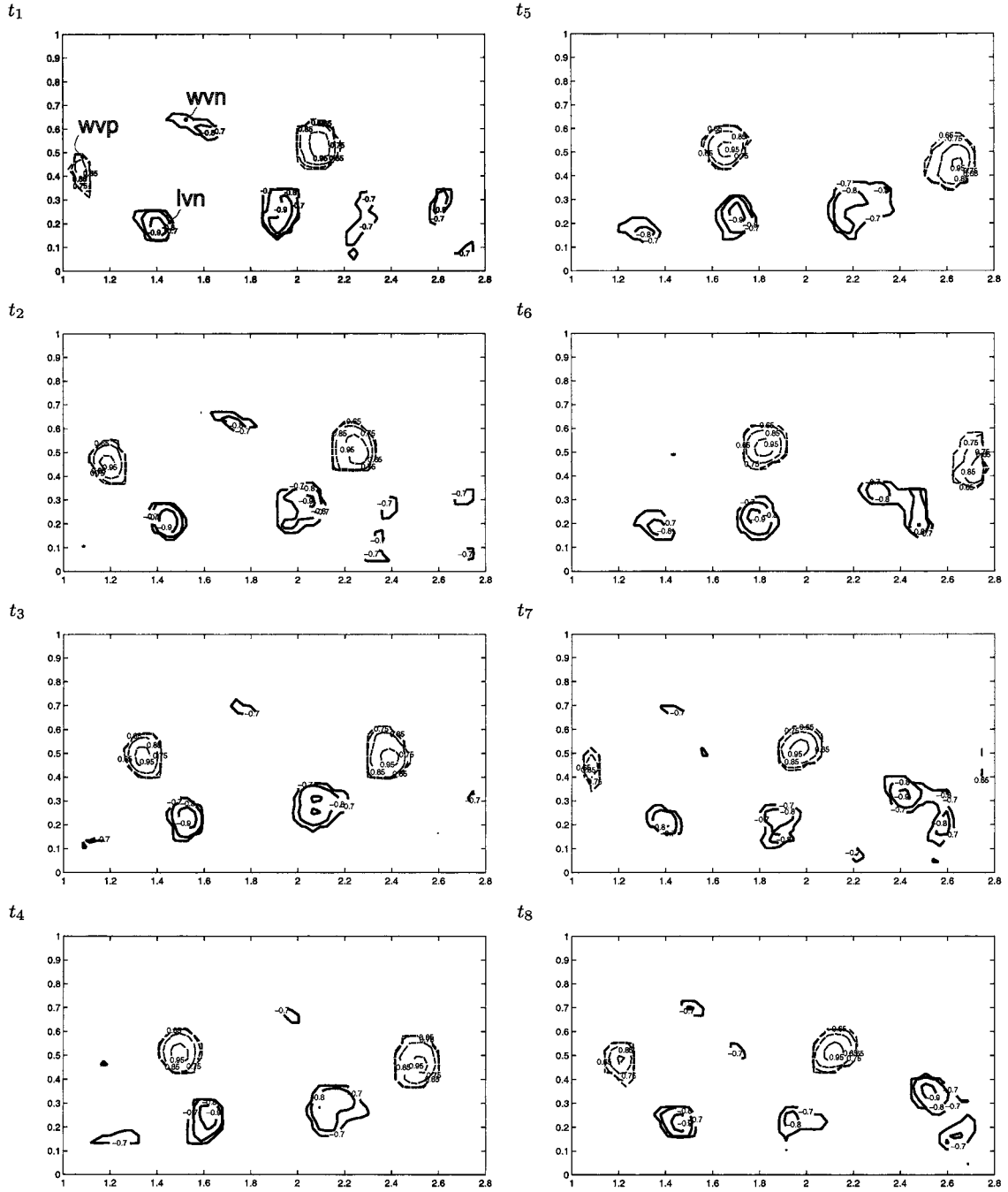


Figure A.6: Contour plots of $|\Gamma_1(t)| > \frac{2}{\pi}$ in the inclined configuration for eight successive times indicated by t_j , $j = 1, 2, \dots, 8$ and $\Delta t = \frac{1}{14.8} s$. Figures have been obtained downstream the slot. The trailing edge of the slot is located at $(1, 0)$. x -axis and y -axis are normalized positions.

Appendix B

Statistical analysis of vortical structures

Section 3.6 describes the need to a statistical approach in the analysis of the developed vortices. Quantitative comparison has been performed between the vortical structures in the different configurations. Figure 3.20 illustrates histograms of surfaces. The most interesting histograms regarding the other quantities are depicted in figures B.1 till B.2. A detailed analysis is described here and a summary is given in section 3.6.

Along the first shear layer

Advection velocities of the positive windward and negative windward structure are similar in all three control windows. Advection velocity in window A is the lowest in the perfect configuration where a maximum $\varsigma = 42\%$ at $U_{vor} = 0.9$, followed by the imperfect case where $\varsigma = 52\%$ at $U_{vor} = 1$. U_{vor} is the highest in the inclined case at $U_{vor} = 1.2$ where $\varsigma = 62\%$. All three distributions are pyramidical. At window B the distributions are shifted towards a higher U_{vor} . Most structures travel here with $U_{vor} = 1.2$ in the perfect case and in the imperfect and inclined case $U_{vor} = 1.3$. At position C, vortical structures in the inclined configuration are decelerated to $U_{vor} = 1.2$ where in the imperfect configuration a similar distribution as previous is present, although, a small amount of increasing velocities for positive structures. The structures originating in the perfect case are accelerated to $U_{vor} = 1.3$.

The largest detected structure, in window A, is generated in the perfect configuration with the maximum size of $s_{vor} = 0.09$. The largest size in the imperfect configuration, detected in window A is $s_{vor} = 0.08$ ('wvn') and in the inclined configuration $s_{vor} = 0.05$ ('wvn' and 'wvp'). Most structures in window A have a size $0.02 < s_{vor} < 0.03$ in all three configurations. Further downstream in window B and C, the distribution of the structures in the inclined configuration remains approximately similar concerning the positive structure. The positive structure becomes smaller in the perfect and imperfect configuration. In all three configurations a decaying distribution is present for the negative structure. Although a small amount of structures is large going to $s_{vor} = 0.08$.

A huge difference in circulation Γ is detected between the positive and negative structures. The circulation of negative structure are discussed now. A maximum $|\Gamma|$ in window A is 0.25, obtained in the perfect configuration. A maximum $|\Gamma|$ for the imperfect case is 0.2 and for the inclined 0.1. The bandwidth is small with a peak at $|\Gamma| = 0.05$ in all three configurations.

ς increases at $|\Gamma| = 0.05$ further downstream in the imperfect and inclined configuration, resulting in negative structures with low strength in the far field. $|\Gamma|$ in the perfect case decreases slightly. The circulation of the positive structure, concerning window A, is 0.65 in the perfect configuration. The smallest strength is 0.05, also in the perfect configuration. The most structures of all three configurations are detected with $0.1 < \Gamma < 0.4$. The histogram of Γ in window A shows a pyramid distribution in the imperfect and inclined configuration, where the peak is at $\Gamma = 0.3$ in both cases. The perfect case distribution does not show a clear shape which changes in window B. Here is a decaying distribution within the range from the maximum at $\Gamma = 0.1$ to a minimum of $\Gamma = 0.4$. An opposite distribution is present in the inclined configuration. Here the minimum is detected at $\Gamma = 0.05$ and the maximum at $\Gamma = 0.35$. In general, the strength of the structures educed in the perfect and imperfect configuration, decays along the shear layer. The perfect and imperfect case both show a peak in window C at $\Gamma = 0.1$. In the inclined case Γ also decays but slower. In window C still 13% of the structures has a circulation of 0.35 in the inclined case.

The average vorticity Ω of the negative structure is concentrated in a narrow band at $\Omega = -2$ in all the three configurations. Further downstream in window B and C, significant differences are not detected. Regarding the positive structure, Ω is the smallest in the perfect case near $\Omega = 4$ and the largest in the perfect and inclined configuration around $\Omega = 18$. The inclined and imperfect configuration show a pyramid distribution where a peak at $\Omega = 12$ is detected in both cases. The peak value is present in the perfect case around $\Omega = 8$. In general the average vorticity is the largest in the imperfect and inclined case. Further downstream a decrease in average vorticity is detected in all three the configurations. A large amount of structures in the perfect case have a lower Ω than in window A and B but still the peak is around $\Omega = 8$ in window C. The peak in the inclined case in window C is around $\Omega = 8$ and in the imperfect case near $\Omega = 6$.

Along the second shear layer

A small amount of positive structures is detected in the second shear layer in all three the configurations. They all have a relatively low surface, circulation and average vorticity. Therefore it is decided to evaluate the negative ('lvn') structures only. A wide range of advection velocities is detected in the perfect and imperfect case $0.2 < U_{vor} < 1.5$. The velocities have a bell-shaped distribution in window A. A peak is detected near $U_{vor} = 0.8$ in the perfect case and $U_{vor} = 0.9$ in the imperfect case. The inclined configuration covers a smaller range from 0.8 to 1.2 where 55% of the structures undergo an advection velocity of 1. Further downstream in the inclined configuration, velocities are decreased and cover a wider range going from 0.4 to 1.2, where a peak is detected around $U_{vor} = 0.8$. The perfect and imperfect configuration show a flatter distribution in window E. The amount of structures with low velocities are increased but also the amount of structures with a high velocity are increased.

The largest structure detected in window D ($s_{vor} = 0.09$) is generated in the imperfect configuration. The largest structure in the perfect case is 0.07 and in the inclined configuration 0.05. The perfect and imperfect configuration show a flat distribution from 0.01 to 0.05 in window D. Structures in the inclined configuration have surfaces from $s_{vor} = 0.02$ to $s_{vor} = 0.03$ in window D. In window E, a largest structure ($s_{vor} = 0.16$) is detected in the perfect configuration. The largest structure in the imperfect case is 0.13 and in the inclined case 0.07. Vortical structures in the inclined case have become smaller along its path. At window E, distributions of the perfect and imperfect configuration show a decay. The largest

amount is small but the amount of larger structures is increased somewhat as well.

The structures are generated with a large dispersion in circulation in the three configurations. $|\Gamma|$ varies from 0.1 to 1 in window D. The inclined configuration shows a large amount in a relatively small range $0.5 < |\Gamma| < 0.7$. The perfect and imperfect configuration show a disperser distribution along $0.1 < |\Gamma| < 1$. In the downstream window, a shift is detected in the three configurations towards lower circulations. Although some structures in the perfect case are detected with $|\Gamma| = 1.5$. The largest amount in the imperfect configuration is detected near $0.1 < |\Gamma| < 0.4$ which for the inclined configuration is higher $0.2 < |\Gamma| < 0.6$.

The average vorticity distribution shows a nice bell-shape in the three configurations. In case of the perfect and imperfect configuration, a similar distribution is detected with a maximum at $|\Omega| = 14$. A maximum in the inclined case is significantly higher at $|\Omega| = 22$. In window E a general shift is detected towards $|\Omega| = 10$ in the perfect and imperfect case, where the peak in the inclined case is detected at $|\Omega| = 12$.

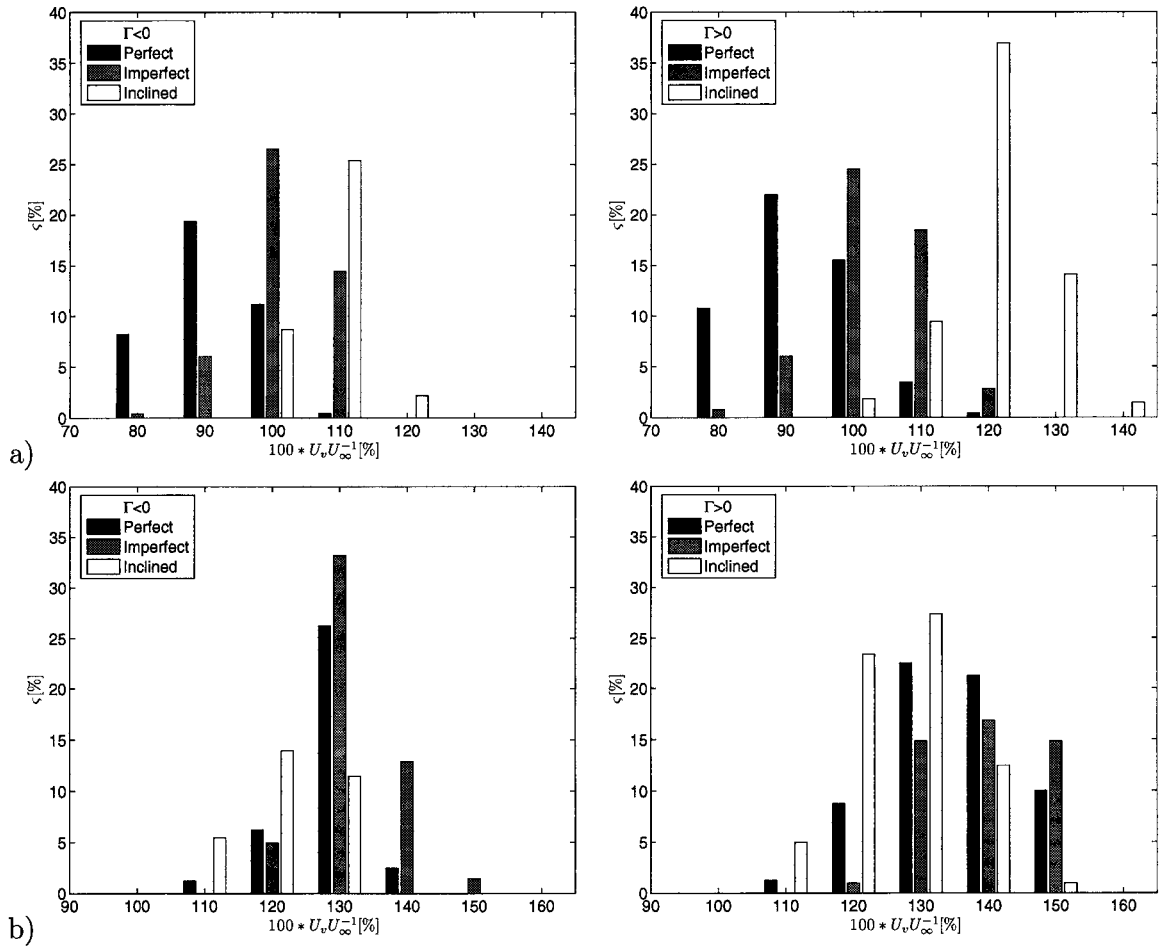


Figure B.1: Advection velocity of vortical structures along the first shear layer. The left column are negative structures and the right column are positive structures detected in control window a) A, b) C.

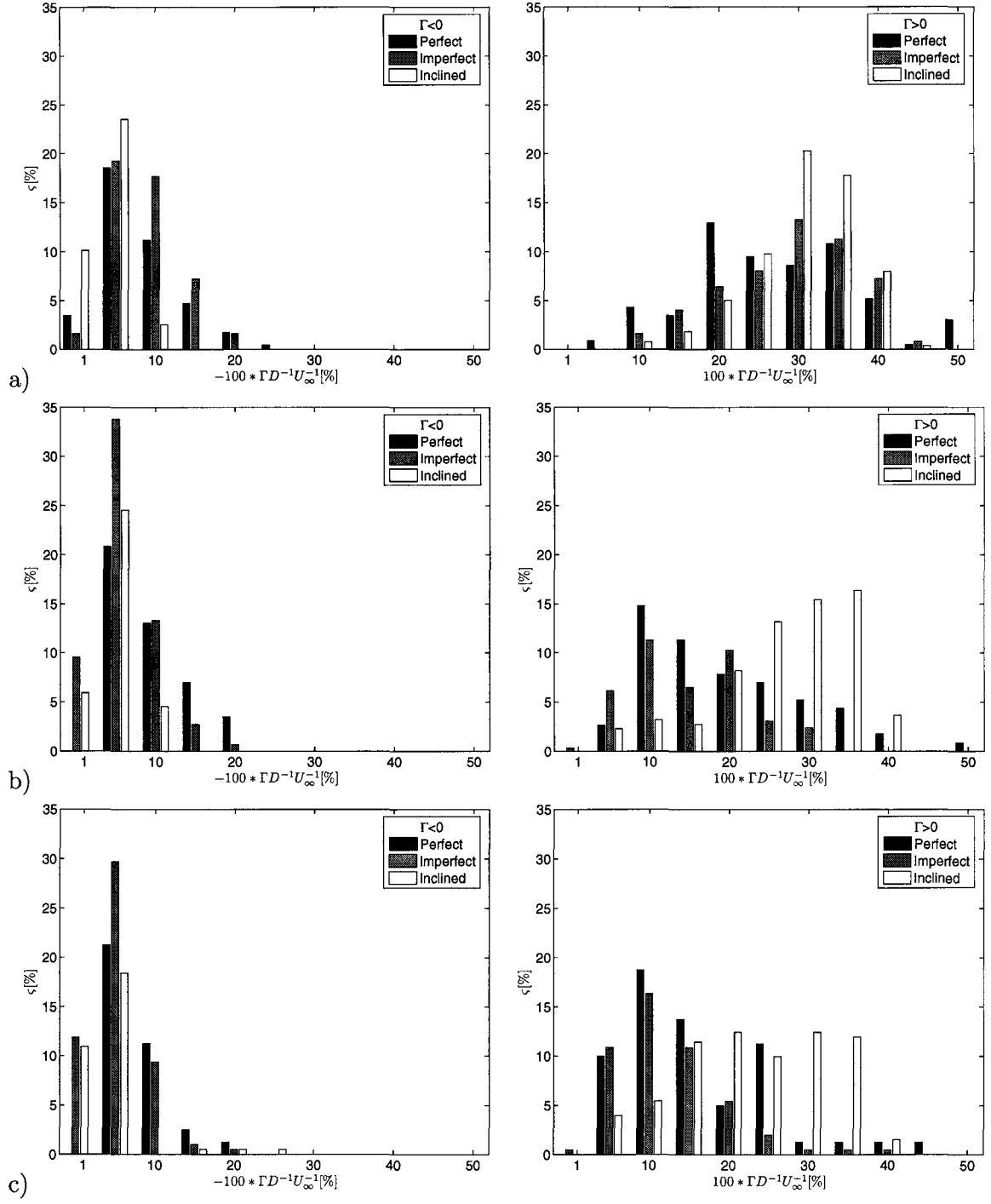


Figure B.2: Circulation of vortical structures along the first shear layer. The left column are negative structures and the right column are positive structures detected in control window a) A, b) C.

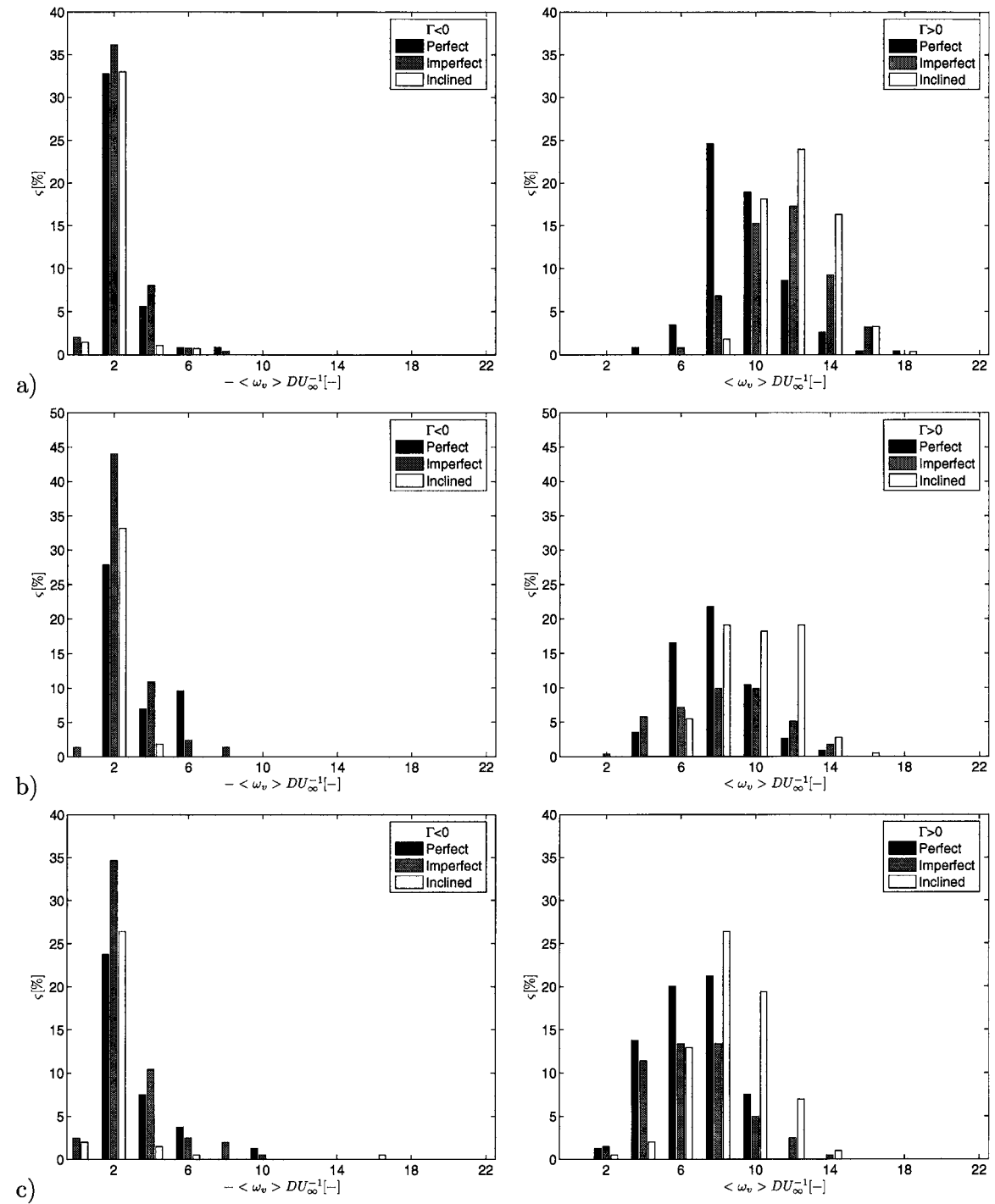


Figure B.3: Average vorticity of vortical structures along the first shear layer. The left column are negative structures and the right column are positive structures detected in control window a) A, b) B and c) C.